Characterization of passive discharge losses in a flywheel energy storage system

by

Miles A. Skinner

A thesis submitted in partial fulfillment of the requirements for the degree of

Master of Science

Department of Mechanical Engineering
University of Alberta

Abstract

Flywheel energy storage systems (FESS) have a wide range of applications in energy grids and transportation such as load balancing, frequency regulation, power quality improvement, and primary or secondary power supplies. Recently, the adoption of high strength composite rotors has allowed FESS to more efficiently achieve these goals making them viable alternatives to electrochemical batteries, or other storage devices. Similar to the effects of high performance composites, other rapidly evolving technologies, including high-efficiency motors and low friction bearings, have rapidly pushed FESS technology into new applications and expanded possibilities within existing sectors. However, this growth is hampered by limited understanding of passive discharge behavior and losses associated with the primary sources of energy dissipation – air friction, bearing friction, and electrical machine electromagnetic forces. This thesis seeks to characterize these losses and create models which could be used to predict losses in future FESS designs. Additionally, unexpected fretting wear at the bearing-hub interface is discussed along with possible mitigation methods. To characterize the passive discharge losses, empirical models are created from experimental data. Then they are used to quantify the expected passive discharge to each source at velocities from zero to 5,000 rpm, and the related times. It was discovered that motor losses were by far the most significant, accounting for approximately 80% of total losses, followed by mechanical bearing friction, accounting for approximately 17%, and finally air friction at 66 Pa, accounting for 3%. Finally, fretting was discovered at the bearing-hub interface, likely caused by the high vibrational loads from the bearings and motor, and was exacerbated by the vacuum environment of the FESS. This was, in part, mitigated by modifying the bearing assembly to better fix the bearing races in place.

Acknowledgments

I would like to thank Drs. Pierre Mertiny and Marc Secanell Gallart for the opportunities and support that were afforded to me throughout the project. Their unique styles of teaching and supervision helped me to develop and grow into the person I am today. On the one hand, one's insistence on independence and individualism forced me to learn to create my own plans, set goals, and be self-motivated. Through this I learned to ask meaningful questions and work through problems. The second supervisor, on the other hand, always strove for perfection while guiding me down a path toward becoming a better researcher. From this I was forced to reevaluate my arguments and gain a deeper understanding of my topic. To the rest of my advisory I would like to thank you as well for your support and guidance.

I would also like to acknowledge the support of the NSERC Energy Storage Technology Network which not only funded the flywheel energy storage system project but also goes through great effort to disseminate the content of this and many other energy storage projects to industries, law makers, and the public. Their efforts are truly invaluable to the development of the energy storage technology in Canada.

Finally, I'd like to thank my colleagues and family who have always supported me. To my family who, despite questioning my sanity after I moved from sunny San Diego to the frozen tundra that is Edmonton, never failed to believe in me. To the innumerable friends and colleagues, I met while here, I could not have completed this degree without you. Honestly, you are all wonderful people and I am better for have known you.

Contents

List of Figures

List of Tables

Nomenclature

A_{con} = Contact region area integral

a = Contact region major axis

B = Magnetic field strength

b = Contact region minor axis

b_m = Motor magnet width

c_{off} = Initial contact offset

c_m = Reduced torque coefficient

D = Total rotor cost

$\overline{D}$ = Normalized rim cost

d = Material cost density

E = Young's Modulus

E_{kin} = Instantaneous kinetic energy of the rotor

F = Force

F_{load} = Applied bearing load

f = Electrical frequency

h = Flywheel rotor height

I_{amp} = Current in motor [A]

I_{cyl} = Moment of inertia, thick walled cylinder

I_{hub} = Moment of inertia from the hub

I_{rim} = Moment of inertia, single rotor rim

I_{total} = Total moment of inertia

K = ones matrix for non-Hertzman analysis

k_c = Classical eddy current coefficient

k_e = Excess eddy current coefficient

k_h = Hysteresis coefficient

M = Air friction moment

M_{total} = Total air friction moment

m = Mass

N_{rim} = Number of rims in the rotor

P = Passive discharge [W]

P_r = Air pressure

p = pressure on bearing element

R = Resistance [Ω]

Re = Reynolds number

r = Radius

T = Torque

T_f = Frictional Torque

T = Motor torque

t = Thickness

t_{tot} = Rotor thickness

u = Displacement

V = Voltage

V_m = Magnet volume

w = elastic deformation matrix

z = initial distance between contact surface

Greek Letters

α = Best fit constant coefficient

β = Best fit exponential coefficient

ε = Strain

η = Fiber wind angle

θ_t = Taper angle

μ = Friction coefficient

v = Poisson's ratio

ρ = Mass density

ρ_{pm} = Resistivity of permanent magnets

σ = Stress

τ = Air friction shear

ω = Angular velocity [rads/sec]

Subscripts and Superscripts

A	=	Axial
air	=	Air friction
b	=	Rotor bottom surface
$core$	=	Motor stator or rotor core
DC	=	Direct current
EMF	=	Electromotive force losses
i	=	Inner
j	=	Rim number, j^{th} rim
max	=	Maximum
mb	=	Mechanical bearing
mot	=	Motor
N	=	Normal
o	=	Outer
pm	=	Permanent magnets
r	=	Radial direction
s	=	Rotor edge/side surface
t	=	Rotor top surface
θ	=	circumferential

1 Introduction

Renewable energy production is rapidly growing in popularity as traditional fossil fuels become scarcer and global climate change becomes more extreme. Canada is uniquely positioned for renewable energy production with readily available hydroelectric, solar, and wind sources in abundance. According to a National Resources Canada study from 2013 just over 60% of Canada's energy comes from renewable sources. They are, in order from largest to smallest, hydro, wind, biomass, and other sources [1]. However, due to the intermittent behavior of many sources, such as wind and solar, significant storage capacity is required to satisfy demand. This inconsistent production presents challenges in load balancing, electric grid reliability, and power quality, all of which can be addressed through energy storage systems. Electrical energy storage systems are anticipated to provide the solution to these issues, but are far underutilized and severely lacking in diversity. In the United States only 2.5% of the delivered electrical energy uses energy storage as a critical component in maintaining a reliable supply of energy, while other leading countries are closer to 10% and 15%, Germany and Japan respectively. Further, the vast majority of storage capacity is in pumped hydroelectric with compressed air and batteries lagging significantly behind [2, 3].

The conventional method of increasing electrical energy storage is using electrochemical batteries. While these batteries are growing in popularity they have some significant disadvantages – such as low cycle life-times, high maintenance, and disposal or recycling issues [3] – making them not ideal for many applications, especially those in the renewable energy sector. Flywheel energy storage systems (FESS) have several main advantages over battery storage making them much more attractive in many fields. They have a high charge and discharge rate, lifetimes ranging from $10^5 – 10^7$ cycles or 10 – 20 years, and high specific energy of approximately 100 $\frac{Wh}{kg}$ [4]. Further, they do not experience depth of discharge effects or cyclic degradation like electrochemical batteries, and have a relatively high cycle efficiency, up to 95% depending on the electrical components [3]. For many applications, FESS can provide the necessary storage and power capacity with longer lifetime and lower environmental impact than electrochemical batteries.

An FESS can roughly be divided into three primary components: the housing, the rotor, and the electrical machine. The housing is of the largest components, and has several main

purposes. First, it protects the rest of the FESS from any environmental effects such as air friction or foreign debris contamination. The rotor provides all the energy storage capacity. Finally, the electrical machine inputs and extracts energy from the system. A cross sectional diagram of the FESS is given below with all primary components labeled

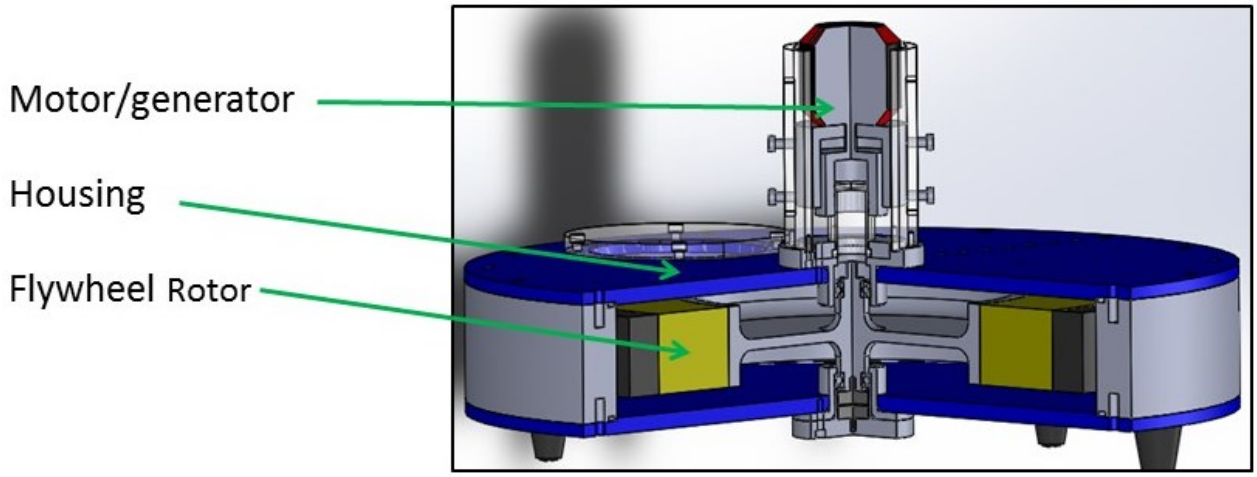

Figure 1: FESS cross section showing the primary components assembled as in the test stand.

One of the largest advantages of FESS over other energy storage devices is its customizability for each specific application. While this concept is little discussed it is passively acknowledged throughout the field. Each component is semi-modular meaning it can be replaced with a similar functioning component to modify the behavior of the system. For example, the rotor can be replaced by a larger or higher strength rotor to increase the energy storage capacity without effecting the power input or output of the system which is controlled by the electrical machine (i.e., motor/generator unit). Similarly, the electrical machine can be replaced by a higher instantaneous or constant power rating without effecting the energy storage capacity or specific energy. Bearings can be replaced with an equivalent component to reduce cost or passive discharge without significantly effecting the electrical machine or rotor performance. This interchangeability of many components is the reason for FESS can be so easily integrated into a wide variety of application and over such a large power and energy range. Further, the range of rotor, bearing, and motor/generator, materials and designs adds additional degrees of freedom [2]-[11]. This is in stark contrast to electrochemical batteries which do not offer this type of customizability, meaning high speed composite FESS, while relatively new, have great potential in many applications.

FESS have been implemented in electric grids to reduce power spikes, frequency regulation, improve power quality, and as backup power supplies for an uninterrupted power supply (UPS) systems. These grid level applications generally range in energy and power capacity between the kWh to MWh range and similar range for energy capacity, kW to MW, depending on the application. For example, Temporal Power, an energy storage company based in Mississauga, Ontario, Canada, has developed a 5 MW all steel flywheel for use in the Toronto grid for regulation. The primary focus for this installation will be to provide frequency response services to the Ontario electric grid [5]. Similar systems have been employed in Canada and the United States by Active Power (Austin, Texas, United States), as a UPS, Beacon Power(Wilmington, Massachusetts, United States), for frequency regulation and power quality [6], and Boeing Phantom Works (The Boeing Company, St. Louis, Missouri, United States), for power quality and power spike reduction [3].

The transportation industry also has large potential for FESS in kinetic energy recovery systems. FESS applications in nearly all sectors of the public transportation industry – e.g., buses [7], cars [8], trolleys [9], and shuttles [10] – have been extensively studied. Porsche (Stuttgart, Germany) implemented an FESS system in their 911 GT3R Hybrid race car which utilizes breaking energy to accelerate a flywheel that, in turn, is used to accelerate the car after breaking. This system can significantly reduce fuel consumption during operation, up to 25% based on Porsche's studies [8]. Additionally, public transit systems, such as City of Edmonton Transit System's Light Rail Transit (LRT), can utilize a similar system to reduce energy consumption and grid dependency. Currently, the LRT uses electric motors to slow the trains, and passes the generated electricity through a bank of resistors to dissipate it as heat. Replacing the resistor banks with FESS could provide significant energy savings to the grid [11]. For example, the FESS used in this study was originally designed for use on the LRT. At the design speed of 30,000 RPM the FESS can store 0.234 kWh of energy, or approximately a quarter of the average total energy needed for the train entering and leaving a station. Therefore, this system would employ three flywheels per car for optimum performance [11]. The breaking energy recovered from braking while entering the station is stored in the flywheel, then fed back into the trains electrical system. To reduce gyroscopic effects flywheels can be placed in pairs rotating in opposite directions.

Even though FESS have a wide variety of application across many industries, but the technology is still developing. The majority of current studies into the construction of FESS systems have focused on maximizing energy density and storage time using ultra-high vacuum levels, low and high temperature superconducting magnetic bearing [12], and high speed composite rotors. While the vacuum level and bearings are correctly judged to maximize the rotor energy density and storage duration it is not an economically feasible approach to widening the adaptation of FESS in residential and commercial energy storage applications given the additional cost of operating active, or superconducting, magnetic bearings and vacuum pumps capable of maintaining ultra-high vacuums. The studies that do exist concerning low cost FESS are limited to very specific application, such as their use in photovoltaic microgrids [13], rather than a more generalized analysis which can be applied to a wide variety of applications. This is likely due to the difficulty in analyzing the FRP used in the rotor. It is only within the last two decades, through the works of Gabrys et al. [14] and Ha et al. [15], that the stress distribution within filament wound composite rotors could be easily determined. Further, the application of these models in cost minimization strategies is even more recent [16]. Therefore, it is only very recently that such studies have been conducted.

Low cost, small-scale FESS, such as those suitable for residential and transportation applications respectively, present several unique challenges which do not appear in grid energy scale systems. Mechanical bearings are the only practicable choice for low cost FESS as magnetic bearings, especially active or superconducting magnetic bearings, are prohibitively expensive. This, however, may significantly increases the wear due to vibrational and cyclic loading on FESS components promoting e.g. fretting at the bearing-hub interfaces. Larger systems can, in terms of size, afford the equipment necessary to cool superconducting bearings or power active magnetic bearings; while more expensive systems are less sensitive to the cost of any magnetic bearing system. The high efficiency FESS developed by Shultz et al. [17] operates at 0.01 Pa with active magnetic bearings at 2,800 rpm measured 1.7% per hour passive discharge. Low cost, small scale systems, such as those employed in residential and transportation sector, are likely to operate at lower vacuum levels and use inexpensive bearings as trade-offs are made between performance and cost. Studies into these systems are significantly lacking in detailed analysis of each source of energy loss and their method for characterizing those losses. For example, Sato et al. [18] quantified passive discharge to magnetic seal,

windage, bearings, and a range of no-load losses in the electrical machine. However, they only briefly describe how electrical and mechanical losses were characterized in general before claiming the bearing and electrical losses accounted for nearly 50% and 40% respectively. While this study does highlight some design decisions and general concepts in FESS losses it lacks the analysis of each passive discharge source needed to validate the claims. The study by Filatov et al. [19] attempts a similar analysis of losses while attempting to characterize the magnetic bearing in the study. However, Filatov et al. is not rigorous in the analysis of their system in general, so the results cannot be verified. The passive discharge results of these are limited not because they are poorly done or inaccurate, but rather because their primary goal was to describe a high efficiency FESS in the first and a novel magnetic bearing system respectively. Therefore, while it is important to recognize the contributions of the above studies, [12]- [19]; studies focusing on the analysis of FESS passive discharge losses are relatively rare. The present study characterizes these losses by first gaining a better understanding of each primary passive discharge source and then experimentally isolating each source and quantifying those losses.

The mechanical design of an FESS poses unique challenges which do not exist in other high speed rotating machines because the system must operate under vacuum. Wear and corrosion in high speed rotating components due to cyclic loading and vibration are serious concerns for any machine. Fretting is one of the most common forms of wear and corrosion in bearing shaft systems primarily due to vibrations, often more generally referred to as oscillatory forces [20, 21]. Fretting is a combined mechanical wear and corrosion process where material is removed from contacting surfaces due to small scale sliding at the interface. This is a serious issue for any FESS with mechanical bearings which have very high vibrational response, even at the low speeds, i.e. 5,000 rpm. Fretting is characterized by the detachment of particles from contacting surfaces due small scale relative motion at the interface. Under atmospheric conditions metallic surfaces and particles, such as the aluminum rotor hub, readily oxidize acting as an abrasive and increasing the wear rate. However, under vacuum the surface does not oxidize as material is removed causing even faster growth than is typical under normal conditions. Fretting removes aluminum oxide particles from the hub surface at the bearing-hub interface exposing the pure aluminum below the oxide. This is unique to rotating machines operating under vacuum. The effects of wear on the rotating components is also investigated in the present study to gain a better understanding of FESS machine design, particularly at low speeds and with

mechanical bearings. Note these problems apply to all FESS because magnetic bearings in FESS require a minimum angular velocity to function properly, and hence, so they utilize a hybrid bearing assembly with mechanical bearings at low velocity and magnetic bearings otherwise.

2 Previous Research

2.1 FESS Development

2.1.1 Rotor Design

FESS are highly customizable energy storage devices where each of the primary components can be replaced by an equivalent part to tailor it to the specific application. While this is advantageous in nearly every circumstance it makes designing FESS rather difficult as a thorough understanding of each component, and its interactions with other parts of the FESS, is necessary to optimize a FESS design.

Much of the development in this field is due to rapidly evolving technologies introducing design options FESS were lacking in the past. Initially, new materials, such as high strength fiber-polymer composites and low friction ceramic bearings, presented new opportunities for rotor and mechanical bearing design. Strong rare earth magnets and super conducting materials were developed into more efficient electrical machines and magnetic bearings. Each new technology was an opportunity to improve FESS, however, they also represented added cost and unique challenges in terms of understanding an increasingly complex design space. As will be shown, researchers have focused heavily on understanding composite material application in FESS rotors to improve such characteristics as specific energy, total energy, and cost. Additionally, the adoption of various types of magnetic bearings has significantly affected the expected behavior of and possible applications of FESS.

Flywheel energy storage systems are a relatively old technology. In its simplest form a flywheel is merely a large rotating disk connected to input/output systems. They were vital to the operation of many types of engines and machines during industrialization in the 19th century, and are still employed very widely in cars and other machines. However, it is only in the1970s and 1980s when FESS were seriously studied as energy and power storage devices.

Prior to the 1970s, nearly all flywheels in use were constructed from (isotropic) materials such as stone or steel which limited their energy density and efficiency. Steel flywheels are still in use, for example the system developed by Amber Kinetics (Amber Kinetics Inc, Tulsa, Oklahoma, USA). The advantages of steel flywheels are that materials are very well understood, readily available, and comparatively inexpensive. Steel rotors rely on their large mass with relatively low angular velocity as opposed to a high specific strength for high rotational speeds

(as for composite rotors) to achieve the desired energy storage capacity. Current models from Amber Kinetics can store 32 kWh with plans to increase the capacity to 160 kWh. The large mass of isotropic rotors is also their main disadvantage as this may increase manufacturing cost with regard to material volume, and supporting systems, such as radial and axial bearings. Further, the large mass increases transportation and installation costs. With the advent of high strength ceramic-plastics, or fiber reinforced polymer (FRP), composite systems were started to be developed in the 1980s allowing FESS to expand into applications it could not feasibly fulfill with conventional materials. Early research into FESS materials, 1970s and 1980s, conducted by Sandia National Laboratories [22] and by the US Department of Energy [23] indicated that isotropic flywheels were a mature technology with little room for improvement, and were incapable of achieving the high strength, fatigue limit, low density, and other material properties necessary to construct a cost effective and efficient FESS. FRP rotors, on the other hand, showed a large potential for FESS advancement because composite materials have these properties in abundance and the ability to tailor those properties to the specific application. As opposed to isotropic rotors, FRP rotors can achieve much higher energy densities and specific energy which could increase the efficiency of the system. The contemporary review paper by Long and Zhiping [24] directly compares the density, strength, specific energy, and cost per unit weight for a variety of isotropic and FRP rotors. Their results show FRP rotors provide significantly higher strength and specific energy than isotropic materials, but at the expense of cost per unit weight. Other early studies with focus on FRP materials, beginning in 1975, were conducted at Lawrence Livermore National Laboratory, in the United States, by Chao et al. [25] seeking to develop a material property database for composites suitable for application in flywheel rotors and disseminate that information to industries. Comparing two types each of glass fiber – S-2 and E-glass – and aramid fiber – Kevlar 49 and 29, and a variety of matrix materials to determine the mechanical properties, creep behavior, toxicity, and cost of the resulting composites. They developed tables of these properties to assist researchers and industries select the appropriate material for a specific application

Analysis of the performance, based on energy stored per unit volume, unit weight, and unit cost, of filament wound FRP rotors was conducted by Foral and Newhouse [26], and Johnson and Gorman [27]. Johnson and Gorman sought to define the maximum possible energy density of a multi-rim rotor using a common, at the time, intuitive approach to understanding

rotor limits. Multi-rim, or hybrid, rotors use multiple concentric FRP rims press fitted together to offer greater control over the rotor design. Their methodology derives from the Virial theorem, but can be simplified to a rule of mixture calculation for hybrid rotors, i.e. a rotors energy density is the weighted sum of each material's energy density. Johnson and Gorman formalized this approach to rotor design, however, it only predicts the theoretical maximum energy density. This method assumes perfect mixing of materials and is not an accurate representation of testable rotors.

Foral and Newhouse also studied multi-rim rotors, however with a variety of materials and a finite number of rims. Their study compared glass fiber, aramid fiber, and carbon fiber single rim and multi rim hybrid rotors to define performance dependence on variations in rotor properties. Most significantly, this study identified a strong relationship between rotor temperature and performance, and the potential advantages of hybridized rotor construction. Foral and Newhouse concluded that a properly constructed hybrid rotor will foster a positive interaction between the discrete rim materials allowing the rotor to achieve greater total energy storage than either material independently. This is a key concept employed by many later researchers to significantly increase FESS capacity without drastically increasing system cost. Material cost is one of the largest barriers to implementation of FESS systems, so minimizing these costs are of primary concern to any low-cost system. The work of Foral and Newhouse, and similar works, on high strength filament wound carbon fiber and hybrid rotor construction marks a corner stone in nearly all modern FESS development.

While Foral and Newhouse worked to better understand composite material's impact on the field, they also helped develop a method to analyze induced stresses during FRP rotor operation, to ensure safe designs. They helped Foral and Newhouse also develop one of the most widely used analytical methods for this technology in the early 1970s and 1980s as a modification of the Classical laminar plate theory (CLPT) of composites to account for the cylindrical shape and wall thickness walls. Foral and Newhouse proposed this method to compare FRP rotor performance and optimize their design for a number of metrics. First, CLPT. This method treats each rim as a laminate with a finite width, so the entire rotor is constructed from N rims, and assumes thin laminations with perfect bonding between layers. This method is based on a plane stress assumption, so the induced stress and strain at an arbitrary axial height is

constant throughout the rotor. Then, the radial stress and strain can be calculated for all points in the rotor.

This concept was later expanded by Haridy et al. [28], Ha et al. [29], and Krack et al. [16] by considering multi-rim rotors constructed from a series of concentric rims pressed fitted together. Each rim is constructed from a unique material providing even more customization of the rotor. Considering the stress equations from Ha et al. [15] they showed the stress increases with radius, so the outer most rim must support the greatest load while the inner most rim will support comparatively little load. Therefore, low strength and low stiffness materials should be used for the inner rims while high strength and high stiffness materials are more appropriate for the outer rims. Further, at high speeds the rotor will tend to deform outward due to radial forces, so the high stiffness outer rim will support the low stiffness inner rim. In this manner, stresses in the radial direction, i.e. the direction transverse to the fibers in which fiber-polymer composites exhibit lowest strength, can be reduced, allowing a rotor to reach higher speeds than it could otherwise. Finally, low strength and stiffness materials tend to be less expensive which can significantly reduce the overall cost of the rotor.

While increasing the number of rims can improve the performance of the rotor, the effect does not increase linearly. As shown by Ha et al. [29] and Haridy [28] the performance increases asymptotically. For carbon and glass FRP rims Haridy showed energy density increased by 80% from one to two rims but only by 30% for one additional rim. Ha demonstrated similar results with energy density tripling from one to two rims then increasing by only 67% for the third.

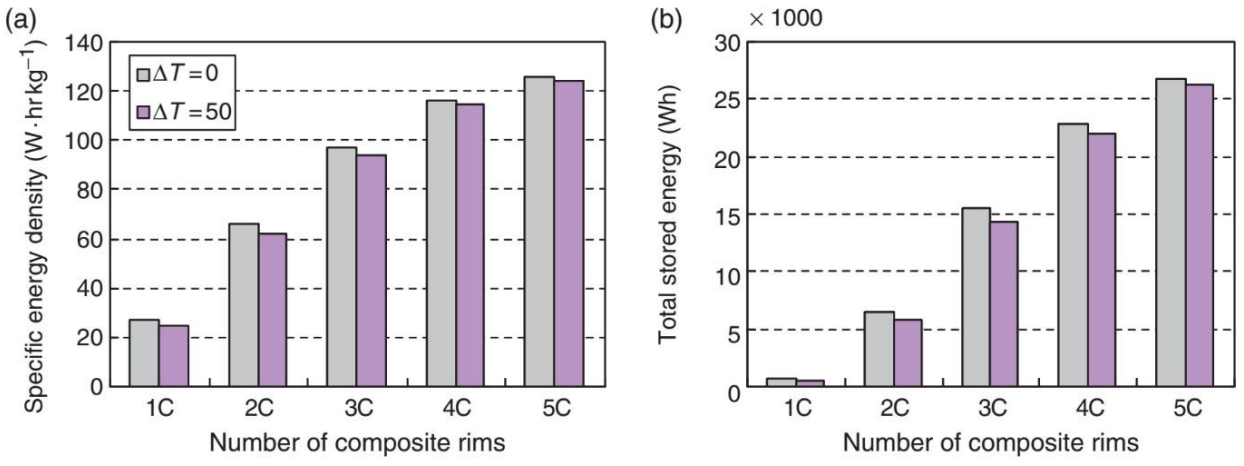

Figure 2: a) Specific energy density of the rotor by rim number b) Total energy storage by rim number. [29]

An optimization strategy was developed by Krack et al. [16] around the aforementioned analytical method to maximize energy storage capacity while minimizing rotor cost. This is one of the proposals Foral and Newhouse made when they introduced their work in the late 1990s [26]. Ultimately, Krack et al. developed an algorithm which takes material properties, cost, number of rims, and geometry as inputs and produces an optimal size for each rim. Through this work, Krack et al. concluded that two or three rims are ideal for low cost rotors as it balances performance improvements with additional manufacturing costs. This is a similar conclusion Ha et al. reached in [29, 30] where, except as proof of diminishing returns, their studies have not exceeded three rims.

The studies discussed above are largely theoretical with limited validation. In order to validate the optimization results a research program is established that includes fabrication and testing. To this end a FESS testing systems is developed to study multi-rim rotors.

2.1.2 Bearing Systems

A cost-based optimization approach is relatively unique in this field as much of the focus has been on understanding the possible breath of FESS applications and limits through the application of new technologies. As mentioned earlier, high strength composites have significantly increased the performance of FESS rotors, nevertheless, the bearing and electrical systems are equally impactful.

Bearings are divided into two main categories, mechanical and magnetic. Magnetic bearings can be further differentiated into passive (PMB), active (AMB), and superconducting magnetic (SMB) magnetic bearings. Radial and axial bearings of each type exist. Note the FESS in this study use radial mechanical bearings and two opposing rare earth magnets to support the weight of the rotor. The opposing magnets simply use the strength of the magnetics to support the rotor. These magnets behave like other axial magnetic bearing in that they support the rotor, however they are not self-centering. Therefore, they are unstable, pushing the rotor away from the axis of rotation, which increases radial loading on the mechanical bearings. This is unusual in FESS because conventional magnetic thrust bearings are equally advantageous, but are in stable equilibrium, pushing the rotor toward the axis of rotation, to not unnecessarily increase the radial bearing load. In this section, conventional axial magnetic bearings will be discussed as these are nearly exclusively employed in FESS.

All magnetic bearings are highly effective at reducing friction and isolating the rotating components from the outside perturbances, but require a minimum operating velocity to stabilize the rotor through the induction of eddy currents, an effect that is dependent on velocity. Therefore, all systems require mechanical bearings, at least, during low speed operation. Conceptually, the simplest to understand are passive magnetic bearings, such as those discussed by Lembke [31] and Filatov et al. [19]. All magnetic bearings function similarly, so the PMB will be discussed for clarity. Then the differences between the different types will be introduced. The PMB examples cited here are two configurations of the same bearing type and are taken to be representative, yet, it is recognized that other configurations exist which function identically to the examples.

Magnetic bearings utilize a conductive material, generally copper, which rotates at very high velocity within an asymmetric magnetic field created by an array of permanent magnets. The flux through the conductor is dependent on the magnetic field strength and the rotational velocity with larger fluxes generating stronger eddy currents. These eddy currents are composed of moving electrical charges which generate an opposing magnetic field. The opposing magnetic fields, from the permanent magnets and the induced eddy currents, resist each other equally on all sides of the bearing creating a negative feedback cycle stabilizing the system. Any force acting on the rotor to push it off center exposes one side of the conductor to a greater flux, and speeds, which then creates stronger eddy currents, therefore stronger opposing magnetic fields, which push the rotor back to center. The two key parameters for magnetic bearings are the same as for springs, that is, stiffness, measured in $\frac{N}{mm}$, and damping, measured in $\frac{Ns}{m}$.

Lambke [31] focused on radial support bearings which could be employed in place of mechanical ball bearings. He measured the PMB stiffness as a function of velocity and found the stiffness plateaued between 50,000 and 100,000 rpm with a stiffness of 20 – 60 $\frac{N}{mm}$ depending on the specific configuration of the conductor and magnets in the PMB. The damping coefficients for these bearings peaked in the same velocity range. The damping coefficients ranged from 4 – 9 $\frac{Ns}{m}$. What is most notable about the studied radial PMB is the very high velocity required for the bearings to function properly, so some alternative bearing assembly is required below this speed.

Filatov et al. [19] focused on axial support bearings which could be used in place of tapered roller bearings or thrust bearings. They attempted to reduce operating cost of PMB by

making some minor changes to the design. Copper windings were used for the conducting component to reduce energy loss, introduced a simple electric circuit to the stator to improve the damping coefficient, and using ceramic magnets to create the asymmetric magnetic field. Their design was able to stabilize a 3.2 kg rotor at just over 1,080 rpm, the minimum functional speed, and had a measured stiffness of $2\,\frac{N}{mm}$. They noted that this design could be improved by substituting the ceramic magnets with more powerful rare earth magnets, and theorized a stiffness of $40\,\frac{N}{mm}$ at 6,000 rpm. Interestingly, Filatov et al. attempted to quantify the passive discharge associated with this bearing system, but had difficulty isolating it from other sources. This forced them to make several iterative changes to the system. First, they began operating the FESS in high vacuum. Then, they added a number of steel rings, to attempt to create a more uniform magnetic field, which doubled the minimum operating speed and limited the maximum to 2880 rpm. They eventually estimated the losses associated with this set up to range from 2.4 W to 1.2 W at the maximum and minimum velocities respectively.

Active magnetic bearings operate under the same principle as PMB in that they use electric currents to generate magnetic fields which constrain shaft lateral movement. This type of bearing is discussed extensive in [32, 33]. AMB employ a control circuit with sensors, conductive coils, and a controller. The controller measures the position of the shaft using the sensors, then modulates the current running through the coils to produce a magnetic field. From this point, they function identically to PMB. AMB require an energy input to power the circuit and experience resistive losses in the windings [34], so, AMB are not ideal for a long-term energy storage system, such as for energy grid applications. Additionally, AMB are naturally unstable requiring the controller to function as opposed to PMB which are intrinsically stable. These bearings are attractive for short term storage than mechanical bearings, such as regenerative breaking for transit systems, where the active components do not need to be operating at all times or the energy storage duration is short minimizing additional losses. Further, transportation systems with short storage times, and regular maintenance serves to minimize the chance of failure in the more complicated bearing system.

Superconducting magnetic bearings seek to further reduce passive discharge losses from the bearings by removing the resistive losses in the conductor. Magnetic bearings eliminate the physical contact associated with mechanical bearings, so the only source of loss is the conductor resistance. By replacing the metallic conductors with superconducting materials these losses can

be minimized or nearly eliminated. SMB can be either active or passive as shown by Coombs et al. [35] and Xia et al. [36], respectively. Further, some FESS bearing assemblies use both passive and active elements to fully constrain the rotor, such as in [37]. While SMB have the lowest passive discharge losses they also possess a number of serious drawbacks. First, they typically have low stiffness and are very vulnerable to perturbations [38], meaning they are not well suited to transportation applications as the effects of uneven road or rail conditions could easily damage the system. Further, and more significantly, all superconductors require some level of cooling to function properly. The discovery of high temperature superconductors (HTS), the most popular of which is yttrium barium copper oxide (YBCO), made construction of superconducting bearing possible. This material is has been used in small and large scale FESS ranging from 1 – 100 kWh [35] - [39]. YBCO is described as a HTS, however its ideal operating range is below 90 K, so all systems implementing HTS magnetic bearings have extensive cooling systems to maintain this condition. It is common to cycle liquid nitrogen around the bearing, as discussed by Coombs et al. and Xia et al., but other cooling systems have been proposed, such as the two-stage thermosiphon described by Jung et al. [39], to eliminate the consumption of N_2 which must otherwise be continually replaced. Regardless, this requirement significantly increases the operating and maintenance cost of the FESS making SMB most suited to the largest grid scale energy storage projects.

The decrease, or lack, of performance of magnetic bearings at low velocities has led to a hybridization of bearing assemblies in many FESS. That is, the FESS bearing assembly has mechanical bearings used at low velocities and magnetic bearings for high velocities. When using a two-stage bearing assembly, the mechanical bearings are decoupled when not in use. Filatov et al. [19] determined the minimum operating speed of their PMB design when the rotor was supported by the mechanical ball bearings rather than the PMB. This hybridization is also discussed in [34] where mechanical ball bearings are described as emergency backup systems for magnetic bearings in case of power or control failure. This is not to say mechanical bearings are not used at all, as they are much less expensive than magnetic bearings which can significantly reduce the overall system and operation cost. Sato et al. [18] was focused on reducing the system cost for long lifetime UPS with FESS, and showed using mechanical bearings resulted in significant cost reduction. This would also be a driving factor in industry where minimizing cost is of primary importance. However, it is becoming much more common to have a hybridized

bearing system as in [40, 41] given that mechanical bearings are necessary to stabilize the system at low speeds. But, mechanical bearings create significant frictional loading especially at speeds greater than 20,000 rpm which many FESS operate at. Bearing wear against the shaft is only significant with mechanical bearings because magnetic bearings do not have a physical connection between the inner and outer bearing races so vibrational forces from the housing, electrical machine, or other sources are not transferred throughout the system. Mechanical bearing's limited use during operation in FESS with a hybridized bearing system has led to little analysis and effort toward understand how mechanical bearings operate in FESS at the relatively low velocities in which they are required, below 5,000 rpm, as they are not seen to significantly impact the system. This a shortcoming as friction and vibration in mechanical bearings can be significant at these velocities causing a decrease in lifetime of system components. Further, the vacuum under which most FESS operate can complicate the wear behavior of system components. Gaining a better understanding of how the system behaves at low velocities is important as a significant portion of the expected component wear will exist in this range. This is also true for hybridized bearing systems even though they experience little to no wear while operating with magnetic bearing support.

2.1.3 FESS Application and Design

The use of FRPs for the construction of flywheel rotors allowed FESS to expand into higher capacity and faster charge discharge rates, power output, making the use of FESS for public and other mass transportation and long term storage applications much more viable. Some of the earliest successful FESS systems in for transportation applications were conducted out of Switzerland in the 1950s. However these projects were relatively short lived, costly experiments. It was not until much later when the U.S. Department of Energy funded a series of studies in the public and private sectors through the 1980s and 1990s that long term urban mass transport systems were given serious attention. These studies employed a variety of steel and composite rotors. The goal of many of these studies were similar, consider [42] to be representative, to develop a trolley system powered entirely by 15 kWh FESS with a lifetime of 23 years. The 1.067 m diameter, 0.59 m tall rotor was designed to rotate at 12,500 rpm under 1.3×10^{-3} Pa. The vacuum level was achieved using two cylindrical molecular pumps in the housing. The driving cycle for this FESS was 12 minutes starting at a maximum 12,500 rpm and decreasing to 6,250 rpm. The system was tested for 1,000 cycles.

While it has been shown that FESS powered vehicles are feasible they are not efficient due to the large energy capacity requirements. The energy density of the rotor was established at 37 $\frac{Wh}{kg}$ in [42] using an FRP rotor. While modern multi-rim flywheels are much higher, 120-150 $\frac{Wh}{kg}$ [29], FESS capacity is still lower than lithium-ion batteries with 150-250 $\frac{Wh}{kg}$, and several orders of magnitude lower than gasoline, 12,200 $\frac{Wh}{kg}$. Therefore, it is not efficient to power a vehicle entirely using a FESS, but rather to supplement existing power systems to capture energy that would otherwise be lost, to breaking for example. Regenerative energy systems can significantly reduce energy consumption in many transportation systems such as transit buses and trains. Power systems with high energy densities can power a vehicle for long periods of time allowing it to travel a great distance before stopping to refuel. Such systems typically struggle with sudden spikes in demand, or become less efficient, such as when accelerating from a stop. FESS excel at high power output, but struggle with long term storage and energy supply. A hybridized bus utilizing a hydrogen fuel cell and an FESS regenerative system, proposed by Heam et al. [43], would be able to significantly improve performance over a traditional diesel bus. During a typical day, completing 371.7 km, the hybrid bus would reduce energy consumption from 2,957 kWh of diesel to 2,199 kWh of hydrogen with an average efficiency increase from 39.1% to 47.4% and improved acceleration from 0 – 65 kph from 30.3 s to 18.8 s. However, as noted by the researchers, the FESS used in this system was not commercially viable due to the economic cost and physical size of the system.

It is currently common FESS that the potential benefits, while significant, are out weighted by the cost of operating the system, so emphasis has been placed on developing low cost systems to address this issue. The FESS used in the present study, designed and fabricated by Ertz, was investigated by Rupp et al. [44] for application in light rail transit (LRT) systems to minimize energy consumption, and in turn reduce operating costs during normal operation. The rotor design and construction to minimize cost are discussed in later sections of this thesis while the potential benefits to the LRT system are discussed here. As a storage device, FESS has a much higher power input and output ratings than electrochemical batteries, and larger capacities than super capacitors [3]. Therefore, FESS have very high potential for short term storage of breaking energy in electrically powered LRT systems. That is, a train must break as it enters a station and accelerate as it leaves the station in the order of a fraction of a minute to a few

minutes later, so the breaking energy can be captured and stored in an FESS then used to accelerate the train as it leaves the station.

FESS have great potential in this operating environment because of the short cycle times and high power requirements. Further, the energy conservation could significantly reduce LRT operating costs. Rupp et al. [44] studied the possible energy and cost saving of introducing a FESS to the City of Edmonton LRT over a five-year period. For one train with three cars and one 1.45 kWh flywheel per car they predicted cost reductions up to 26.7%. Cost reduction could further be improved by increasing the storage capacity of the FESS [44]. The rotor is estimated to cost 525 CAN$/kWh, the motor is 17 CAN$/kW, so the final estimated cost of the 1.45 kWh FESS is $8,940 providing a rated power output of 481 kW. The operating cost reduction of this system is expected to recover the initial investment of the flywheels after three years giving a net benefit to the transit system for the remaining five years the study focused on.

Economic flywheel design, proposed by Krack et al. [16], seeks to determine a minimum cost rotor for a given energy capacity. That is, the optimum rotor design will maximize the stored energy per unit cost of the rotor. The cost for the rotor, D, is the summation of the cost of the rims and hub, d_j, i.e.

$$D = \sum d_j m_j \left[\left(r_2^{(j)} \right)^2 - \left(r_1^{(j)} \right)^2 \right]. \tag{1}$$

where m_j, r_o and r_i are the rotor rim mass, outer and inner radii, respectively. The rotor cost in equation (1) is simply a weighted summation, however, only the cost ratio between rims is necessary for the optimization so the cost for the first rim is normalized to

$$\overline{D} = \frac{D}{\overline{d_1}}. \tag{2}$$

The normalization cost factors are $\overline{d_1} = 1$, $\overline{d_2} = \frac{d_2}{d_1}$, and so on.

The kinetic energy of the rotor, cost, and stress distribution can all be calculated as described so it is possible to define an optimization problem as

$$\text{Maximize: } f(x) = \frac{E_{\text{kin}}(x)}{\overline{D(x)}} \qquad \text{w.r.t. : } x = \left[\omega \;\; \frac{t_1}{t_{\text{tot}}} \ldots \frac{t_{N_{\text{rim}}-1}}{t_{\text{tot}}} \;\; \eta_1 \ldots \eta_{N_{\text{rim}}} \right]^T \tag{3}$$

$$\text{Subject to: } g(x) = \begin{bmatrix} R(x) - 1 \\ \left(\sum_{j=1}^{N_{\text{rim}}-1} \frac{t_j}{t_{\text{tot}}}\right) - 1 \end{bmatrix} \leq 0 \qquad \begin{matrix} 0 \leq \omega \leq \omega_{max} \\ 0 \leq \frac{t_j}{t_{\text{tot}}} \leq 1 \text{ for } j = 1(1)N_{\text{rim}} - 1 \\ 0 \leq \eta_j \leq 90^{\text{o}} \quad \text{for } j = 1(1)N_{\text{rim}} \end{matrix}$$

where R is the assembled rotor strength ratio vector. The angular velocity, n, is bound between 0 and ω_{max} $\frac{\text{rad}}{\text{sec}}$, and the winding angle, φ, is bound between 0 and 90° but is usually defined as exactly 90° to yield the best possible material properties. The rim thicknesses, t_j, are similarly bounded where the sum of the first $N_{\text{rim}} - 1$ rims is less than or equal to the total rotor thickness, t_{tot}.

An optimization algorithm was created to solve this problem for various rotor sizes and velocities. This program outputs the optimum thicknesses for each rim, the induced radial and circumferential stress at rest and maximum rotor velocity, and displacement also at rest and maximum velocity. This program was used extensively for designing the flywheel used in the present study.

An optimized rotor was found using the algorithm proposed by Krack et al. in [16], however, an attempt should be made to optimize also the cost and performance of the other FESS components in order to be most economically viable. The remaining major components – housing, electrical machine, and bearings – which Ertz addressed individually are discussed in detail in Chapter 3.

The optimized design problem solved by Krack et al. does not account for self discharge losses, type of bearings, or vacuum level, all of which could substantially change the optimum design. In this thesis therefore work is undertaken in order to develop models that could be interpreted in the design problem to account for these losses.

2.2 Contributions

In the previous section, it was shown that although FESS have been studies over several decades there are still significant gaps in the literature related to the impact of mechanical bearings on self discharge, the introduction of bearings and vacuum systems in the optimized design problem of flywheels and on the validation of stress field development in multi-rim FRP rotors. In this study a method to characterize passive discharge losses in a small scale FESS is created. Then, it is employed to develop models of each source of losses, and those models are validated against experimental data. Finally, methods to mitigate a significant source of wear and

fatigue in the FESS bearing shaft assembly are discussed, and recommendations to improve FESS lifetime are made.

2.3 Structure of the Thesis

In subsequent chapters of this thesis a description of the research project is presented. Chapter 3 contains a description of the current FESS experimental test setup and the equipment used to collect data. Chapter 4 describes and discusses the appropriate models for each primary source of FESS energy losses. Chapter 5 contains the experimental procedures, how data was processed, and the energy loss results. Chapter 6 provides a discussion on the observed FESS damage and failure events, their potential causes and effects, and the solutions employed in this study. Finally, Chapter 7 concludes the thesis with closing remarks and potential future work.

3 FESS Experimental Platform

The FESS used in this thesis and depicted in Figure 2, was constructed by Ertz [11]. In the following the main components are detailed with special attention to the modifications in this work.

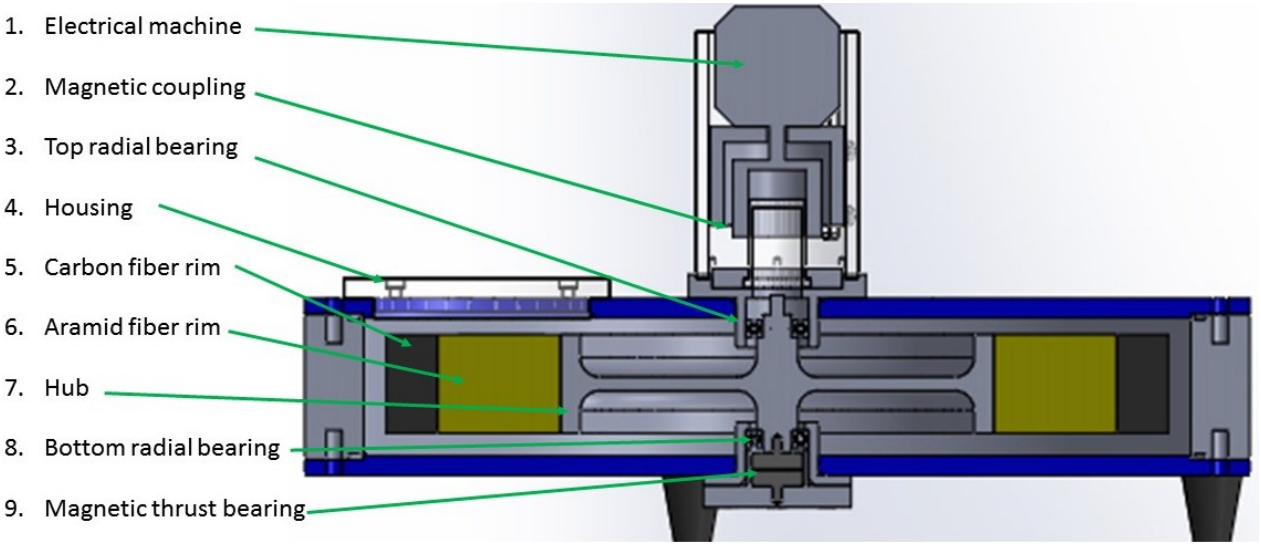

Figure 3: Labeled cross section of the current FESS experimental test stand.

3.1 Housing

The housing has three main purposes. First, it provides mounting surfaces for the motor, bearing-rotor assembly, instruments, and any other necessary components. Second, it maintains a vacuum around the rotor and other rotating components. Finally, it is a crucial safety feature in the event of a catastrophic failure of the rotor or bearings.

The housing, shown in Figure 3, is constructed from a top and bottom plate made of 10 mm 6061 aluminum providing all the mounting surfaces, and a thick cylindrical burst ring, for safety. The bottom plate has a two-part bearing fixture, seen as the two connected parts surrounding the bottom bearing assembly consisting of a radial bearing and a magnetic thrust bearing. The top plate holds a single piece fixture with the upper radial bearing. The bearings are discussed in greater detail below. Directly above the upper bearing fixture an acrylic tube is mounted that which allows the inner part of a magnetic coupling to connect the rotor shaft to connect to the electrical machine, which is located outside the housing. Six threaded holes are placed linearly into the top plate to act as input/output ports for sensors as discussed later.

Additionally, a large round window was added to provide a view of the flywheel during operation and a fixture for the optical speed sensor. A vacuum is maintained inside the housing by vacuum grease coated rubber O-rings at the interfaces between the burst and ring and the top and bottom plates.

The burst ring is designed to withstand the energy of the rotor should a catastrophic failure occur. Unlike the other components of the housing, the burst ring is constructed from 30 mm steel with no holes or slots cut into the sides. The top and bottom faces have an O-ring grove and bolt pattern to attach the plates. The housing will be held under vacuum for long periods of time, so a finite element analysis (FEA) was performed to ensure the deflection of the plates will not negatively affect the system. The maximum deflection of the housing was found to be low with less than 0.06 mm in the center of the bottom plate. The FEA results were validated during this study and the top plate deflection vs. pressure results are shown in Figure 4b. In this figure the pressure along the x-axis is given in Torr, where 1 Torr is equivalent to 1 mmHg or 133 Pa. The top plate deflection along the y-axis is in mm. The deflection is linear with pressure as expected. Further, there was no change in deflection within the pressure range of the FESS, 10 Torr.

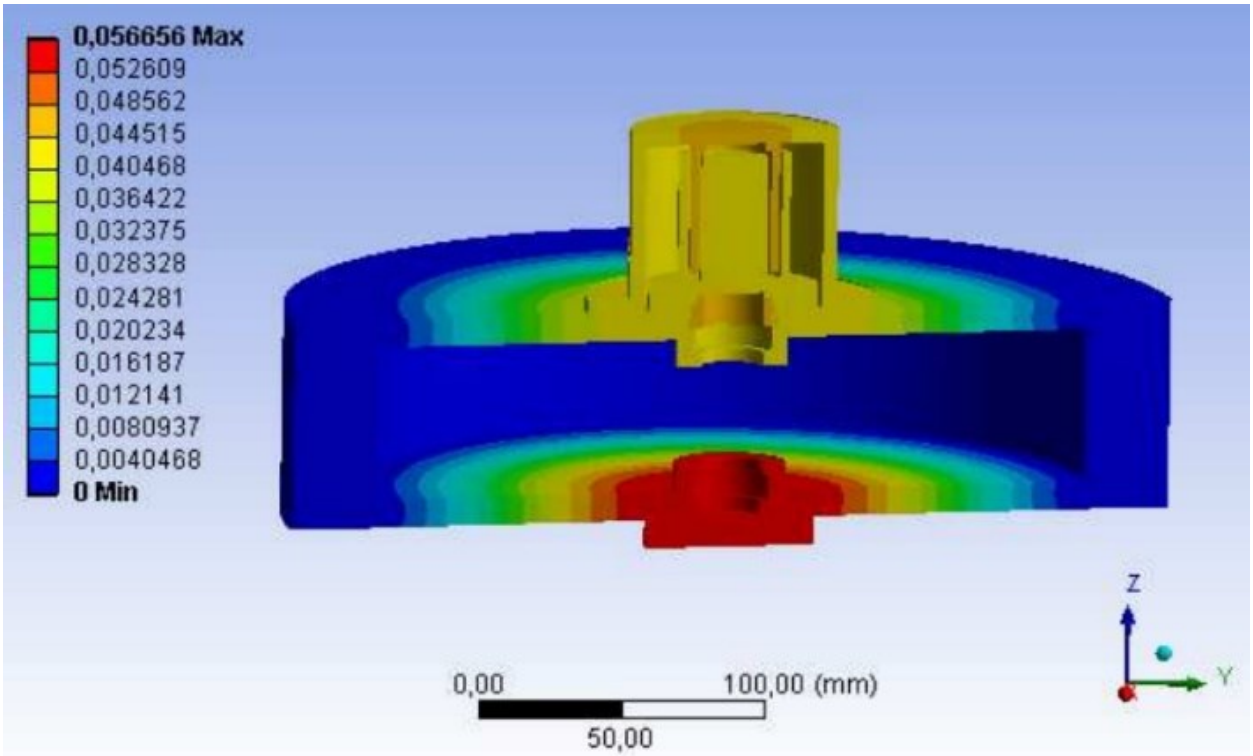

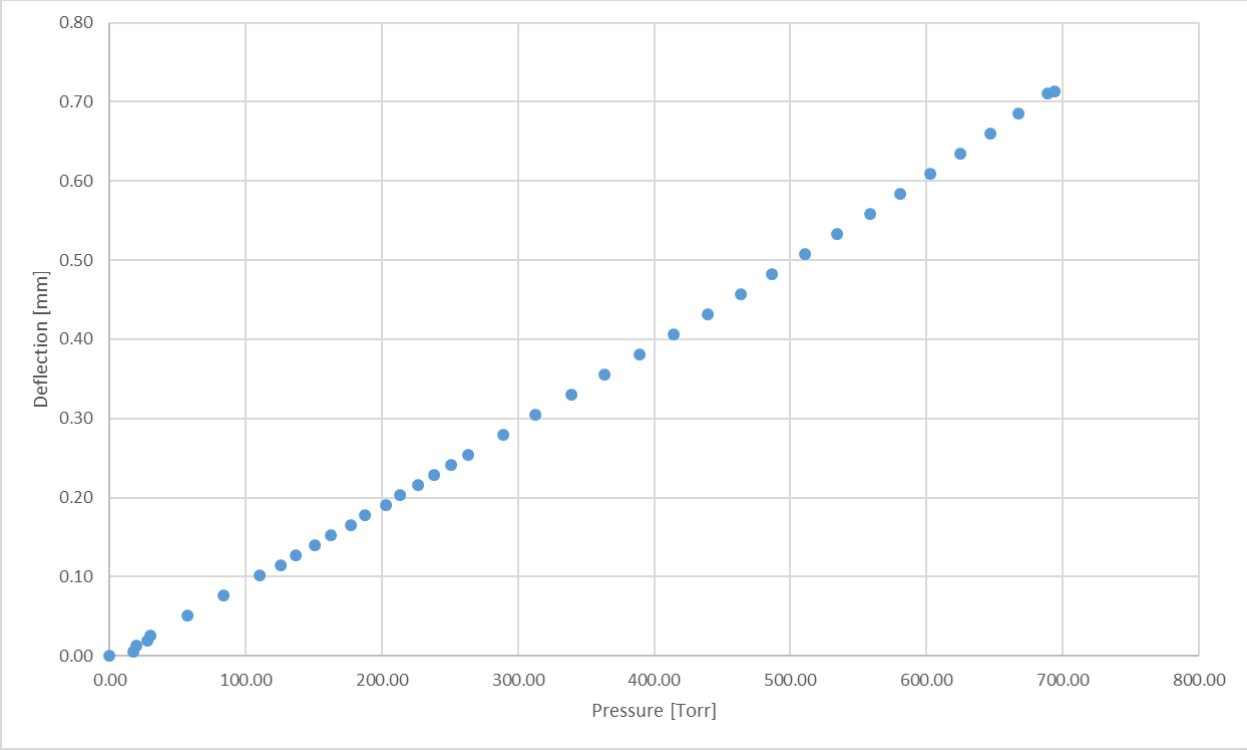

Figure 4: a) Simulation of maximum deflection of the housing under vacuum. [11] b) Deflection testing of the top plate.

3.2 Rotor

The rotor is comprised of two separate rims of dissimilar materials that are assembled with the aluminum hub via press fits. As described earlier, this multi-rim design increases the specific energy density of the rotor and reduces material cost [11, 29, 28] which are key objectives for low cost FESS. The rotor's total mass is 7.75 kg. The outer rim has a maximum radius of 200 mm and inner radius of 170 mm and an axial height of 50 mm. It is constructed from filament-wound AS4C carbon fiber reinforced polymer (CFRP) with a winding angle of approximately 88° (Hexcel, Stamford, Connecticut, United States). The CFRP provides a high stiffness in fiber direction of 128 GPa, providing much of the support and rigidity to the rotor assembly. Additionally, with a density of 1569 $\frac{\text{kg}}{\text{m}^3}$ it accounts for 2.73 kg of the rotor's total mass, 35.2%. The inner rim has a maximum and minimum radius of 170 mm and 100 mm, respectively, and is constructed from filament-would Twaron aramid 2200 aramid fiber reinforced polymer (AFRP) (Teijin, Chiyoda, Tokyo, Tokyo, Japan). This material has good strength in fiber direction, yet, low transverse strength. Its lower cost but reasonable stiffness compared to the carbon fiber makes it a good choice for this application. With a density of 1343 $\frac{\text{kg}}{\text{m}^3}$ the AFRP rim comprised 3.98 kg of the total rotor mass, i.e., 52% of the total mass. The geometrically most complicated component is the rotor hub. Constructed from high strength 7057 aluminum, the hub has a Laval tapered central disk with a 10 mm outer rim cross section. Further, it has an integrated shaft with radial bearing mounting surfaces on the top and bottom, magnetic thrust bearing mounting point at the bottom, and magnetic coupling post at the top. The outer most hub rim is 50 mm in axial height to mount flush with the AFRP composite rim. The central disk is 10 mm thick tapering radially to approximately 6 mm. The hub was thermally fit inside the composite rims by exploiting the significant difference in thermal expansion coefficients between the aluminum and AFRP. The cross section view of the rotor is shown in Figure 5, and the dimensions are given in Table 1. Based on a study conducted by Widmer [45], and reported by Ertz et al. [44], the rotor will experience either fiber-matrix delamination in the fiber direction, or matrix fracture in the transverse direction, both of which are dependent on the fiber-matrix interfacial bond strength.

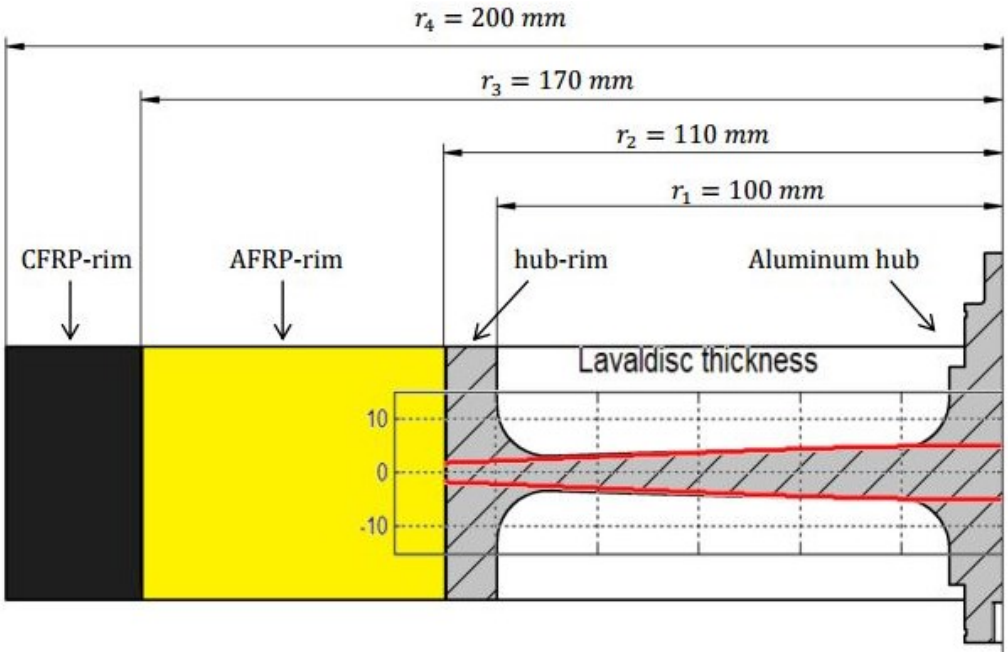

Figure 5: 2D cross section of the rotor including all rims and hub showing the Laval cross section. [11]

Table 1: Flywheel rotor dimensions and material properties.

	Dimension	Unit
CFRP rim		
Outer radius	0.200	m
Inner radius	0.170	m
Density	1569	$\frac{kg}{m^3}$
AFRP rim		
Outer radius	0.170	m
Inner radius	0.110	m
Density	1380	$\frac{kg}{m^3}$
Hub	0.110	m
Density	2700	$\frac{kg}{m^3}$
Height	0.050	m

In a previous rotor design, the magnetic coupling attached to the top of the rotor shaft, Figure 3 part 2, sheared off as a result of cyclic loading. The original design included a necked region where the coupling attached to the shaft with a collet. The shaft sheared off at this neck due to cyclic loading from the electrical machine and rotor harmonics. A new rotor shaft was designed and fabricated with an interchangeable tapered steel stud. The redesigned component can be seen in Figure 6. The tapered steel stud was fitted into the hub to replace the failed section. Tapered shafts are common in many high speed rotating machines, such CNC milling and lathing machines [46, 47], so its application here is reasonable. Tapered shafts also self-aligns concentrically to minimize cyclic loading and vibration, and can efficiently transfer torque between the electrical machine and rotor. The stud was designed with the large diameter of 8.09 mm, a small diameter of 4.76 mm, and a taper angle of 5°. The stud end is threaded to match a tapped hole in the hub to hold the stud in place and provide the necessary axial load to transfer torque from the electrical machine to the rotor. An M3x0.5 bolt is placed in this threaded hole and fixed in place with a thread locking adhesive 12 mm deep. The friction at the interface created by the bolt is larger than the applied torque from the motor, so all energy transfer occurs along the tapered surface, which minimizes the risk of the stud loosening during operation. The taper dimensions are given in Table 2.

Table 2: Tapered stud dimensions.

Feature	Dimension	Unit
Large Diameter	8.09	mm
Small Diameter	4.76	mm
Taper angle	5	degrees
Taper length	19.05	mm
Thread length	12	mm
Thread diameter	3	mm
pitch	0.5	mm

Steel and aluminum were both considered as possible options to construct the stud from. The hub is 6061 aluminum which is important as the interface could be subject to wearing during operation. The most reasonable options were 1018 steel and 7075 aluminum. Both are low cost,

easy to machine, high strength, and moderate to high ductility. Ultimately, the mild steel was chosen because it was more readily available and marginally less expensive than the aluminum. The material properties are given in

Table 3: Material properties of 1018 steel used to fabricate stud. [48, 49]

Property	Value	Unit
Hardness	126	--
Tensile strength	440	MPa
Young's Modulus	205	GPa
Poisson's Ratio	0.29	--
Friction coefficient	0.7	--

The stud is not subject to fatigue failure as the previous shaft was given the new geometry, so the next most significant loading is axial load from the threaded end. The threaded end is necessary to prevent the stud from loosening during operation the interfacial friction must be greater than the torque applied by the motor.

$$T_{\mathrm{f}} < T_{\mathrm{motor}} \tag{4}$$

where T_{f} is the torque acting at the interface due to friction, and T_{motor} is from the motor.

$$T_{\mathrm{f}} = \mu \mathrm{r}_{\mathrm{taper}} F_{\mathrm{N}} \tag{5}$$

To ease the analysis a normal force, F_{N}, was assumed to act half way up the tapered shaft. F_{N} is related to the axial force, F_{A}:

$$F_{\mathrm{N}} = F_{\mathrm{A}} \sin \theta_{\mathrm{t}}. \tag{6}$$

where θ_{t} is the angle between the central axis and the taper wall. Then, the axial force applied by the threaded stud end must be greater than this minimum. The maximum tensile strength for this type of bolt is 400 MPa according to ISO 898-1 standard, provided by AMES [50, 51]. Therefore, assuming this axial stress from the stud, the axial force, F_{A}, is 15.37 kN. Then the normal force, F_{N}, is 1.34 kN. Finally, the maximum tore the stud can transfer, T_{f}, is 3.01 Nm. The magnetic coupling can only transfer a maximum of 1 Nm, so the modified design was determined to be safe.

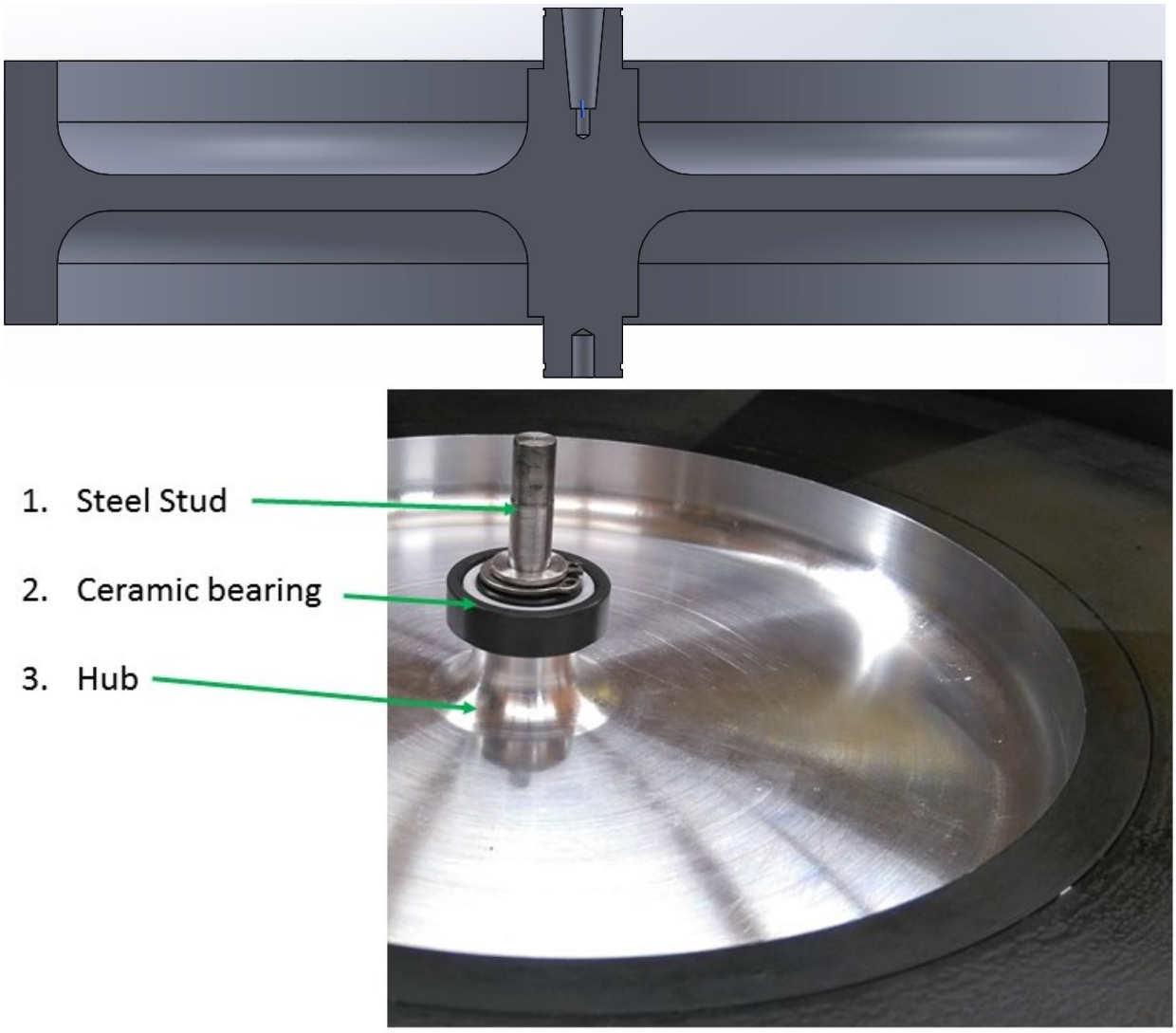

Figure 6: a) Solid model of the hub redesign. b) As manufactured and assembled.

3.3 Bearings

A detailed cross section of the bearing system is shown in Figure 7 The rotor is supported axially by a trust bearing consisting of two permanent neodymium magnets with opposing magnetic fields, and radially by two 6002 full silicon nitride deep groove ball bearings (Bearings Canada Inc, Concord, Ontario, Canada) with a PTFE cage, see items 4 and 5 in Figure 7

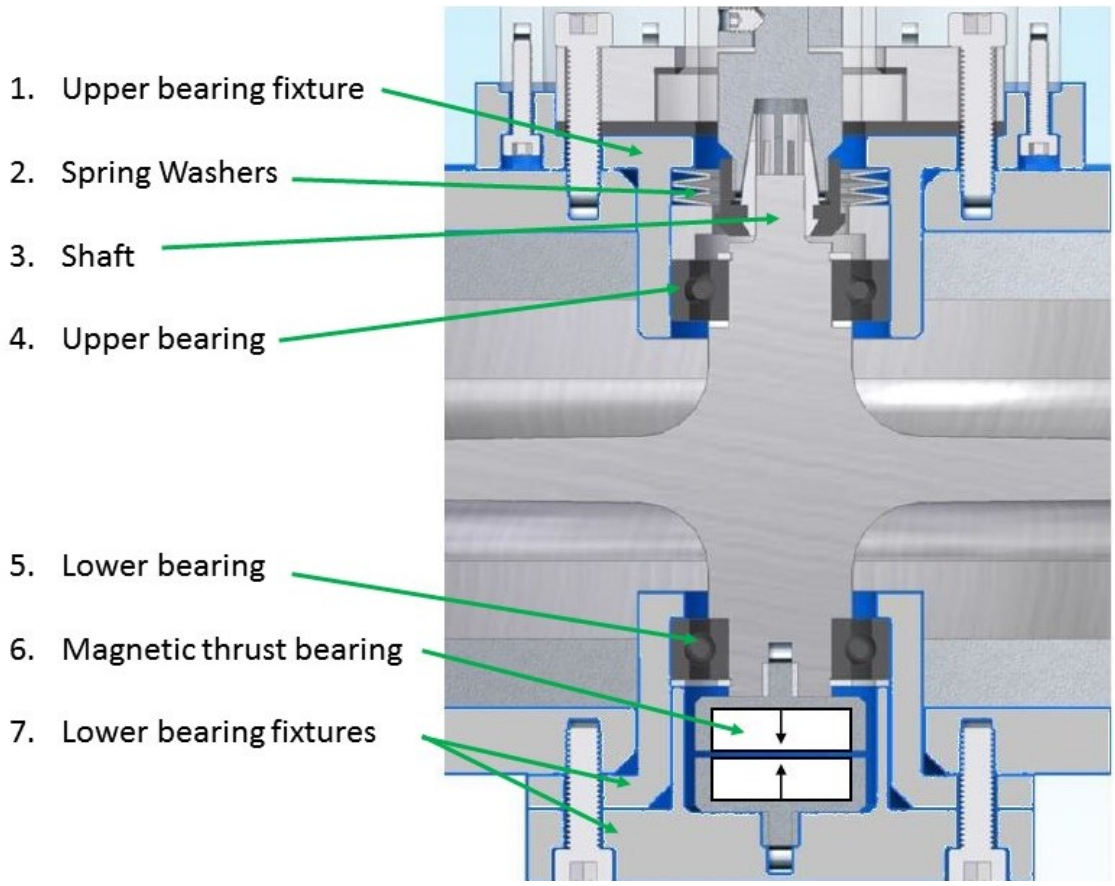

Figure 7: Labeled components for the upper and lower bearing sub-assemblies.

The ball bearing dimensions are 35 mm by 15 mm by 9mm for the outside diameter, inside diameter and height, respectively. The upper bearing assembly has a series of spring washers pressing on the outer race. This axial load is important to stabilize the upper bearing and minimize vibrational loading. In total six spring washers were arranged completely in parallel, meaning they will behave as a single weaker long spring with the measured spring force, to form the spring assembly. The springs can be arranged in series to create a short strong spring. For the spring washers to apply load to the bearings they must be compressed by a lip on the upper bearing fixture, Figure 7 part 1, meaning the spring assembly must be long enough to fill the space between the upper bearing fixture and the outer bearing race. This requirement, in part, dictates the washer's arrangement. Additionally, because any loading on the mechanical bearings increase friction, and therefore passive discharge, the ideal axial load from the springs is the minimum load which mitigates the unnecessary bearing vibration. Based on this two configurations were tested, first, the spring washers were arranged to behave as the longest and

weakest spring possible, i.e. all in series, Figure 8a. Second, the springs were divided in half with three spring washers in parallel to create two moderately strong spring which were then placed in series, Figure 8b.

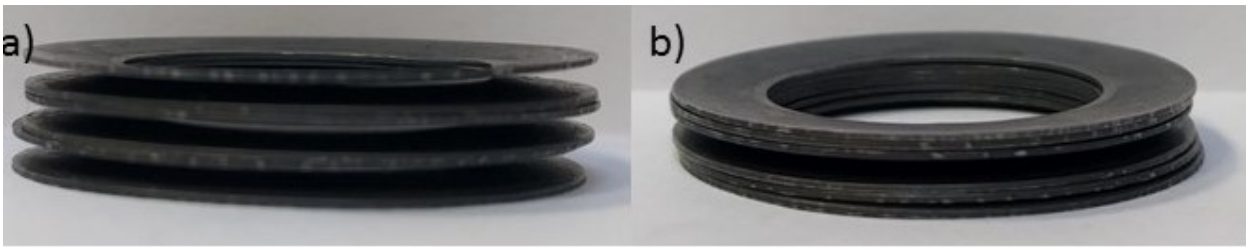

Figure 8: a) First spring washer configuration with all washers in series creating a long relatively weak spring. b) Spring washers in second configuration with two sets of three washers in parallel creating a shorter stronger spring.

The strength of each spring washers was measured using a universal testing machine (MTS 810, Machine Testing System, Eden Prairie, Minnesota, USA), which compressed the springs while measuring deflection and opposing force. The test setup and corresponding results are shown Figure 9 and Figure 10. The testing machine was set to slowly increase the spring washer's deflection until they were completely compressed then slowly decrease deflection. Figure 10 shows the spring deflection along the x-axis, and the resultant force along the y-axis. The two overlapping lines are caused by the testing procedure. They simply indicate the springs are applying equal load while compressing and expanding, as is expected. The second configuration behaves as a much stiffer spring so even small deflections create very large loads, Figure 11. The spring washers in this configuration appear to behave differently while compressing and uncompressing, however this could be caused by small difference in the sets of spring washers. Meaning, one set of washers could begin uncompressing before the other causing the difference seen in the figure. This is unexpected, but does not indicate an error in the measurements.

Figure 9: Test setup for compressive force of spring washers. The washers depicted here are in the second configuration, however the setup is the same for both tests. Same set up is used for magnets

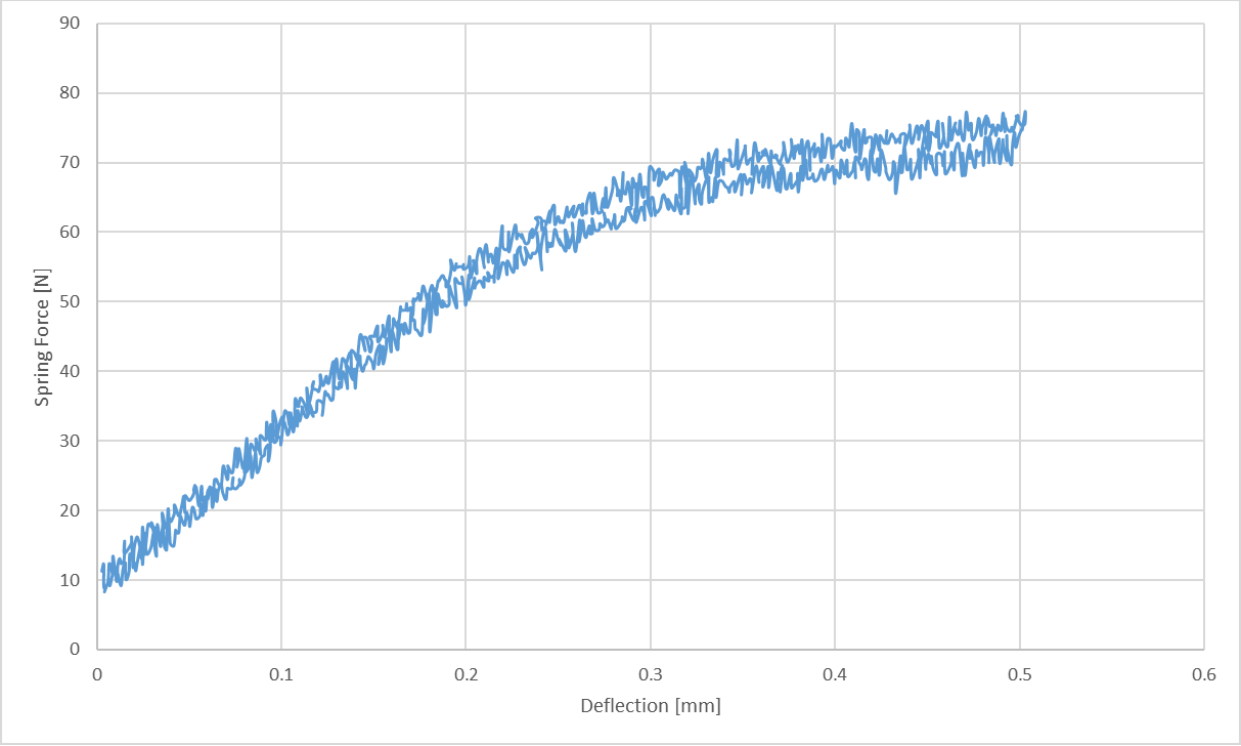

Figure 10: Shows spring washer force vs deflection distance for washers in first configuration. The force while being compressed and uncompressed is shown and is approximately equal as expected.

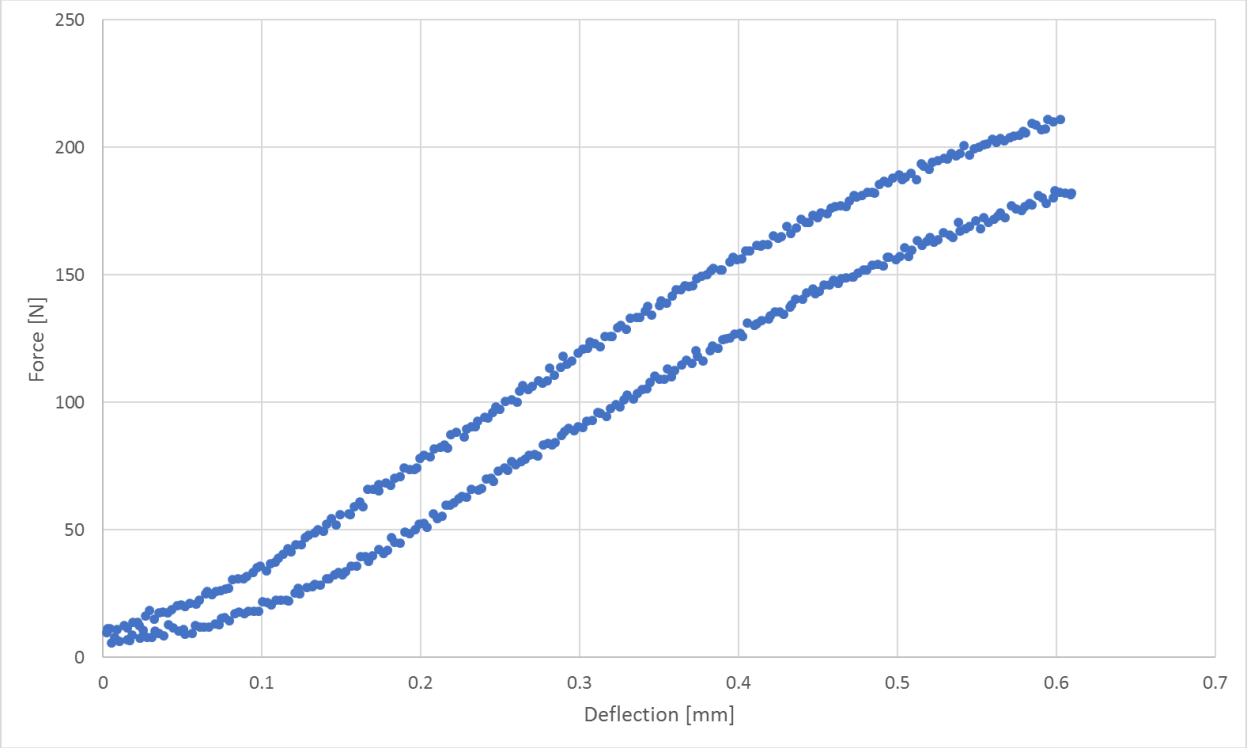

Figure 11: Spring washer force vs deflection distance for washers in the second configuration. Larger variation during compression and expansion, still not unexpected.

From these results, it is clear the first configuration applies lower load at all deflections, so this configuration was chosen.

The magnets of the thrust bearing, item 6 in Figure 6, support the weight of the rotor to minimize rolling friction in the ball bearings. Each magnet is press fit into a steel enclosure which is threaded into the bottom of the hub or the lower bearing fixture. It was discovered during testing that this system does not function exactly as intended for the following reasons. First, and of least concern, the magnetic thrust bearing assembly is not frictionless, since the magnets interact with their surroundings. Due to the high speed rotational motion the magnet assembly generates small eddy currents in the metallic components surrounding them. Associated energy losses are not considered large enough to significantly affect the system, and are likely the smallest sources of energy loss of the FESS device. Secondly, even when perfectly aligned with one another the two-magnet assembly is in unstable equilibrium, so any minor protuberance to the system will cause it to try to collapse. This manifests its self as a radial force pushing the axis of rotation out of alignment which is counter acted by the radial bearings. This will increase the radial force on the bearings and in turn frictional losses. This is considered the

second largest contributor to the mechanical bearing friction. Finally, it was discovered that the thrust provided by the bearing assembly is insufficient to carry the full rotor weight. The relationship of strength versus distance of the magnetic thrust bearing was measured using again a universal testing machine. Corresponding results are shown in Figure 12. where the force necessary to support the rotor is shown as a red line. The data is rather noisy due to measurement errors, but it shows approximate necessary distance necessary to support the rotor. Dimensions of the as-manufactured system were taken to determine actual offset distance, which is approximately 1 mm, see Figure 13 This analysis reveals that the magnets are only able to support between 50% and 75% of the rotor weight, the rest of which must be taken up by the mechanical bearings. This situation is considered the largest source of mechanical bearing frictional losses, which also reduces the lifetime of the bearings. Notable degradation of the bottom mechanical bearing was observed during testing, which is supports the above assumption. The ensure ideal operation the bottom bearing was cleaned or replaced nearly twice as often than the top one forcing the system to require frequent maintenance. Overall, it is currently not possible to quantify the magnitude of forces acting on the mechanical bearings during operation since the bearing fixtures are held rigidly in place. The fixtures and housing would need to be modified to accept an array of load cells which could be arranged to measure the force and quantify these loss effects.

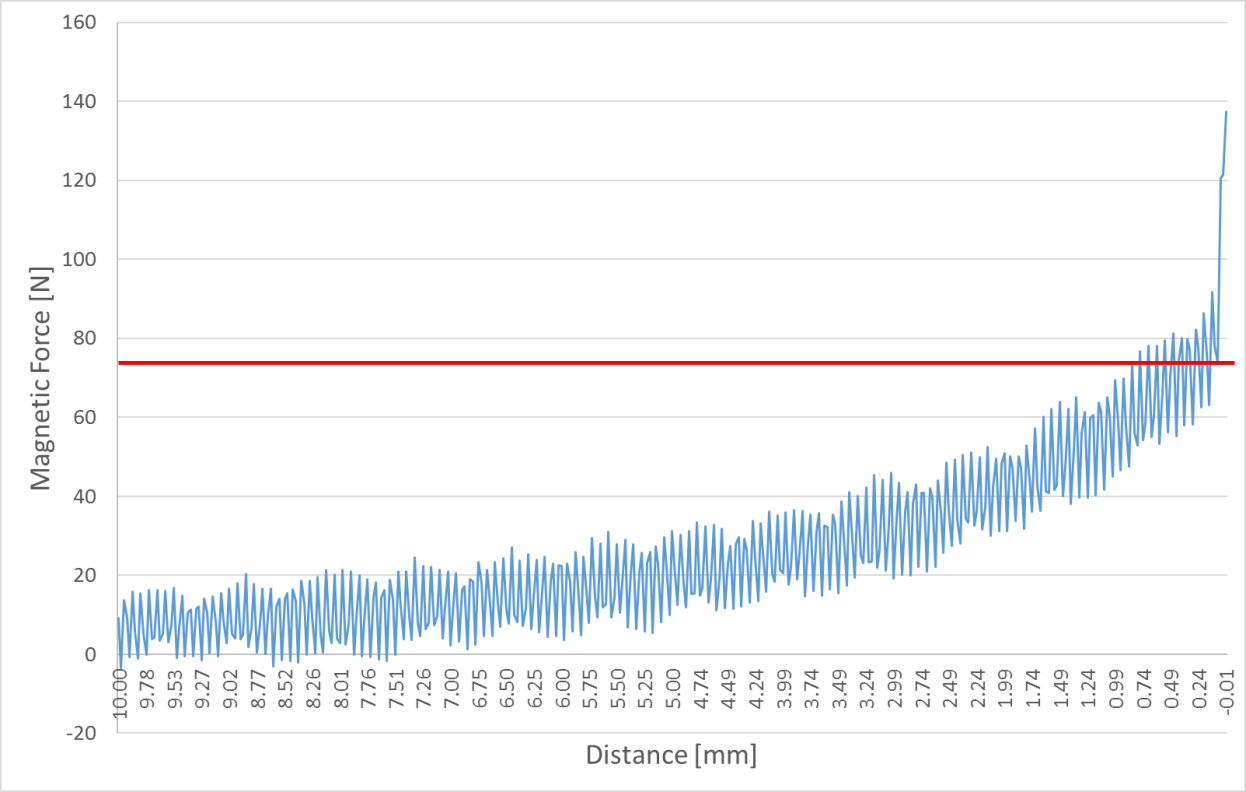

Figure 12: Opposing force compared to distance between the thrust magnets. The red line represents the minimum necessary force to support the rotor.

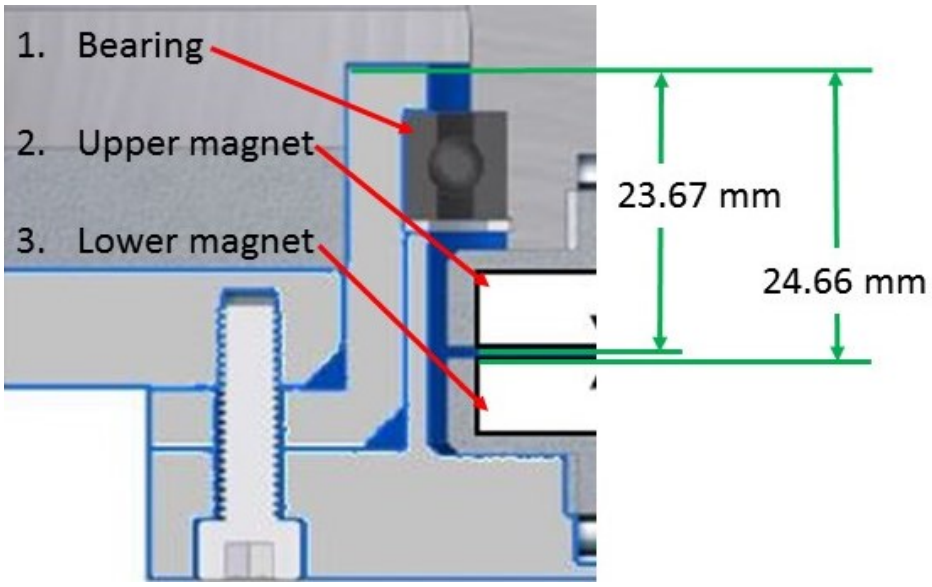

Figure 13: Measurements of the actual distance between the magnets when assembled.

During initial testing the lower bearing experienced significant fretting at the interface between the inner race and aluminum hub. This was unexpected as the radial load on the bearing is relatively low, so wear was not a primary design concern. This caused significant damage to the hub, due to material loss, and the bearing, due to fine particles at the ball-race interface. To mitigate this a plastic spacer was added in between the axial thrust magnet and the bearing inner race, shown in Figure 14. The bearing rests on a shoulder machined into the hub, and the axial thrust magnet threaded into the hub on the other side. Therefore, the magnet and shoulder create a clamping force on the inner race holding it in place and mitigation some fretting. A more detailed discussion of fretting and failure can be found in Chapter 6.

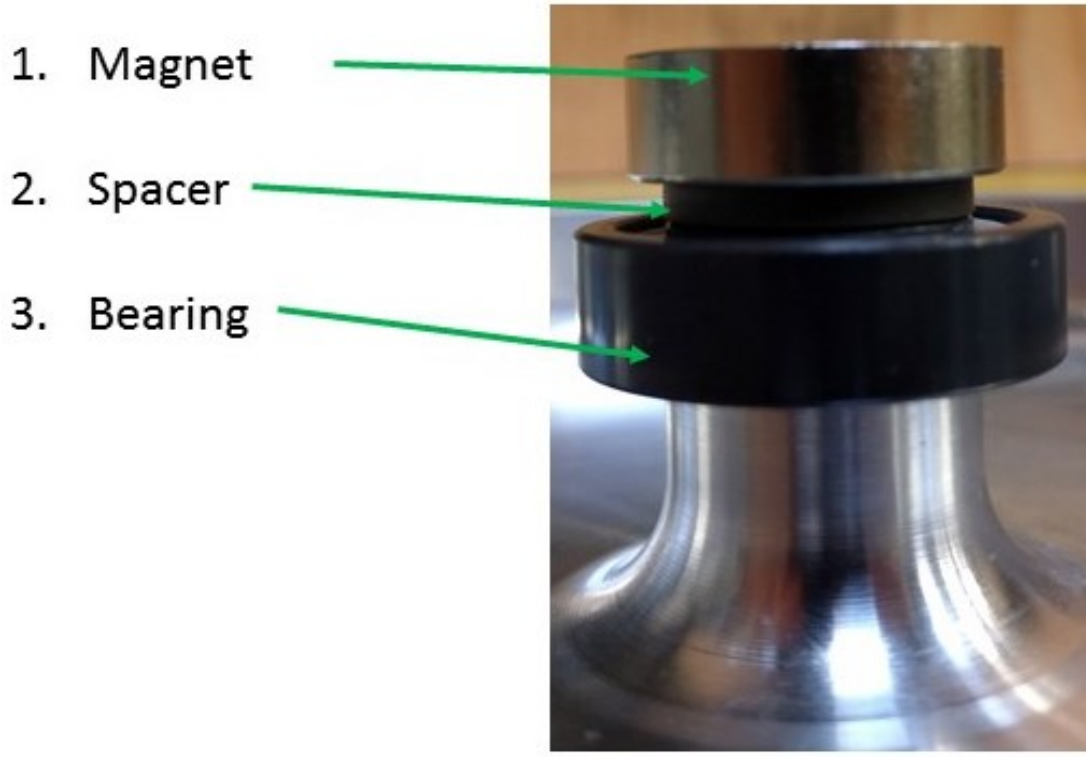

Figure 14: Bottom bearing assembly with the spacer to prevent the race from sliding Note the bearing assembly is shown upside down.

3.4 Electrical System

The electrical system depicted in Figure 15 connects the electrical machine to the power supply or a resistive load, using a set of relays operated by a controller. The relays set the electrical system in either motor, standby, or generator mode. Motor mode connects the electrical machine to the power supply to supply electrical energy to the system. In generator mode, the electrical machine is connected to the load to remove energy from the system. Standby mode

disconnects the electrical machine from both the load and power supply, therefore electrically isolating the electrical machine. In this mode, the electrical machine can spin, but it is not experiencing any load losses.

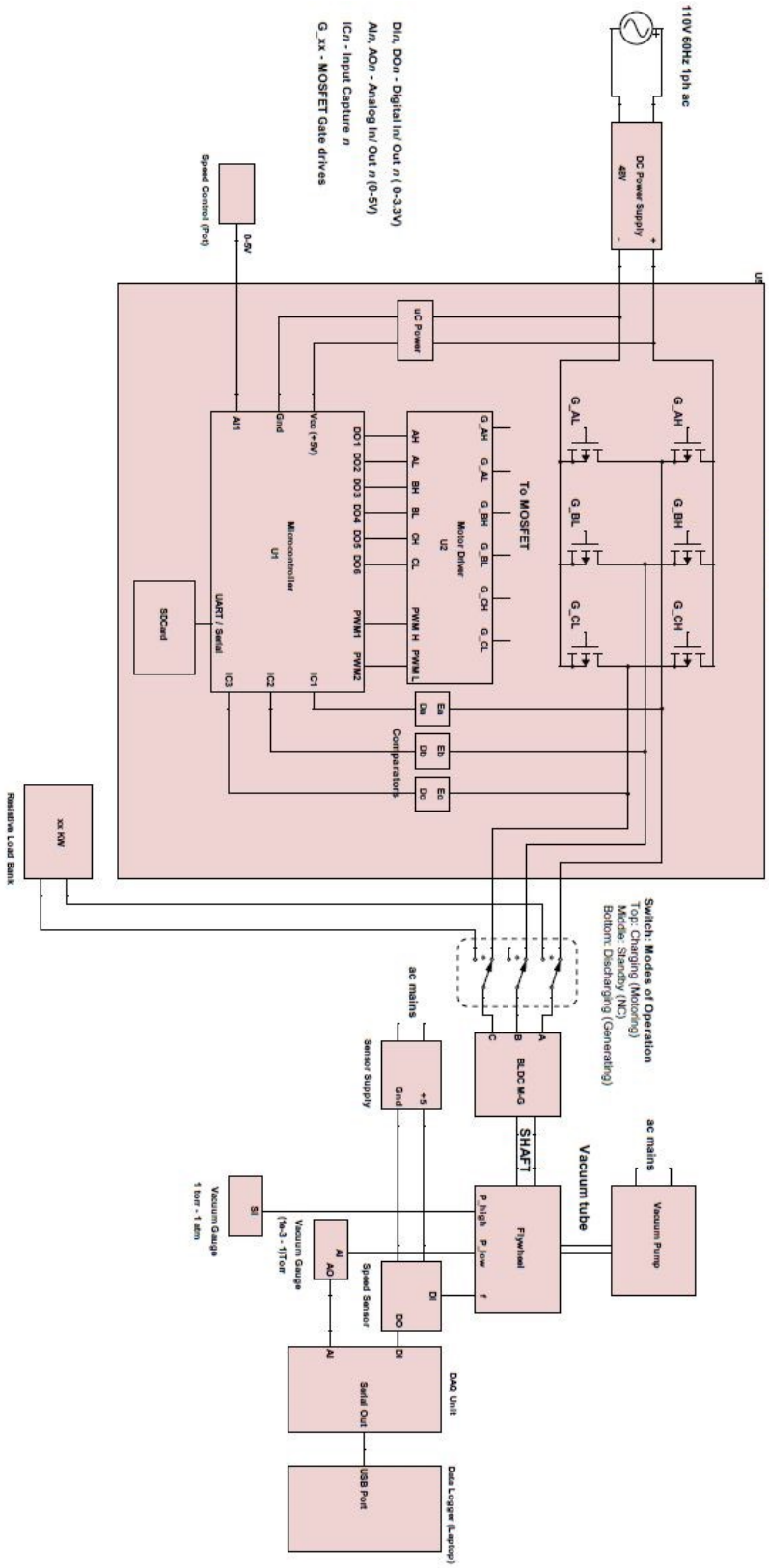

Figure 15: Circuit diagram of electrical system. (Courtesy of Vaishnavi Kale)

3.4.1 Electrical Machine

The electrical machine currently used with the FESS is a brushless permanent magnet (BLPM) three-phase DC motor (Pyro 850-50L, by Kontronik, Rottenburg-Hailfingen, Germany). The motor has a rated speed of 30,000 rpm, a maximum torque of 2 Nm, and maximum power output of 6 kW [52]. Power is supplied to the motor through a Kontronik Kosmik 160 LV electronic speed controller, which in turn is powered by a RT2000 power supply outputting 2 kW at 56V (Lucent Technologies Inc., Murray Hill, New Jersy, USA). The described electrical components are shown in Figure 16.

Figure 16: Primary electrical system components. Left to right, RT2000, Kosmik 160LV, Pyro 850-50

The electrical machine is coupled to the rotor, through the housing, via the passive magnetic coupling seen in Figure 17. This coupling uses alternating poles on to transfer torque between the electrical machine and rotor shaft. In Figure 14 the 'Outer rotor' of the coupling is attached to the electrical machine and 'Inner rotor' is attached to the rotor shaft. These components enable a coupling and decoupling of electrical machine and rotor. The 'flange' and 'canister' shown in Figure 12 are assembled to the housing to provide a vacuum-tight system. Using a magnetic coupling instead of a physical motor-shaft connection simplified the housing design as it minimizes the number of required input/output ports (for electrical connections),

making maintaining a vacuum environment less challenging. In addition, it allows the electrical machine to be air cooled and be removed completely from the rest of the rotating components, eliminating motor losses completely. This feature is highly attractive for the current investigation as it allows loss effects to be isolated. The maximum torque the coupling can transfer is limited based on the strength of the magnets. The coupling was intended to transfer the maximum torque from the electrical machine of 2 Nm, unfortunately, the magnetic coupling is effectively only able to transfer 0.7 Nm.

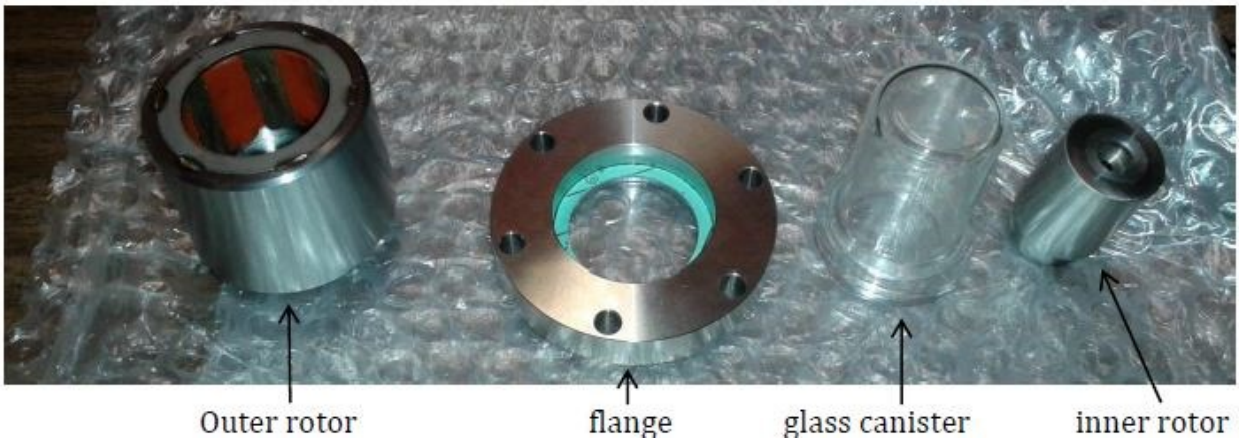

Figure 17: Magnetic coupling components. Outer rotor connects to the motor, inner rotor connects to the shaft. Flange and glass canister maintains the vacuum.

This electrical machine experiences two types of losses. First, load losses occur when electricity is conducted through the machine, either in motor or generator mode, which can be approximated as the electrical resistance of the motor windings and connection wires. This loss scenario can be disregarded as all experiments were conducted with the motor in stand-by mode, so no current was conducted. Second, no-load losses which are caused by electromotive forces (EMF) and mechanical forces. These losses exist any time the motor is rotating irrespective of power flowing or not. No-load losses can be divided into four sources, two electrical and two mechanical. The electrical losses are due to eddy currents, induced in the iron core, permanent magnets, and windings, and hysteresis losses in the iron core. The mechanical losses are due to bearings in the machine and air friction on the motor rotating components. Note that since the motor rotates in atmosphere it experiences aerodynamic drag. This is separate to the air friction the flywheel rotor experiences in the housing of the FESS. For characterization purposes, in

Chapter 4, the four electrical machine loss sources are all be considered together as motor losses. For analytical analysis, only the electrical no load losses were considered.

3.4.2 Instruments and Data Acquisition

The array of holes provided in the top plate, and the acrylic window, function as the input/output ports for the FESS, see Figure 15. The instruments connected to these ports are, from the furthest from the center to nearest to the center, the vacuum pump, a Baratron vacuum gauge (MKS instruments, Andover, Massachusetts, USA), a fine-adjustment needle valve, and a thermocouple vacuum gauge (No.270006, connected to an ionization gauge controller Series 270, Granville Phillips, Longmont, Colorado, USA). The optical speed sensor (OSS) is fixed to the acrylic window. Two ports remained empty and were capped. The vacuum pump is connected via an 8 mm rubber tube and an appropriate fitting. Ideally, the pump can reach a maximum vacuum level of approximately 4 Pa (0.03 Torr). However, miniscule vacuum leaks are hardly unavoidable, and hence, most experiments were conducted above 26.7 Pa (0.2 Torr). The fine adjustment needle valve was used to control the pressure in the system. The valve in combination with the vacuum pump provided an effective pressure range of 4 Pa to 1.33 kPa that accurately be maintained within 0.01 Pa once in equilibrium.

The sensor was connected to dedicated controllers (with the exception of the Baratron gauge), which in turn were read out by a NI USB-6009 data acquisition system (DAQ) (National Instruments, Austin, Texas, USA) and recorded by a computer. A corresponding instrumentation diagram is given in Figure 16.

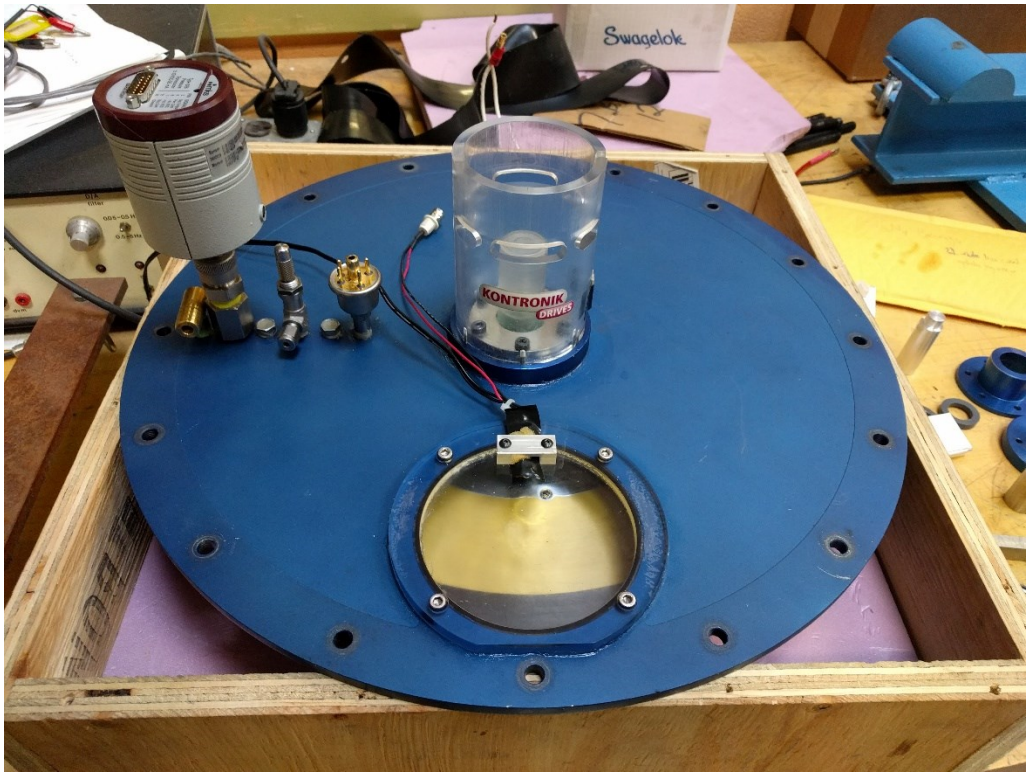

Figure 18: Housing top plate with the sensors in their appropriate ports.

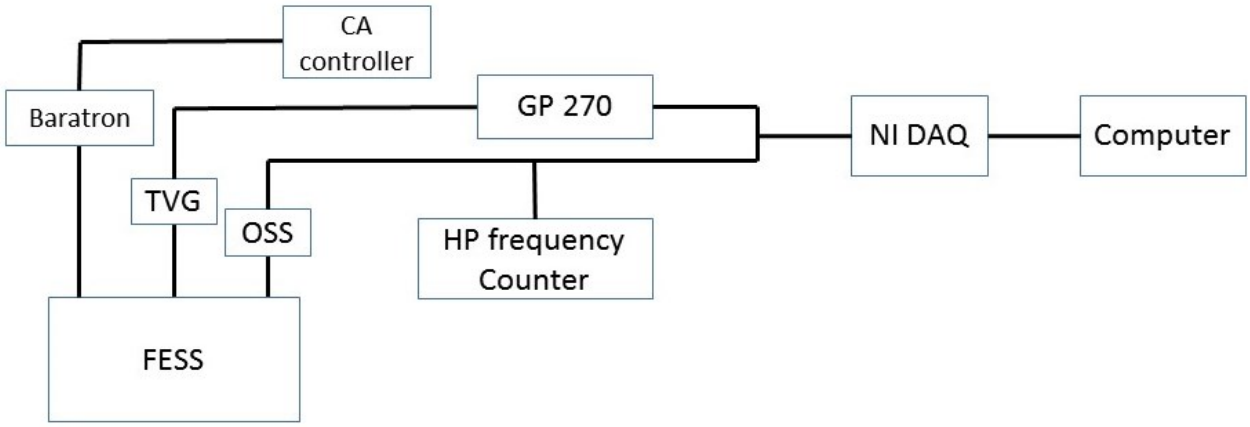

Figure 19: Instrument diagram of the current FESS sensors, controllers, and DAQ

3.4.2.1 Baratron Vacuum Gauge

The pressure in the housing is measured continuously by one of two measurement systems. The Baratron gauge was connected to CA SR5-SP411-11-0 pressure controller, and has an effective range from 1333.3 kPa (1,000 Torr) to 1.3 kPa (1 Torr). Unfortunately, the controller only displays the pressure in psi, and the data is not electronically recorded, however this did not prove to be an issue because all experiments were conducted at equilibrium. The pressure was

manually recorded periodically during an experiment to ensure the pressure remained constant. Combined with the thermocouple vacuum gauge this is seen as sufficient.

3.4.2.2 Thermocouple Vacuum Gauge

The thermocouple vacuum gauge (TVG) is the primary pressure sensor for the majority of experiments. It has an effective range from 1.3 kPa (1 Torr) to 0.13 Pa (10^{-3} Torr). It is connected to a Granville-Philips 270 thermocouple gauge controller for these test. The GP 270 is connected directly to the DAQ to continuously record pressure during the experiments [53]. The gauge applies current to a thin wire to heat it and measures the temperature with a thermocouple, see Figure 17. Air molecules lower the temperature of the wire as they interact with it. The pressure in the system then is found by comparing the temperature recorded by the thermocouple with a standard temperature and pressure. The GP 270 controller outputs the thermocouple voltage to the DAQ, and the manufacturer provided a voltage pressure calibration graph see Figure 18. A series of 13 data points were determined from the graph and high order polynomial fit approximated the given curves. The manufacturer provided minimum and maximum curves for any given pressure value are shown as blue and orange lines, respectively. The pressure given in the unit Torr was then determined as an average of the maximum and minimum values.

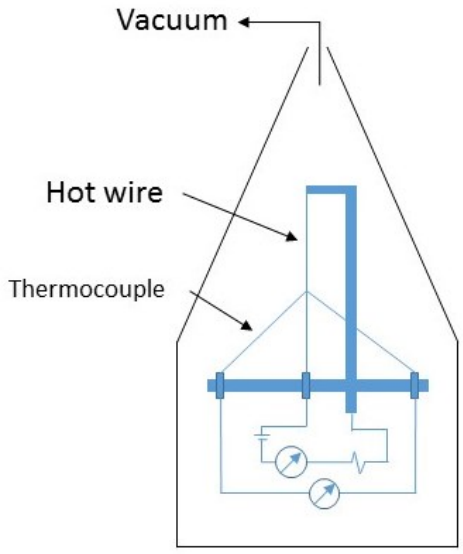

Figure 20: Circuit diagram of a thermal couple vacuum gauge.

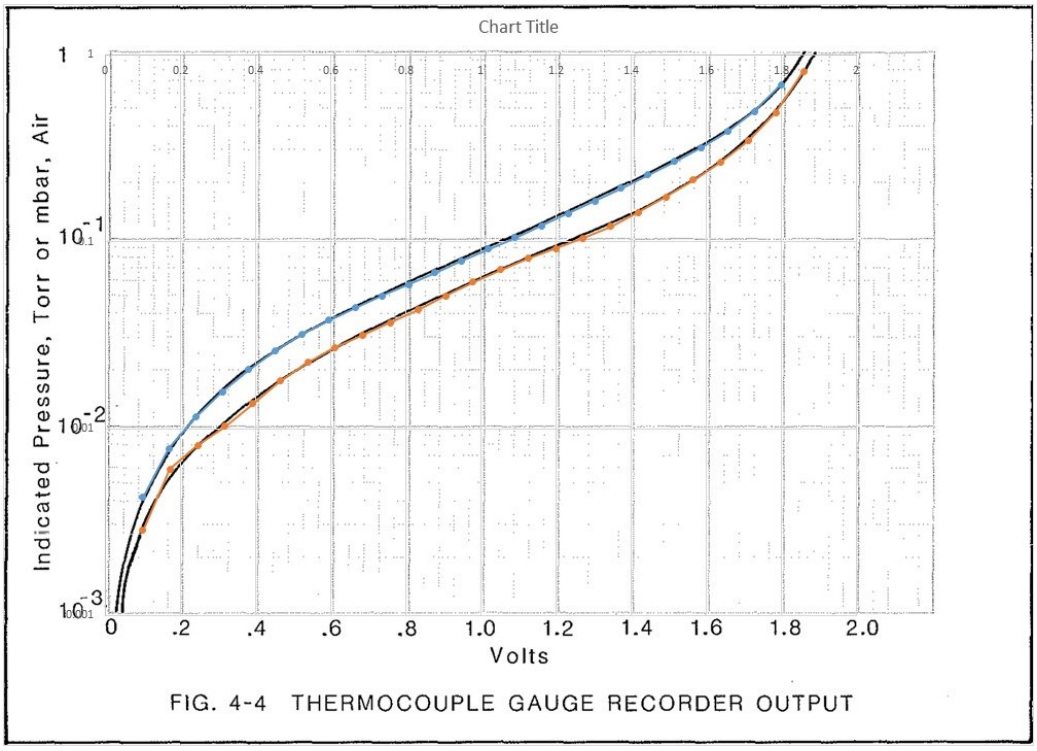

Figure 21: Thermocouple vacuum gauge calibration curves. The blue and orange lines are polynomial approximations of the manufacturer's data. Courtesy of Grandville Philips user manual [54]

3.4.2.3 Optical Speed Sensor

The optical speed sensor measures the frequency of the rotor by recording pulses of light reflected off a small reflective surface on the top of the rotor. One spot on the rotor was made reflective by adhering a small piece of polished aluminum tape to the surface. The sensor is mounted to the window located in the top plate of the housing. The device employs an ultraviolet light emitting diode (LED), a light sensitive diode, and a resistor to regulate power. A diagram of the optical sensor is shown in Figure 19. The two diodes must be adjusted to point at the same location on the rotor so light emitted from the LED will reflect off the rotor and back to the sensor. The housing window has two angled holes to accomplish this. However, it was found that the LED did not produce a reliable signal alone and needed a halogen lamp to supplant the LED signal. The LED in conjunction with the halogen lamp was found to be very reliable as no failures were observed in this system during testing. The light sensitive diode output is a 5 V digital signal when excited, which is directly fed to the DAQ. The latter counts the number of steps in a defined period of time, in this case seconds. Because only one point on the rotor is reflective, this setup directly provides revolutions per unit time. In addition, an HP 5314A

Universal Counter (Hewlett-Packard, Palo Alto, California, USA) was connected to the output of the OSS. This device is optional, but it was found to be a useful tool for comparison between the computer read out, in rpm, and the counter read out in frequency during testing. The values displayed by this machine were not used for the analysis, only the OSS data was processed and analyzed.

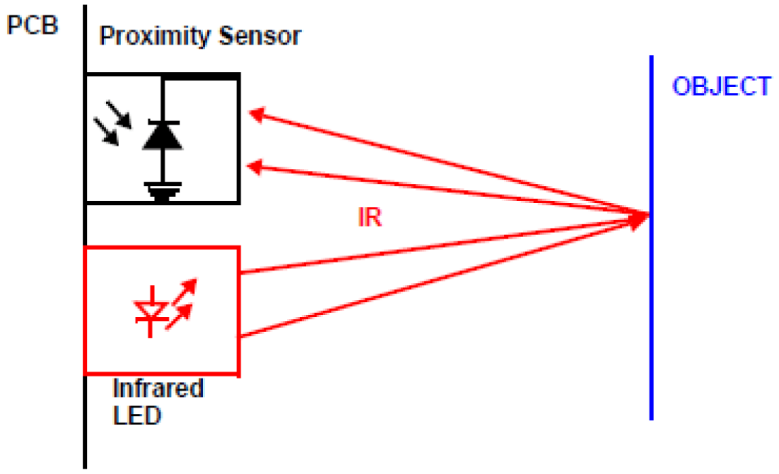

Figure 22: Optical speed sensor diagram.

3.4.2.4 Data Acquisition System

The output signals from the optical speed sensor and the GP 270 controller are interpreted by the National Instruments DAQ. The DAQ monitored one analog signal from the GP 270 controller to record the pressure in terms of voltage, and one digital signal from the OSS. The DAQ interfaces with a personal computer using a program made in house using LabVIEW (National Instruments, Austin, Texas, USA) This program allows the user to decide which data to record, either pressure, frequency or both, the sample rate, and units, either rpm or Hz. This program can record frequency at varying accuracies dependent on the update delay which controls how often the on-screen display refreshes. The default delay is 0.5 seconds and has an associated accuracy of 4 Hz (240 rpm) but increasing the delay to 2 seconds increases the accuracy to 1 Hz (60 rpm). The sample rate can be controlled independently. For this study the sample rate was 1 ms with an accuracy of 1 Hz.

The main screen of the graphic user interface (GUI) is shown in Figure 23. From this screen the data and experiments can be labeled, some data formatting controls are available, and the desired channels to record data from can be selected. The test screen is shown in Figure 24. On this screen the rotor current and average speed is displayed, the current vacuum within the housing, and some display controls are available.

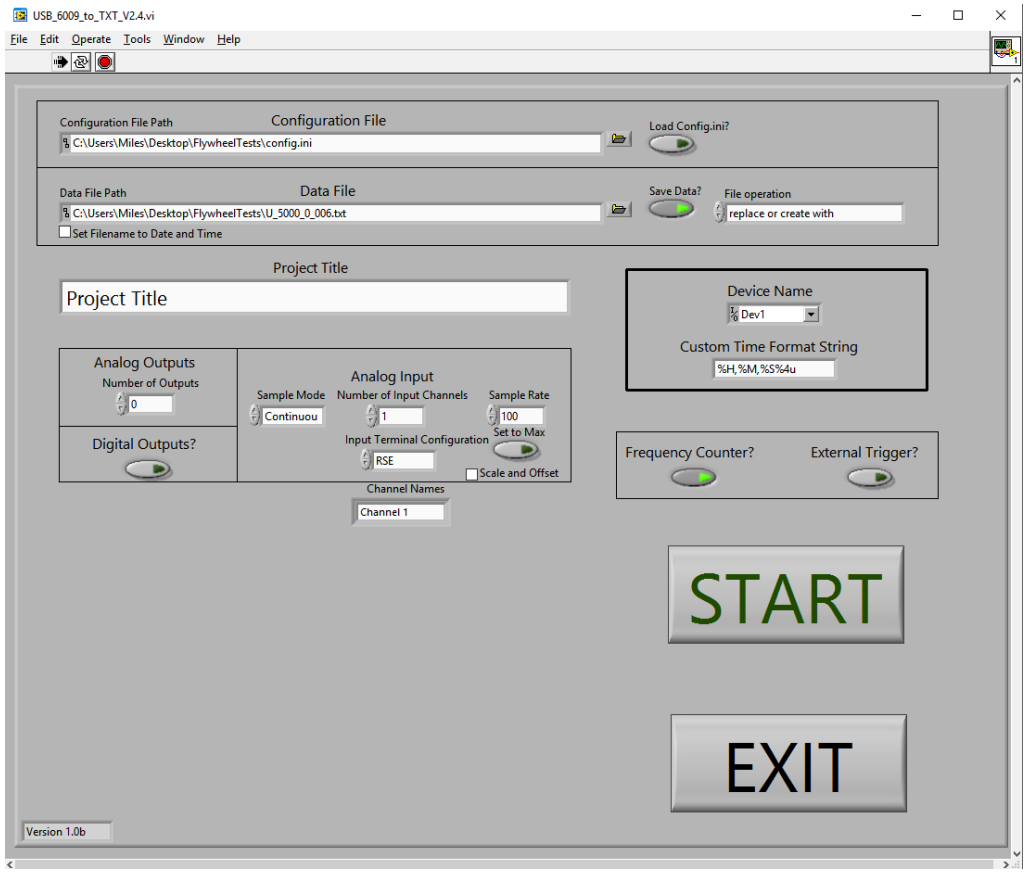

Figure 23: The main screen of the graphic user interface. From this screen desired data, formats, and labels can be defined.

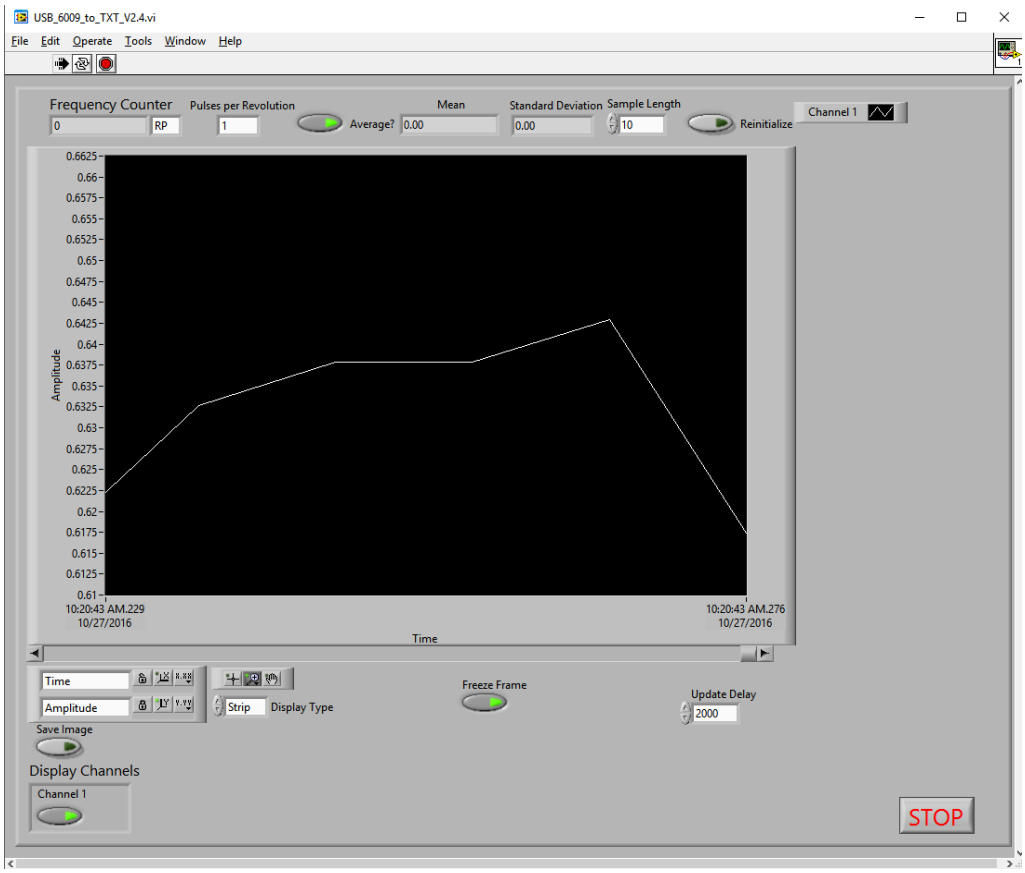

Figure 24: Test screen from graphic user interface. Flywheel rotor velocity and test pressure is displayed here. Some basic controls are available for controlling some display settings.

4 Passive Discharge Loss Analysis and Modeling

The passive discharge in any FESS is caused by three main sources: i) bearing rolling friction, ii) electromotive force losses, EMF, iii) viscus air friction. In the current test setup, the magnetic coupling allows the electrical machine to be physically separated from the rotor and bearing system to eliminate the electrical machine losses, leaving just the air friction and bearing losses. In the following sections, each of these sources is discussed independently along with appropriate models and dependencies.

4.1 Bearing Friction Analysis

Mechanical deep groove ball bearings are designed to support large radial loads and small axial loads. As discussed previously the axial load is relatively small in the FESS, so this load component does not pose a risk of damaging the bearing, however radial loads acting on the bearings are highly cyclical and dependent on the motion of the rotor, the electrical machine, and the magnetic thrust bearing. Considering each of these items individually, the component of the load from the rotor is a combination of the rotor imbalance, misalignment of the bearing, and precession. The rotor was professionally balanced during fabrication, but could have developed a slight imbalance due to time-dependent deformation such as creep. The bearings are aligned based on the concentricity of mounting fixtures which is accurate to within 0.12 mm. Therefore, the effects of precession and other misalignment effects cannot be neglected as these significantly impact bearing losses. Finally, eccentricity effects in the magnetic thrust bearing should be considered. The opposing poles of the two magnets, composing the thrust bearing, create a radial load due to the imbalance of the magnetic field. Assuming the magnets were aligned perfectly concentric they would be in an unstable equilibrium with high potential energy. Perfect alignment is impossible given the loading conditions and errors associated with manufacturing, and hence, the trust bearing system is constantly trying to move toward a lower potential energy state which is resisted by radial forces applied by the mechanical bearings.

There are two main models for analyzing the bearing friction of mechanical deep groove ball bearings: the Hertzian and non-Hertzian methods [55, 56]. The non-Hertzian method is appropriate for any rolling bearing because only material properties and geometry are input parameters are initial inputs. The normal load on a single ball is,

$$F_{\mathrm{N}} = \sum (\int \int p(x', y') dx' dy') \tag{7}$$

where, p is the pressure on each element in the contact region. This is a function of the elastic deformation matrices, *w1* and *w2*,

$$w1_e + w2_e = \frac{1 - \nu^2}{\pi E} \int \int \frac{p(x', y') dx' dy'}{\sqrt{(x - x')^2 + (y - y')^2}} \tag{8}$$

and the total displacement, *d*,

$$[w1] + [w2] = c_{\mathrm{off}} * [K] - ([z1] + [z2]) \tag{9}$$

where [K] is a matrix where all values are 1, and [z1] and [z2] define the initial distance between the contact region and contact body. From the normal force the energy loss to the bearing is,

$$P_{\mathrm{mb}} = \mu F_{\mathrm{N}} r \omega \tag{10}$$

where r is the radius of the bearing. The contact region of the bearing is defined by the elastic modulus and applied load. This is difficult to calculate exactly and will vary with the load, especially with the highly cyclic nature of the FESS. In the present experimental system the force applied to the bearings currently cannot be measured.

The Hertzian method is a well-established rolling friction analysis method derived from the surface contact model of the same name. It uses the applied loads on the surfaces of the bearing rolling elements and races to analytically determine the contact area for each interface based on the deformation of the surfaces. The contact region in a ball bearing is defined as an elliptical region with a major radius a, and minor radius b. The normal stress at any point in the contact region is

$$F_{\mathrm{N}} = \frac{3F_{\mathrm{load}}}{2\pi ab} \left[1 - \left(\frac{x}{a}\right)^2 - \left(\frac{y}{b}\right)^2 \right]^{\frac{1}{2}}. \tag{11}$$

From this the friction force over the contact region of each ball is simply the integral of the normal force over the contact region times the friction coefficient.

$$F_{\mathrm{F}} = \frac{3F_{\mathrm{load}}\mu}{2\pi ab} \int \int \left[1 - \left(\frac{x}{a}\right)^2 - \left(\frac{y}{b}\right)^2 \right]^{\frac{1}{2}} dxdy \tag{12}$$

Then the passive discharge to the bearings can be found from equation (10).

Similar to the non-Hertzian method, the deformation is dependent on the applied load and the material properties. This raises the same issue as with the non-Hertzian method, that is, it is currently not possible to measure the bearing loading.

While either method cannot be used to predict the actual energy loss these models provide guidance in terms of their dependency on different parameters. In general, the bearing loss is given by

$$P_{\mathrm{mb}} = T\omega \tag{13}$$

where torque T is a function of the applied radial and axial load, friction coefficient, and contact region. In the current system, the force is a combination of the rotor precession, radial thrust resulting from the magnetic thrust bearing misalignment, and radial misalignment in the mechanical bearing fixtures. If the bearings were properly aligned, i.e. minimum loss conditions, and with the electrical machine uncoupled, the measured energy loss will have a linear component which can directly be related to the bearing loss. This decouples it from any quadratic, or cubic, components which are associated with air friction and electrical machine losses.

4.2 Air Friction Analysis

The operational speed of the rotor for this study is 5,000 rpm, so viscous air friction around the rotor, and other rotating components, can be significant. The rotor tip speed can be found by multiplying the angular velocity and radius together. The equivalent angular velocity to 5,000 rpm is $523.6\,\frac{rad}{sec}$ and the radius is 0.2 m, so the tip speed is $104.74\,\frac{m}{sec}$. This is approximately 30% the speed of sound in atmosphere. As discussed, the housing maintains a vacuum to minimize these losses and increase performance. Analytical and empirical analysis methods were considered herein to better understand the air friction losses and for comparison with the experimental results.

The analytical approach to determining the air friction losses in a rarefied gas is a non-trivial process dependent on the degree of rarefaction, mechanical properties of the gas, geometry of the surface, and size of the environment as described by Shen [57]. These all affect the characteristic gradients, such as the air density and air velocity gradients, which cannot be measured by the current experimental setup, so these analyses were not attempted. Instead, the theoretical approach presented by Broecker [58] is considered a more feasible approach to

assessing these losses. This model was designed for a rotating disk rotating at high speed inside a housing. Given the close resemblance of the conditions in a flywheel, Ertz [11] adopted this model. Further investigation was deemed necessary to validate its application under the conditions found in the current experimental setup.

The model described by Boecker [52] determines the sum of frictional moments acting on each surface of the rotating disk. The effects of rarefication on the moment are accounted for in terms of density, ρ, the kinematic viscosity, v, and reduced torque coefficient, c_{m}. Ertz adjusted the model for the given design constraints of the system and assumed turbulent flow around the rotor at high velocity. Therefore, the moment acting on the rotor is,

$$M_{\text{total}} = M_t + M_b + M_s \tag{14}$$

where M_{t}, M_{b}, and M_{s} are the moments acting on the top, bottom, and side of the rotor. The top and bottom have the same properties and can be found with,

$$M_t = M_b = \frac{1}{2} c_m Re^{\frac{1}{5}} \rho \left(r_o^{\frac{23}{5}} - r_i^{\frac{23}{5}} \right) \left(\frac{\mu}{\rho} \right)^{\frac{1}{5}} \omega^{\frac{9}{5}}, \tag{15}$$

the Reynolds Number is given by

$$Re = \frac{r_{max}^2 \omega \rho}{\mu}. \tag{16}$$

The FESS, in this study, operates at a maximum of 5,000 rpm (523 sec^{-1}) meaning the Reynolds number doesn't vary much during operation. The maximum Reynolds number is approximately $1.7\mathrm{x}10^3$, and is treated as constant due to the relatively small change in velocity. Additionally, equation (15), takes the fifth root which further reduced the effect of Reynolds number. The torque coefficient, c_m, is empirically derived by Broecker for a range of Reynolds numbers, shown in Figure 25. This figure the Reynolds number is plotted on a log scale while the torque coefficient is linear, so large changes in the Reynolds number relate to small changes in torque coefficient. Further, because the Reynolds number does not make large changes during operation then c_m can also be treated as constant. It must be interpolated as the Reynolds number is outside the given range, and was found to be 0.09.

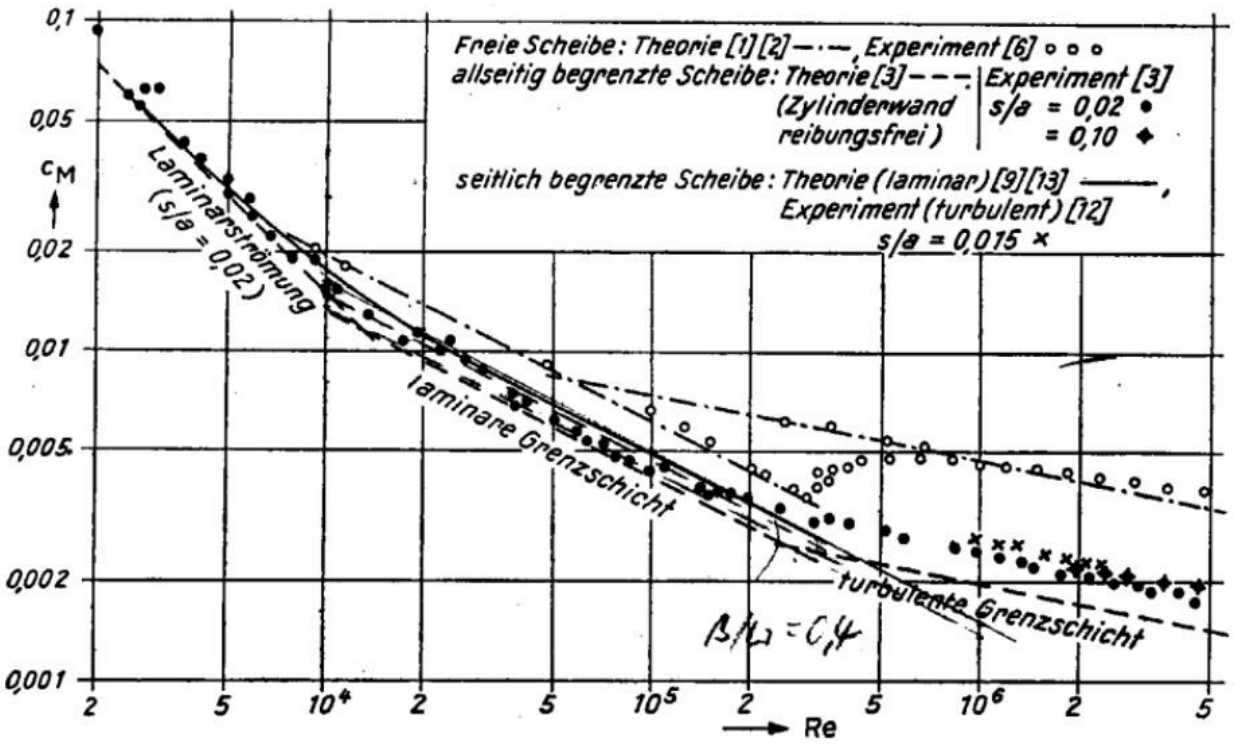

Figure 25:Reduced moment coefficient of rotating disk with respect to Reynolds number. Translating from the original German; Laminarströmung: Laminar flow, Laminare Grenzschicht: Laminar boundary layer, Turbulente Grenzschicht: Turbulent boundary layer. [58]

Finally, the air density is found with the ideal gas law,

$$\rho = \frac{P_r M}{RT}, \tag{17}$$

where P_r is the air pressure, M is the molar mass of air, and T is the temperature. The air friction moment equations can be rewritten by noting that many of these parameters are constant, giving,

$$M_{\mathrm{t}} = M_{\mathrm{b}} = \frac{1}{2} c_m \rho \left(r_{\mathrm{o}}^{\frac{24}{5}} - r_{\mathrm{i}}^{\frac{23}{5}} \right) \omega^2 = C\omega^2 \tag{18}$$

where C is constant. The torque coefficient c_m is dependent on the Reynolds number, but can be thought of as approximately constant within this velocity and pressure range.

The frictional moment acting on the side of the rotor is defined as,

$$M_s = 2\pi r_o^2 h\tau. \tag{19}$$

where τ is,

$$\tau = \frac{M_t}{2\pi\left(\frac{5}{23}\right)(r_o^3 - r_i^3)}. \tag{20}$$

M_s is dependent on M_t so it will have the same form meaning altogether the frictional moment is of the form,

$$M_{\text{total}} = C\omega^2, \tag{21}$$

Finally, the passive discharge to air friction from this model is the total moment acting on the rotor times the angular velocity,

$$P_{\text{air}} = C\omega^3 \tag{22}$$

This form is useful for comparing effects between models, discussed in this chapter, and experimental results, discussed in the next. This is similar to the passive discharge for the ball bearings, however it is cubic with velocity rather than linear. Therefore, with no electrical machine losses, the passive discharge will identify the primary effect. If the FESS discharge is more linear or more cubic then the primary source of passive discharge losses is either the bearings or air friction respectively. Additionally, by monitoring the losses as pressure varies it is possible to determine if the primary source changes under different operating conditions. The model from Broecker was validated against other theoretical models, and experimental results for a laminar flow, however it showed some deviation under turbulent flow. The Broecker model was designed for application in flywheel systems, and given the accuracy he demonstrated, this model was deemed appropriate for the conditions in this study.

4.3 Electrical Machine Losses Analysis

The electrical machine losses are unique in that they are more subjective to this specific FESS than the other sources of passive discharge. All silicon nitride bearings will behave similarly, and air friction will interact with a moving object in the same way for all systems, but permanent magnet electrical machines vary wildly between manufacturers and designs. The electrical machine losses only affect the current experimental setup when the electrical machine is coupled to the shaft; otherwise the electrical machine losses are zero. When coupled, the employed DC motor can operate in motor mode, accelerating the rotor and adding energy to the

system, or as a generator, decelerating the rotor and removing energy, or in stand-by mode when it is doing neither.

Electrical machines will experience no-load and load losses during operation. The no-load losses are due to magnetic losses and mechanical friction. The load losses come from the flow of electricity through the machine and are a function of the electrical resistance of the materials, and stray current. The load losses are due to the electrical resistivity of the material used in the stator and rotor windings, expressed as

$$P_r = I_{\text{amp}}^2 R = \frac{V^2}{R}. \tag{23}$$

Stator and rotor winding resistive losses generally contribute 47 – 57% of the total losses, and when combined with stray current are approximately 67% of the total electrical machine losses [59].

The no-load losses from mechanical friction are due to the bearings in the electrical machine upon which the rotor turns, and air friction around the electrical machine rotor. When the electrical machine is coupled to the flywheel rotor shaft, air friction is turbulent. Fins on the backside of the employed DC motor, visible in Figure 16, are designed to draw air into the DC motor housing for cooling. This high-speed turbulent flow is very efficient at cooling, however air flow around the rotor is limited by the electrical machine fixture seen on top of the housing in Figure 3. This housing is necessary to align the machine and allow it to couple and decouple from the rotor, however it can cause the motor to heat up during operation due to less efficient heat convection away from the windings. During testing this was only noticeable while it was under load, and the windings were under electrical load.

The analysis of the mechanical losses, i.e. air friction and ball bearings, in the electrical machine is similar to that of the flywheel rotor air friction and bearings as discussed in Sections 4.1 and 4.2, so they will not be discussed here. The magnetic induction of electromotive forces (EMF) in conductive components generates eddy currents and hysteresis due to the changing magnetic field. The *EMF* losses in the electrical machine rotor and stator iron cores are,

$$P_{\text{core}} = k_h B^2 f + \left(\frac{1}{6}\right)\pi^2 a^2 \sigma V_{\text{c}} B^2 f^2, \tag{24}$$

The k term is calculated by curve fitting the iron loss data from the manufacturer to determine hysteresis losses. The eddy current losses in the core, from the second term in equation (24), are dependent on the square of the electrical frequency where the hysteresis is linear. This highlights an interesting relationship between the no-load losses, and decouples them in the same way was the air friction and bearing losses. The eddy current losses associated with the permanent magnets is,

$$P_{\mathrm{pm}} = \frac{V_{\mathrm{pm}} b_{\mathrm{pm}}^2 B^2 f^2}{12\rho_{\mathrm{pm}}}. \tag{25}$$

The permanent magnets do not experience hysteresis losses because they are due to the magnetic field changing faster than the magnetic induction. The magnetic field is constant so the hysteresis losses are zero.

The strength of the magnetic field, B, of each magnet is typically known design parameter for DC motors, but the manufacturer would not disclose this value during this study, so it was not possible to calculate the losses analytically. However, the above equations emphasize the relationship between key parameters. Similarly, to the bearing losses, the electrical machine losses have a linearly term and a quadratic term based on the electrical frequency, f, so the measured losses should follow this relationship. It should be noted here again that during this study the electrical machine is only operated in stand-by mode, and all four unique no-load loss are collectively referred to as electrical machine losses.

5 Results and Analysis

5.1 Experimental Design

The three sources of passive discharge losses, i.e. bearing friction, air friction, and electrical machine losses, are treated as independent variables for characterization. The bearing losses are herein considered to exist at all times and to be only a function of rotational speed since they cannot actively be varied, so only one state exists. The electrical machine can either be coupled or uncoupled, giving two possible states. All experiments were conducted at a maximum of 5,000 rpm (523 sec^{-1}). Finally, the vacuum pressure inside the flywheel housing can be varied continuously, yielding a complete mapping of the functional space, however, this is unnecessary. As was discussed previously, the FESS was designed to operate at moderate vacuum levels, so four pressures were chosen to test at giving four states. Thus, four vacuum states are defined, the minimum state at 27 Pa, a low state at 66 Pa, an intermediary state at 133 Pa, and a maximum state at 1,333 Pa. Given the relatively small functional space and independence of passive discharge loss sources, full factorial experimentation was determined to be the most practical experimental method. This process involved keeping one variable constant and sweeping through each possible state of the others, giving six unique experiments as shown in Table 4. More experiments were conducted with the electrical machine uncoupled than coupled because electrical machine losses mask the other losses. Additionally, many FESS discussed in literature operate at vacuum levels below the minimum, so it was reasonable to focus more on these low loss conditions. Each experiment was repeated in triplicate with the exception of the 1,333 Pa condition which only has one repetition. This organization isolates each source from facilitating comparisons between sets for characterization.

The chosen experimental design assumes that neither the existence nor magnitude of one passive discharge loss source does not affect any of the others. That is, the minimum passive discharge loss, i.e. bearing losses at minimum pressure, is constant across all experiments, so any measured losses at a maximum pressure are entirely due to that change in pressure. Similarly, the energy lost to air friction at a given pressure within the housing is constant with the electrical machine coupled or uncoupled.

Table 4: List of experiments to independently characterize each source of passive discharge losses.

Angular Velocity [rpm]	Electrical Machine Position	Air Pressure [Pa]	Test Repetitions
5,000	Uncoupled	27	3
		66	3
		133	3
		1,333	1
	Coupled	66	3
		133	3

5.2 Data Reduction Scheme

For any energy storage system it is important to determine the amount of energy in the system after any time, *t*. In a FESS the rotor practically provides all the energy storage capacity for the system, and is scalable to tailor the system to a specific application. The method chosen herein for assessing the three sources of passive discharge losses is therefore based on the quantity of energy stored in the flywheel rotor for a given time during the experimentation. The kinetic energy of the rotor can be determined by

$$E_{\text{stored}} = \frac{1}{2} I_{\text{total}} \omega^2 \tag{26}$$

where E_{stored} is the kinetic energy of the rotor (in Watts), I_{total} is the rotor moment of inertia, and ω is the angular velocity in radians per second. The moment of inertia depends of the rotor geometry, so calculating it analytically may be non-trivial for complex shaped rotors. The total moment is the sum of the moment of inertia of each component, which in the present case encompasses the rims and the hub, see equation (27). The rims are simply thick walled cylinders for which the moment of inertia can be determined using equation (28).

$$I_{\text{total}} = I_{\text{hub}} + \sum I_{\text{rim}} \tag{27}$$

$$I_{\text{rim}} = I_{\text{cyl}} = \frac{1}{2} \rho \pi h (r_o^2 - r_i^2)(r_o^2 + r_i^2) = \frac{1}{2} \rho \pi h (r_o^2 - r_i^2)^2 \tag{28}$$

where ρ is the density of the material in kilograms per m^3, h is the rotor height in meters, and r is the cylinder inner or outer radius (in meters) denoted by the subscripts 'i' or 'o', respectively. The moment of inertia of the more complex hub geometry was approximated considering a thick-walled cylinder connected to a solid disk, as indicated by equation (21). The total moment of inertia for the hub is,

$$I_{hub} = \frac{1}{2}\rho\pi h {r_\mathrm{i}}^4 \tag{29}$$

Given the dimensions of the rim and rotor in Table 1 the moment of inertia used in this thesis for the flywheel is 0.814 kg·m^2. This was compared to a model of the rotor created in the SolidWorks design software (Vélizy-Villacoublay, France) yielding an error of 0.03 kg·m^2 between the analytical and numerical models. This is due to the simplifying assumptions made in the analytical calculation of the moment of inertia, in particular, assuming that corner radii have a negligible effect on the moment of inertia. Equations (26) to (29) demonstrate the most efficient approach for increasing the energy capacity of the rotor, that is, to increase the rotor radius and angular velocity as much as possible (since these variables affect the rotor kinetic energy quadratically). However, doing so will significantly increase the induced stress in each rim as seen in studies conducted by Foral et al. [26], Gabrys et al. [14], and Ha et al. [30]. The volumetric mass density of fiber-reinforced composite materials is relatively low compared to metals, and hence, composites may intuitively not be the ideal choice as a rotor material. However, their ability to sustain high stresses in fiber direction allows the design of rotors with larger diameters and higher allowable velocities, making energy density of composite rotors greater than that of rotors made of isotropic materials.

The next step of the chosen data reduction scheme is determining the energy loss per unit time and unit velocity from the rotor angular velocity (or frequency) recorded during the experiments and calculated kinetic energy data. Focusing on losses per unit time and velocity is useful for comparing various operating conditions and predicting performance. The energy stored at a specific time, E_{stored}, can be expressed as the initial energy, E_{start}, minus the energy lost, E_{loss}, to air and mechanical bearing friction, E_{air} and E_{mb}, and electrical machine losses, E_{EM}, see equations (22) and (23).

$$E_{\text{stored}}(t) = E_{\text{start}} - \Delta E_{\text{loss}} \tag{30}$$

$$\Delta E_{\text{loss}} = \Delta E_{\text{air}} + \Delta E_{\text{mb}} + \Delta E_{\text{EM}} \tag{31}$$

For the example of air friction, the losses are the rate of energy loss per time over a given time, i.e.

$$E_{\text{air}} = \int_{t_1}^{t_2} \frac{dE_{\text{air}}}{dt} dt \tag{32}$$

where E_{air} is the energy loss during an instant of time. Hence, the time-differential of E_{air} is the power loss or passive discharge, P, to a specific source, i.e.

$$\frac{dE_{air}}{dt} = P_{air} \tag{33}$$

Determining the passive discharge is highly desirable because it can be used to compare different discharge sources and determine the kinetic energy, that is, the energy stored in the flywheel, after a given period of time. Relationships similar to equations (32) and (33) can be established for E_{mb} and E_{EM}. The passive discharge is obtained from experimental data by,

$$P_{\text{air}} \cong \frac{E_{\text{air}}(t_1) - E_{\text{air}}(t_0)}{t_1 - t_0} \tag{34}$$

With the passive discharge defined the baseline losses are,

$$\frac{dE_{\text{baseline}}}{dt} = \frac{dE_{air}}{dt} + \frac{dE_{mb}}{dt}. \tag{35}$$

Then, by varying parameters individually, it is possible to determine the rate of losses for a specific source. For example, if two experiments are conducted at the minimum pressure, with the same bearings and starting velocity, where the electrical machine is coupled in one and uncoupled in the other case, then the electrical machine losses are given by

$$P_{\text{EMF}}(\omega) = P_{\text{coupled}}(\omega) - P_{\text{uncoupled}}(\omega) \tag{36}$$

where P_{EMF} is the passive discharge from all sources while the electrical machine is coupled to the system and is dependent on angular velocity. This is reasonable because air pressure and

bearing friction are constant across both experiments, making the electrical machine losses the only independent source. A similar process can be followed for any two experimental data sets were the source of interest is the only independent variable to determine the rate of passive discharge and magnitude of losses after any time.

The first step is to determine the minimum losses present in the system. That is, with all other losses eliminated the baseline will be the only remaining source. For this system, the electrical machine is decoupled making EMF losses zero leaving only some air friction and bearing losses. The bearings only exist in one state so the air pressure will determine the minimum losses. The first step is to measure the losses at each pressure, then find a relationship between pressure and passive discharge. The minimum point is estimated to represent the pressure independent losses, and are taken as the baseline losses.

5.2.1 Baseline Losses

The kinetic energy storage time at each pressure state is one of the primary characteristics for the FESS and is of concern when designing energy storage systems. The rotor energy vs time is given in Figure 26. Also on this figure is the point where half the kinetic energy has been discharged, called the half-life. The average total storage time and half-life time for each condition is given in Table 5.

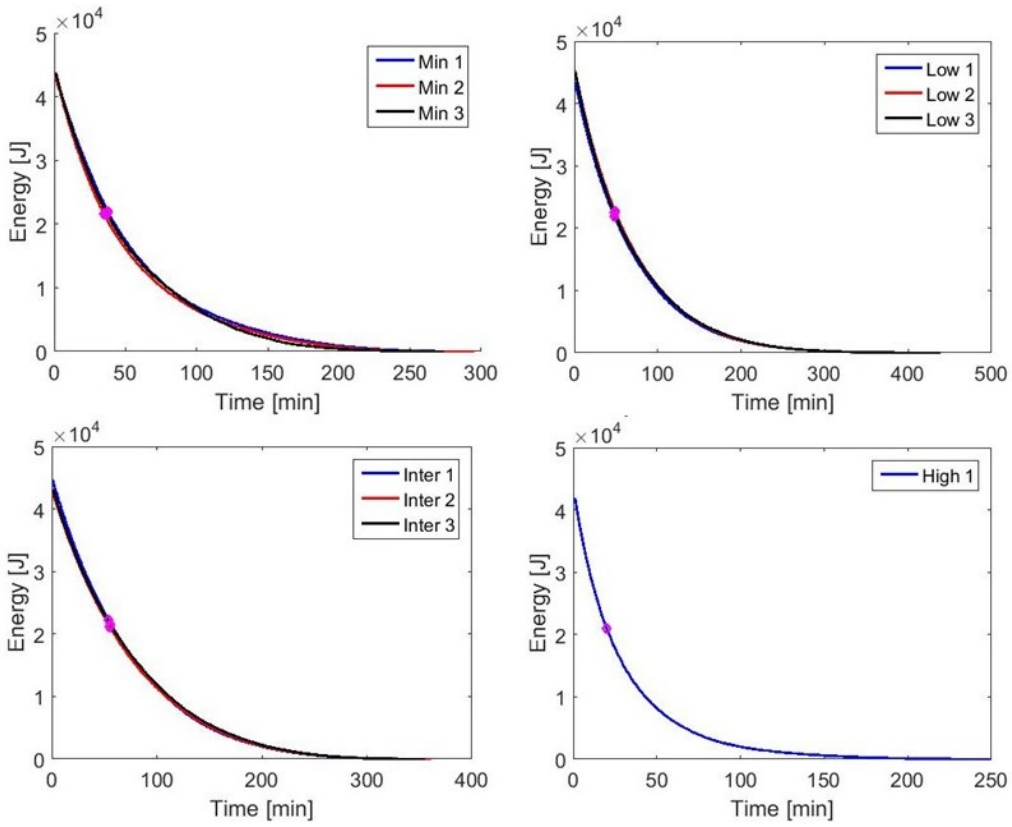

Figure 26: Rotor kinetic energy vs discharge time for all four pressure states. The half-life is also given as a point on each figure. The minimum is top left, low is top right, intermediate is bottom left, and high is bottom right.

Table 5: Rotor kinetic energy total discharge time and half-life time for all for pressure states.

	Pressure [Pa]	Half-life [min]	Total [min]
Minimum	27	36.7	275.3
Low	66	48.5	450
Intermediate	133	55	357
High	1,333	20	250

The intermediate state has the longest half life time showing it has the lowest initial rate of passive discharge, however the total discharge time is shorter than the low pressure state. This results will be discussed in more detail later.

Measuring the passive discharge losses begins with the rotor velocity which is measured with the OSS continuously during experimentation from which the kinetic energy can be calculated with equation (26) to yield Figure 27b. Here the low pressure state loss calculations are used to demonstrate the analysis process, in later sections the given passive discharge values are found using this process.

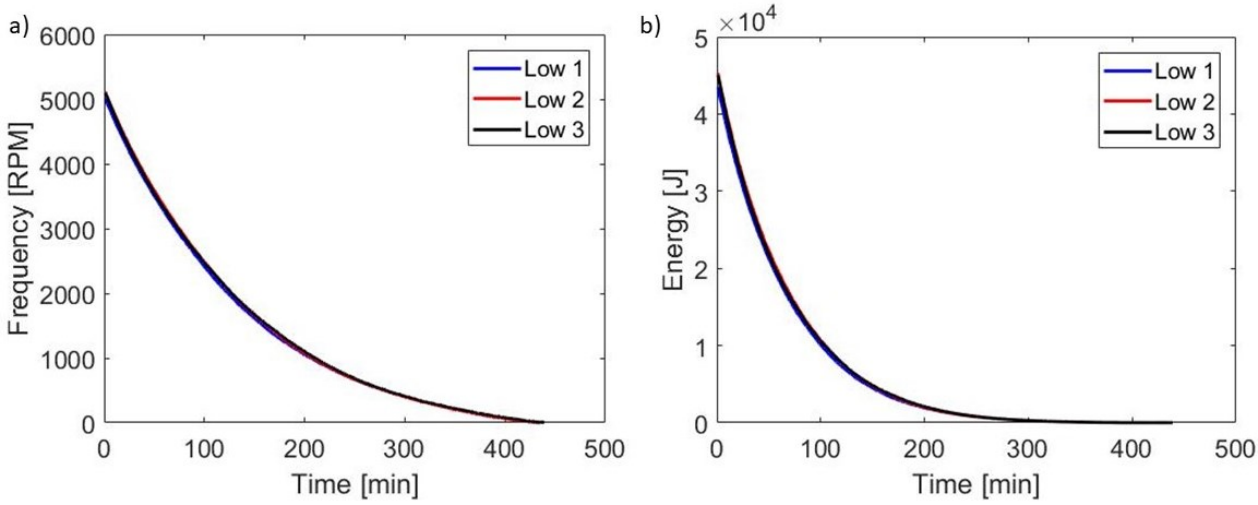

Figure 27: Low pressure experimental results for a) Rotor frequency in rpm vs time in minutes, and b) rotor kinetic energy [J] vs time in minutes.

This figure above shows experimental data for the low pressure state from three identical experiments. In Figure 27a, the rotor frequency in RPM is given on the vertical axis with respect to time. Figure 27b gives the corresponding kinetic energy with respect to time. This data is very consistent with all three experiments reaching completion in 450 minutes, 7 hours 30 minutes, within approximately three minutes of each other. Then the passive discharge is found according to equation (34) which is shown with respect to time and angular velocity, Figure 28.

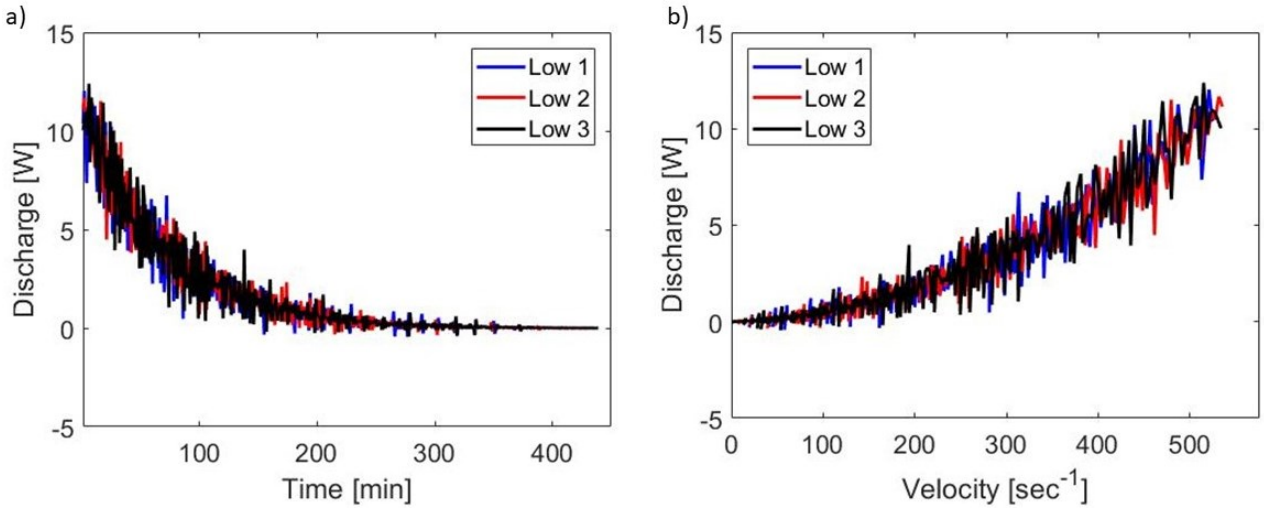

Figure 28: Low pressure a) passive discharge [W] with respect to time [min] and b) passive discharge [W] vs angular velocity [sec^{-1}]

The passive discharge in this figure is the total discharge, not the losses due to one specific source. The magnitude of energy loss in each unit time is highly variable, as evidenced by the noise introduced during differentiation which may be an indication of high cyclic loading during operation. That is, the non-constant applied load varies the energy lost to the bearings, thus creating the non-constant passive discharge seen in Figure 28 above. Cyclic loading was significant enough to damage previous iterations of the rotor hub, and could manifest itself in the power loss data at relatively large variations in power loss per unit time. To quantify losses by velocity rather than time, and as a means of comparison between experiments, the passive discharge is plotted over angular velocity. Finally, all three models in chapter 4 show that passive discharge is a function of angular velocity, therefore fitting the data to these curves is reasonable.

The noise in the data makes comparisons between data sets challenging, so it was necessary to find a best fit approximation to represent each experiment. Considering the analytical models discussed in chapter 4 all the losses are a set of constants – such as mass, geometry, surface conditions, motor components – multiplied by the rotor frequency to an unknown power, giving,

$$P = \alpha\omega^{\beta}. \tag{37}$$

This empirical approximation allows the constant and exponential coefficients, α and β respectively, to take any value which best represents the data. The curve fitting algorithm in

MatLab's curve fitting toolbox was used as it contains a robust non-linear least squares regression method. The fit is obtained using the least absolute residuals (LAR) method which minimizes the absolute difference of the residuals to minimize the influence of outliers. This method is preferred when the data has few outliers [60]. Looking at the plots of the data in Figure 28 the data is noisy, but contains few spikes outside the range of normal values so the LAR method is appropriate.

The noisy passive discharge data was averaged together, as an unweighted average, to reduce random error. This method seems appropriate because each individual data set is a repetition of the same condition on the same systems, therefore the only differences should be random error which is reduced by averaging. The results for the low pressure state are shown in Figure 29 along with the best fit approximation. The ability for the best fit curves to accurately represent each data set is determined by the goodness of fit parameters: Sum of Squares due to Error (SSE), Adjusted r-squared (Adj-r^2), and Root Mean Squared Error (RMSE). These values for the low pressure approximation shown above are given in Table 6.

Table 6: Goodness of fit parameters for low pressure, 66 Pa, best fit approximation showing the model well represents the experimental results.

Parameter	Value
SSE	0.659
Adj-r^2	0.9998
RMES	0.039

An SSE less than unity suggests low random error effects while the Adj-r^2 and RMES approach unity and zero respectively suggests a high fit quality and low standard deviation meaning this approximation is the best representation of the data obtainable. Through the same process the net passive discharge at each pressure can be determined. The results for the other three states are plotted in Figure 29 to Figure 32, and the statistical parameters are given in Table 7.

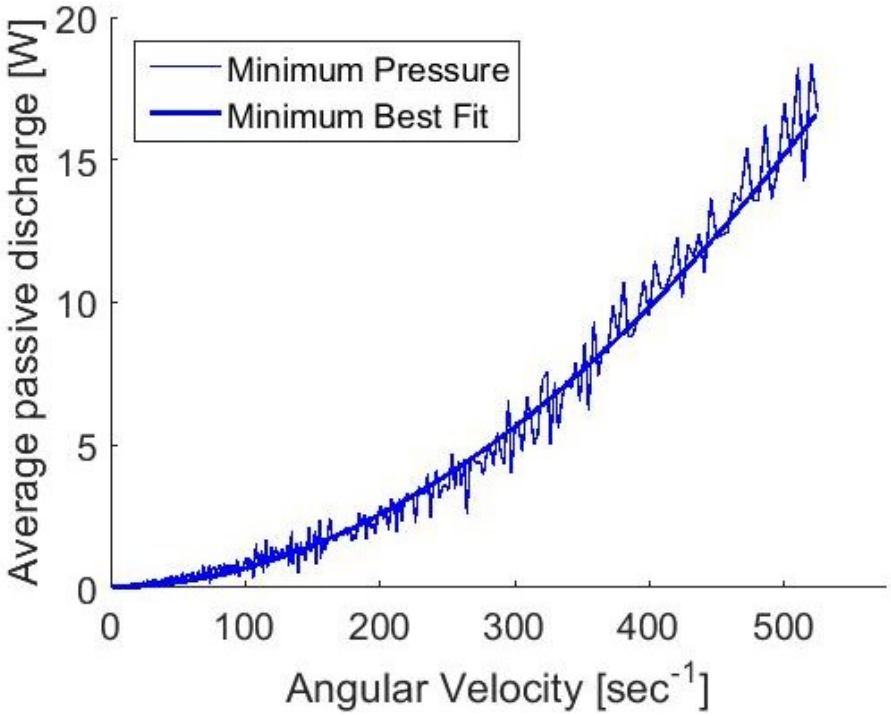

Figure 29: Minimum pressure, 27 Pa, average passive discharge losses and best fit approximation.

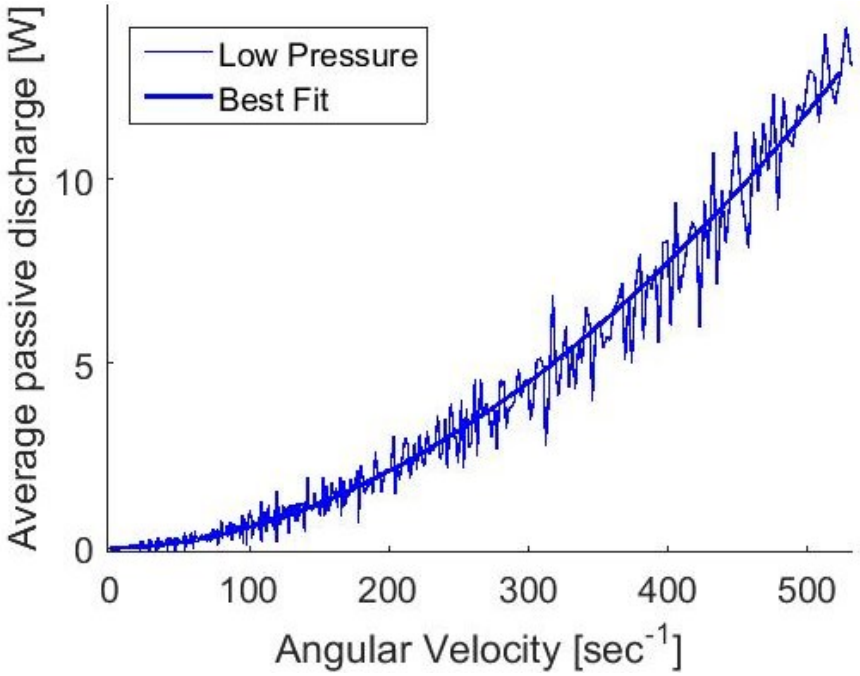

Figure 30: Low pressure, 66 Pa, average passive discharge results plotted with the best fit approximation.

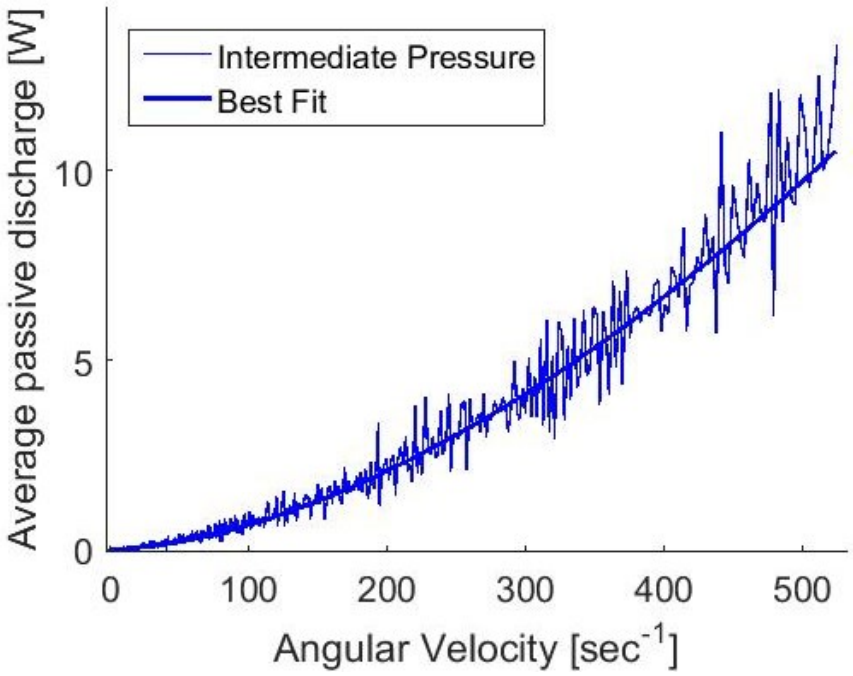

Figure 31: Intermediate pressure, 133 Pa, average passive discharge losses and best fit approximation.

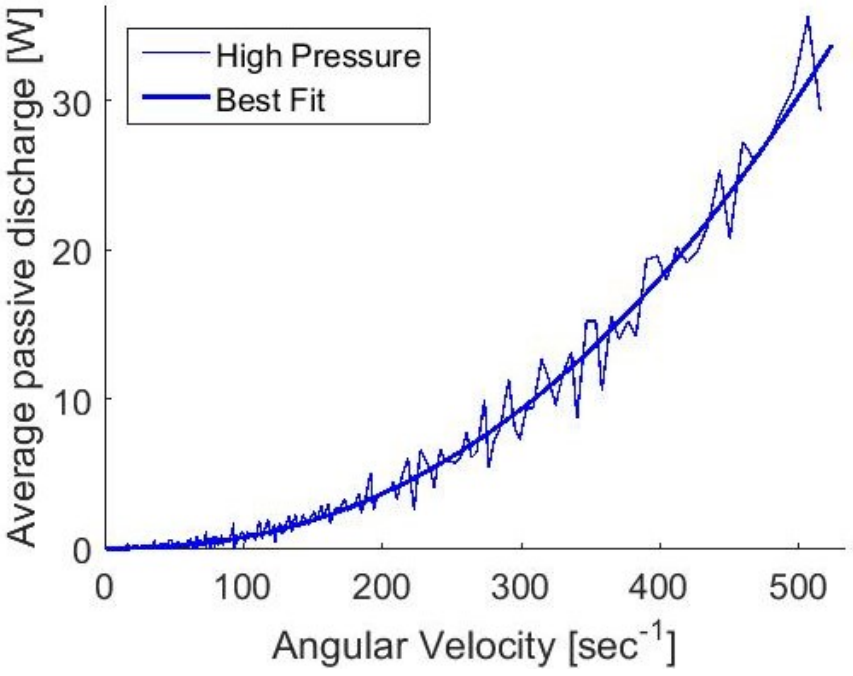

Figure 32: High pressure, 1,333 Pa, average passive discharge losses and best fit approximation.

Table 7: Statistical goodness of fit parameters for average passive discharge losses for minimum, intermediate, and high pressure states.

	Minimum	Intermediate	High
SSE	0.803	1.006	1.802
Adj-r^2	0.9998	0.9995	0.9997
RMSE	0.0535	0.0529	0.0852

The statistical parameters indicate the best fit approximation accurately represents each data set suggesting they are appropriate for modeling and predictions. The minimum state is well fitted, shown by the Adj-r^2, and a small standard deviation, shown by the RMSE. The SSE show minimal random error effects. The intermediate approximation fits the data very well in all categories. Finally, the high pressure state has the most influence from random errors, seen by the SSE and RMSE, likely due to only conducting one repetition at this pressure state.

These models are approximating the total passive discharge losses, so a relationship between discharge and pressure can be found to determine the pressure independent losses. The discharge at a variety of speeds is given in Figure 33. The dashed lines in this figure are included to identify a trend in the measured data assuming a linear relationship between pressure in passive discharge losses.

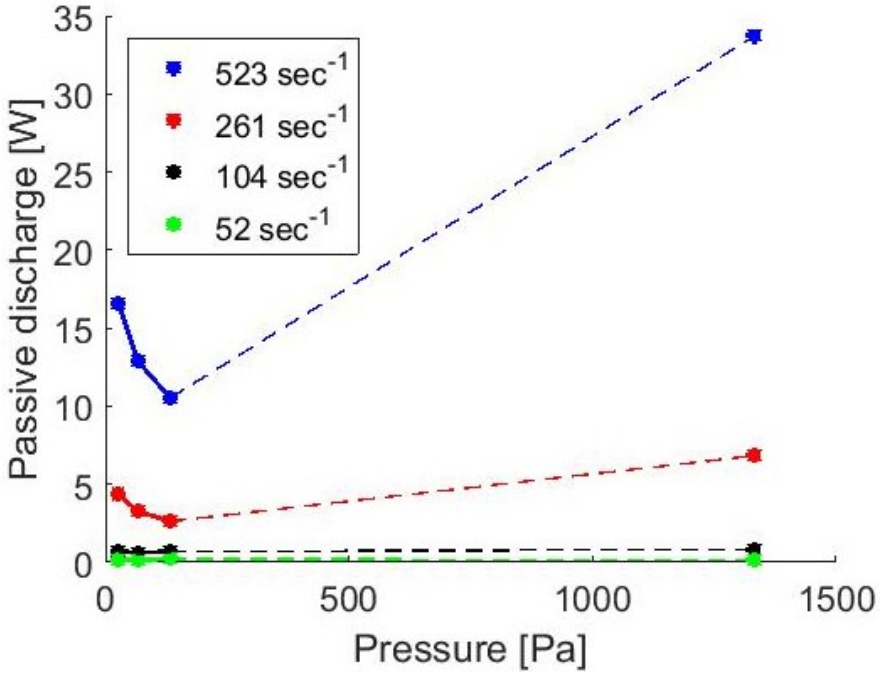

Figure 33: Total rotor passive discharge vs air pressure at four rotor speeds in RPM. The dashed line in the figure assume a linear relationship between pressure and passive discharge losses, and are included to identify a trend in the measured data.

The angular velocity can be introduced to Figure 33 above to observe the effect of pressure and velocity on the rotor passive discharge, Figure 34. The passive discharge in this figure is taken from the best fit approximations at four rotor speeds during testing. The minimum losses occur at 133 Pa which is the intermediate pressure state. This is unexpected as the minimum losses should occur at the minimum pressure state according to the air friction model discussed in chapter 4. This was initially suspected to be caused by a failure in the vacuum housing during operation, or another systematic failure. However, as shown in Figure 35, the pressure remained constant and at the appropriate level during the low and minimum pressure state experiments.

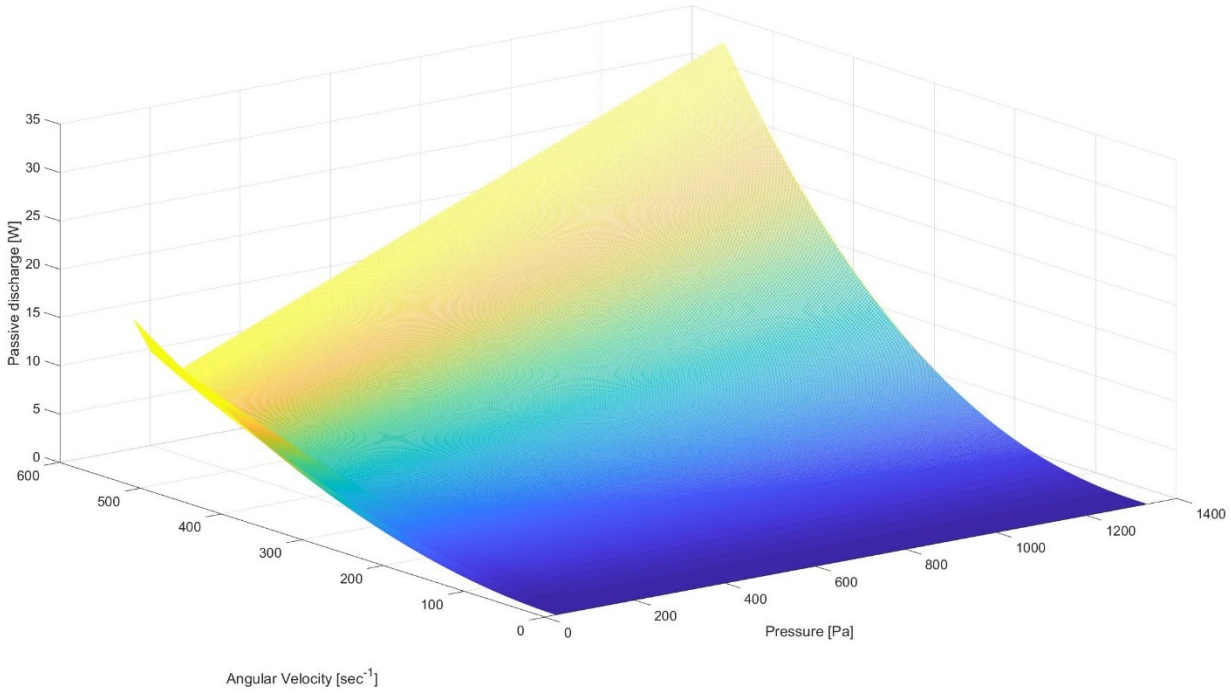

Figure 34: Total rotor passive discharge vs angular velocity and pressure.

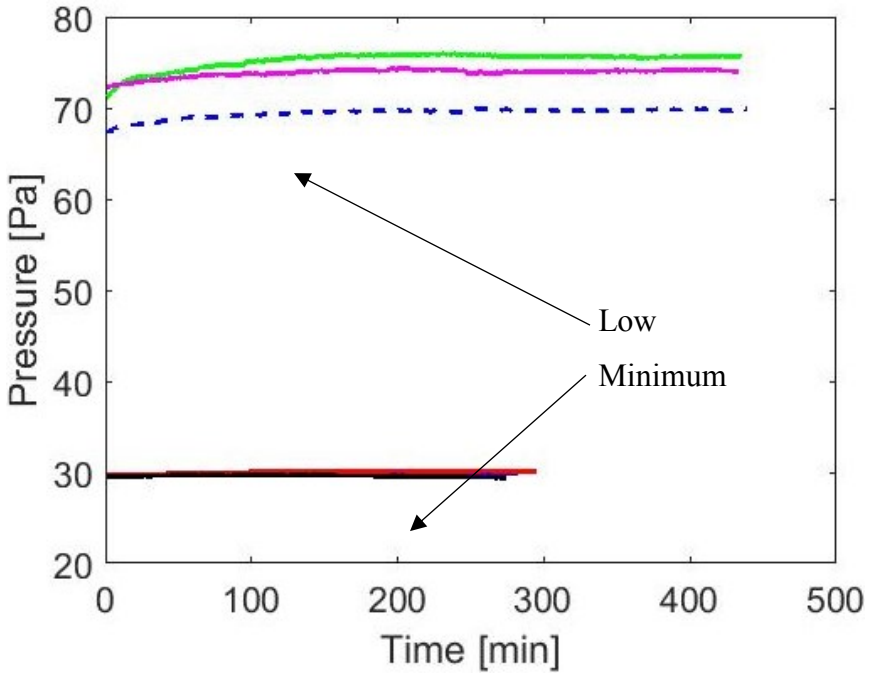

Figure 35: Minimum and low state experimental pressure data.

The only other sensor is the OSS mounted to the top of the housing. This sensor records angular velocity by counting the number of times a pulse of light reflects off the reflective surface of the rotor in a predefined period of time. This system was found to function accurately at atmospheric pressures by manually turning the rotor at low speed and comparing the manual and sensor measurements. While this was tested in atmosphere the only difference during operation is the vacuum condition of the housing which changes the refractive index of the medium which the light passes through. However, this does not affect the OSS because it employs a halogen lamp to ensure there is always sufficient light reaching the sensor. There are no other sensors used in this study, so instrumentation failure is unlikely.

It has been hypothesized the increasing losses with decreasing pressure could be due to less efficient heat convection away from the bearings as pressure decreases. Then the additional heating could increase the rolling friction in the bearing, and increasing passive discharge. Heat convection away from the bearing does become less efficient as pressure decreases. However, regardless of the experimental pressure convection will always be negligible compared to heat conduction from the bearing to the hub and housing. Conduction is pressure independent so the bearing temperature is not expected to change significantly under any of the experimental conditions. Conduction is dependent on the area of the contact region, and the balls have a relatively small contact region with the race. Therefore, the reduction in convection could allow bearing ball heating to become significant enough to reduce the bearing rolling efficiency.

An unknown deformation in the bearing fixture could change the loading conditions, however no change in the external deformations were measurable. Further, the difference in force applied to the housing is negligible. Consider, atmospheric pressure is 101,125 Pa, and the pressure in the housing changes from 27 Pa to 133 Pa, so the difference in pressure is approximately 100 Pa or 0.1% of the total pressure. The surface area of the housing is constant so the 0.1% change in pressure results in the same change in force. This is a small change compared to the total force, so it is not expected to significantly affect the system in this way.

Finally, bearing wear against the shaft generates fine particles which can migrate from the bearing-shaft interface to the ball-race interface increasing passive discharge. This can be a pressure dependent effect and will be discussed in greater detail in chapter 6.

Many FESS operate at lower pressures than the one used in this study, for example the one used by Place in [42]. It is likely this effect is unique to the system in this thesis although few other studies have been conducted in this manner, so direct comparison is not possible.

The minimum passive discharge losses shown in Figure 31, i.e. losses at the intermediate pressure (133 Pa), are taken as pressure independent losses and are assumed to be largely caused by the mechanical bearing rolling friction as well as some amount of air friction. This is approximately 10.5 W at maximum velocity decaying to 2.6 W at 2,500 RPM, and significantly less than 1 W below that. These losses are subtracted from all other losses to find the pressure dependent losses. The α, β and statistical parameters from equation (37) are given in Table 8.

Table 8: Best fit coefficients and statistical parameters for the baseline losses which occur at 133 Pa (intermediate pressure state).

Parameter	Value
α	2.753×10^{-4}
β	1.685
SSE	1.006
Adj-r^2	0.9995
RMES	0.0529

Looking at the baseline losses alone the best fit approximation is given by itself in Figure 31, where the approximation coefficients, α and β, are 2.753×10^{-4} and 1.685 respectively. The exponential coefficient, β, is most interesting as it can indicate which passive discharge source dominates losses under these conditions. Equations (13) and (22) are the theoretical models governing these conditions. The bearing losses in (13) are linearly related to velocity while the air friction losses in (22) are cubically related. The results from the baseline loss approximations are dependent on angular velocity to the power of 1.685 indicating the mechanical bearings do contribute to the losses more than air friction. It is possible to rewrite the empirical best fit approximation in equation (38) to separate the bearing and air friction losses giving,

$$P = \alpha_{\mathrm{mb}}\omega + \alpha_{\mathrm{air}}\omega^3, \tag{38}$$

where the constant coefficient for each source are now separated and the velocity exponents are defined by the models discussed in chapter 4. The results of this fit compared to the intermediate pressure state are shown in Figure *36*. This equation is appropriate because the theoretical models, discussed in chapter 4, are designed to predict losses in an FESS under these conditions, and air and bearing friction are the only sources of passive discharge.

This approximation is reasonably good, but not as accurate as the first, equation (37). The SSE and RMSE are both more than double the previous set. Comparing Figure *36* to Figure 31 this approximation tends to underestimate the experimental data at moderate velocities, from 1,900 to 3,800 RPM (200 – 400 sec^{-1}), but then overestimate above 3,800 RPM (400 sec^{-1}). However, the approximation according to equation (38) is more useful for comparing the experimental results to the theoretical models. The constant coefficients α_{mb} and α_{air} are 0.0074 and $5.536x10^{-8}$ respectively. Consider the air friction coefficient first. This coefficient makes this term negligible at low velocities allowing the bearing friction to dominate. This changes as velocity increases and the angular velocity grows large enough to dominate the equation.

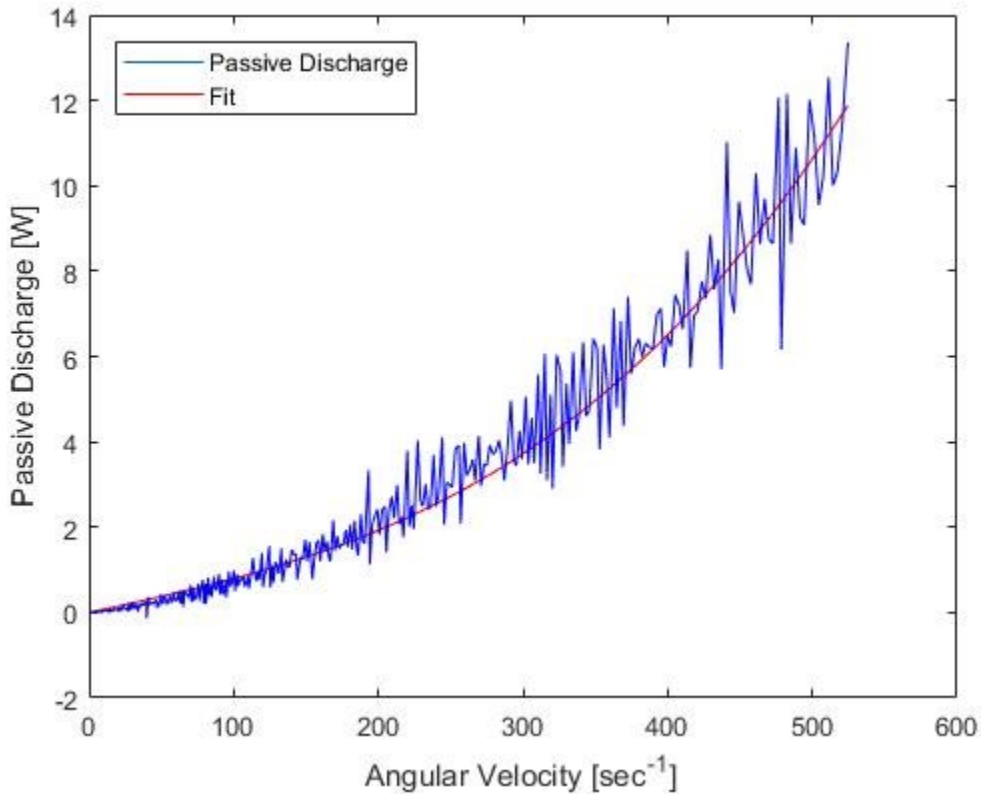

Figure 36*: Best fit approximation of intermediate pressure state passive discharge losses using equation 38.*

Table 9: Physical constants used to calculate theoretical air friction coefficient from equation 22.

	Value	Unit
Molecular weight, M	0.028	$\frac{kg}{mol}$
Temperature, T	293.15	K
Gas Constant. R	8.314	$\frac{kg\ m^2}{s^2 K\ mol}$
Density, ρ	0.0015	$\frac{kg}{m^3}$
Viscosity, μ	1.81×10^{-5}	$\frac{kg}{m\ s}$
Reynolds Number, Re	1.77×10^{3}	-
Reduced Torque Coefficient, c_m	0.09	-

Comparing the air friction term with equation (38) can indicate how well the theoretical model, from equation (15), represents the experimental results. The necessary constants are given in Table 9.

From this the air friction coefficient, C, is 9.125×10^{-8} which compares relatively well with the experimental data in that they are of the same order of magnitude. However, they vary from each other by approximately 64.83% at maximum velocity. Based on this the theoretical model overestimates the air friction passive discharge by 65% at all speeds. This could be caused by an overestimation of the reduced torque coefficient which is found in Figure 25 and is dependent on the Reynolds number. The actual Reynolds number for the FESS falls outside the minimum range given in the figure, so the c_m value had to be estimated based on a linear interpolation from the given graph. Additionally, this value is held constant instead of increasing as the Reynolds number decreased, because of the lack of an appropriate functional form. Holding c_m constant is believed to be appropriate for this model because c_m increases linearly from 0.001 to 0.1 while Re increases logarithmically, meaning large changes in Re relate to small change in c_m. Further, Re is constrained by air density, dependent on pressure, and angular velocity which is kept relatively low, so the Reynolds number does not vary significantly. The

largest changes in Reynolds number occur at minimum velocity, so this will introduce the larger error as velocity approaches zero. These points suggest keeping the reduced torque coefficient constant is appropriate, however the result of this is some overestimation in passive discharge, especially at low velocities. This model could more accurately represent the experimental data if more information was known about the reduced torque coefficient at the appropriate Reynolds numbers.

Considering equation (38) decouples the bearing and air friction losses it is possible to determine the significance of each source at various velocities. At maximum velocity, 5,000 RPM, the bearing friction accounts for 32.8% of losses while air friction accounted for 67.2%. At 2,500 RPM, this reversed to 66.2% for the bearing friction and 33.8% for air friction. The air friction continues to decrease cubically, and becomes negligible as velocity approaches zero. The break down for percent loss due to each source is given in Figure 37. This shows the air friction surpasses the bearings at approximately 3,500 RPM (368.2 sec^{-1}).

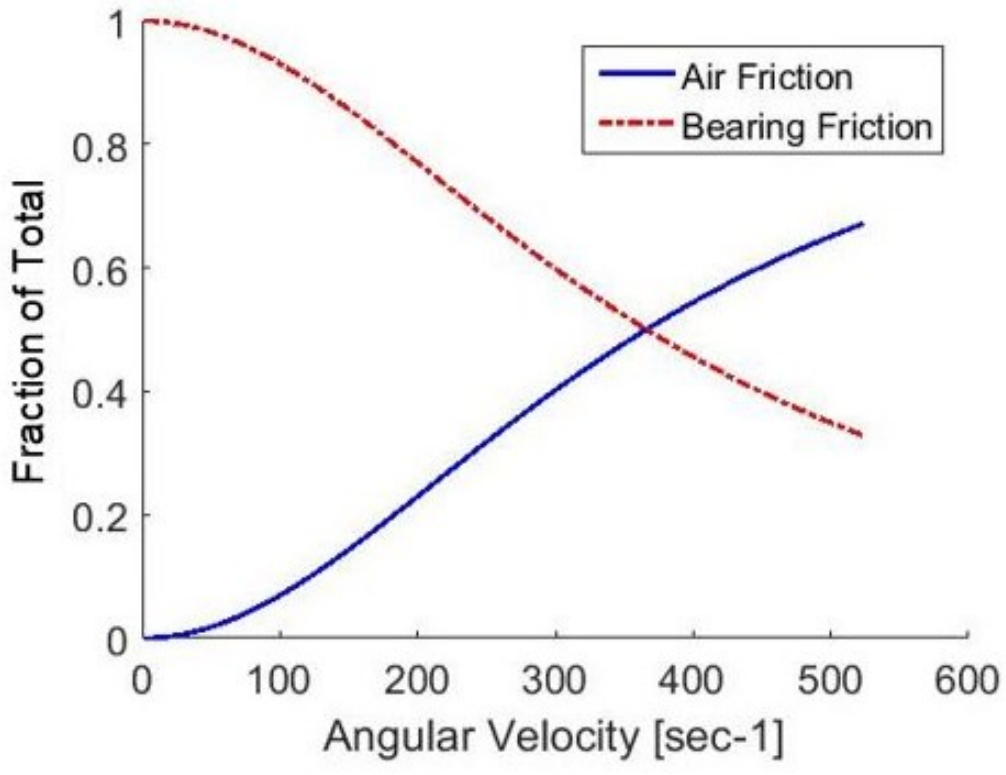

Figure 37: Percent losses due to the bearing and air friction based on the approximation from equation (38) at the baseline (intermediate) pressure state.

While the best fit approximation from equation (38) is useful for decoupling the passive discharge sources and comparing with theoretical models it does not as accurately represent the experimental data as equation (37). Therefore, the empirical approximation from this equation is expected to be more accurate when predicting losses or when integrated into FESS optimization algorithms. However, it is limited to this FESS and would need to be validated or recreated as the system changes.

5.2.2 Air Friction

To quantify the passive discharge due to the change in air pressure at each state the baseline losses are subtracted from the net losses at each pressure state according to equation (36) where these losses can be written as,

$$P_{\text{air}}(\omega) = P_{\text{total}}(\omega) - P_{\text{baseline}}(\omega). \tag{39}$$

The losses for each pressure state are given in Figure 38. The losses at all states are approximately equal while the rotor velocity is below 955 RPM (100 sec^{-1}). There is a small amount of error in this range of approximately ±0.1 W maximum. The low pressure losses are most similar to the baseline with a maximum difference of approximately 1.1 W decaying to less than 0.1 W at 2,500 RPM. In this figure the unusual increase in losses as pressure decreases is again visible between the minimum and low pressure states.

The air friction results, in Figure 38, can be compared to the analytical model in chapter 4.2 to understand how accurately this model represents losses. The physical constants are given in Table 10. Only the density, Reynolds number, and reduced torque coefficient are dependent on air pressure so these must be updated. The reduced torque coefficient is held constant as discussed previously, but varies between pressure states with the other pressure dependent variables.

The analytical model, equation (38), cannot be compared with the baseline losses because these are a combination of air friction and bearing friction which the analytical model does not take bearings into account.

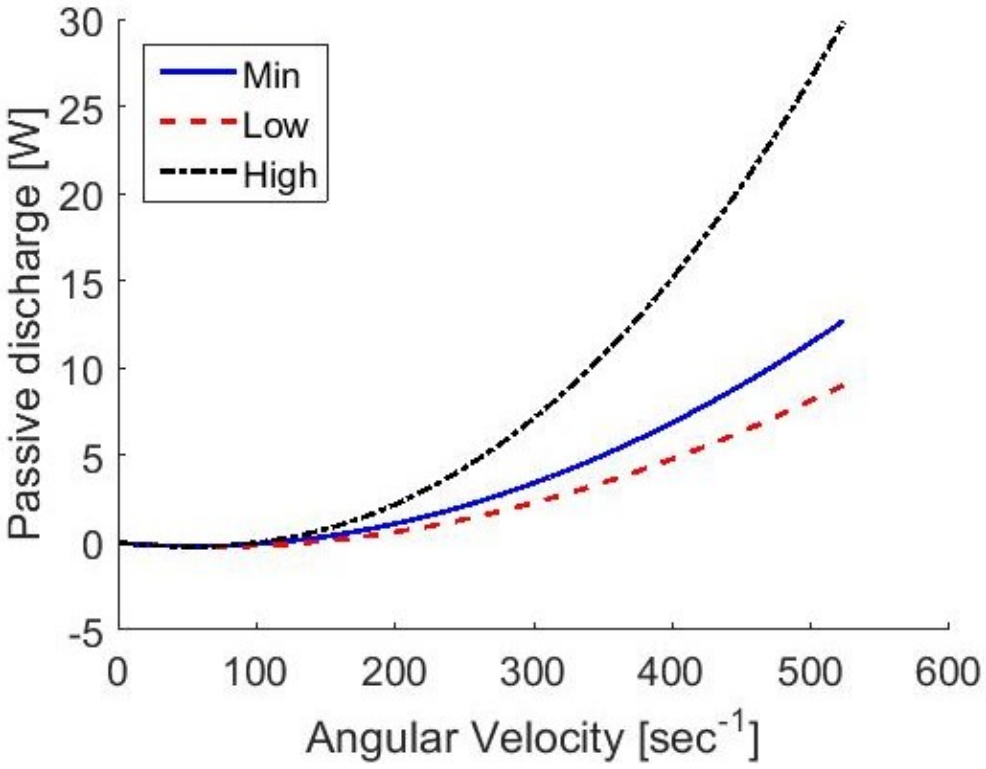

Figure 38: Comparison of air friction losses at minimum, low, and high pressure state with baseline losses removed.

Table 10: Physical constants used to calculate theoretical air friction losses at each pressure state.

Pressure state	Minimum	Low	High	Unit
Molecular weight, M	0.028	0.028	0.028	$\frac{\text{kg}}{\text{mol}}$
Temperature, T	293.15	293.15	293.15	K
Gas Constant, R	8.314	8.314	8.314	$\frac{\text{kg m}^2}{\text{s}^2\text{K mol}}$
Density, ρ	$3.06\text{x}10^{-4}$	$7.66\text{x}10^{-4}$	0.015	$\frac{\text{kg}}{\text{m}^3}$
Viscosity, μ	$1.81\text{x}10^{-5}$	$1.81\text{x}10^{-5}$	$1.81\text{x}10^{-5}$	$\frac{\text{kg}}{\text{m s}}$
Reynolds Number, Re	354.5	886.2	$1.77\text{x}10^{4}$	-
Reduced Torque Coefficient, c_m	0.1	0.1	0.013	-

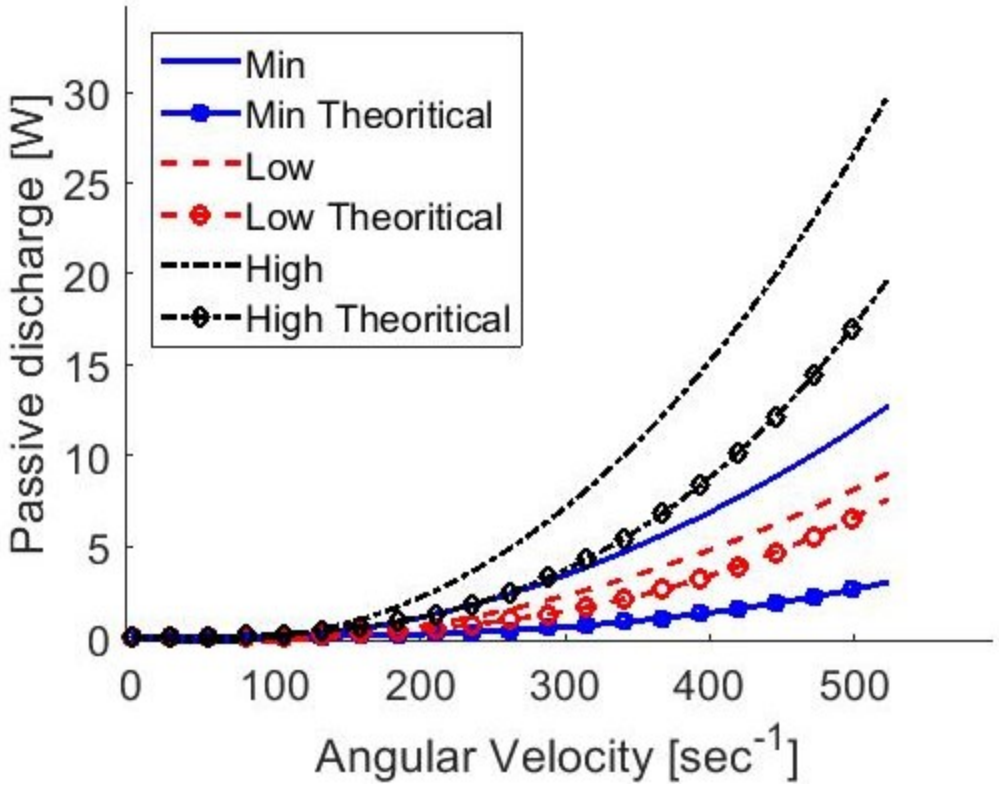

Figure 39: Experimental passive discharge plotted against the analytical model.

The experimental results in Figure 39 are generated by subtracting the bearing losses calculated with equation (38), and the expected analytical results are plotted alongside these. The black curve represents the high pressure state analytical results, and corresponds most closely with the theoretical model. The high pressure state passive discharge and the theoretical model follow the same trends indicating only pressure dependent losses are represented in the figure. This is expected given the pressure independent losses were accounted for and removed with the bearing friction. These data sets contain only losses due to the air friction. The theoretical losses are plotted alongside the experimental data, shown in the figure with markers on corresponding lines, for comparison. The error between the theoretical and experimental high pressure losses are approximately 34%. Some error is expected based on the previous baseline loss discussion, further, the error with the high pressure experiment is significantly less than that seen at the baseline pressure. Note this is in contrast to the baseline losses which were not as accurately represented by the approximation in equation (38) based on the constant coefficients. The exponential coefficient, β, for the high pressure state is 2.689, given in Table 12, which is close to the theoretical value, therefore, given this and the correlation at the baseline pressure, it is

reasonable to assume the theoretical model is a reasonable approximation of how the FESS is expected to behave.

The high pressure state experimental results correlate well with the theoretical air friction model so applying equation (38) to these results can decouple the bearing and air friction losses. This is accomplished by fitting the total discharge data, which includes the intermediate losses which were subtracted in the earlier analysis, to this equation. The results of this fitting are given in Figure 40.

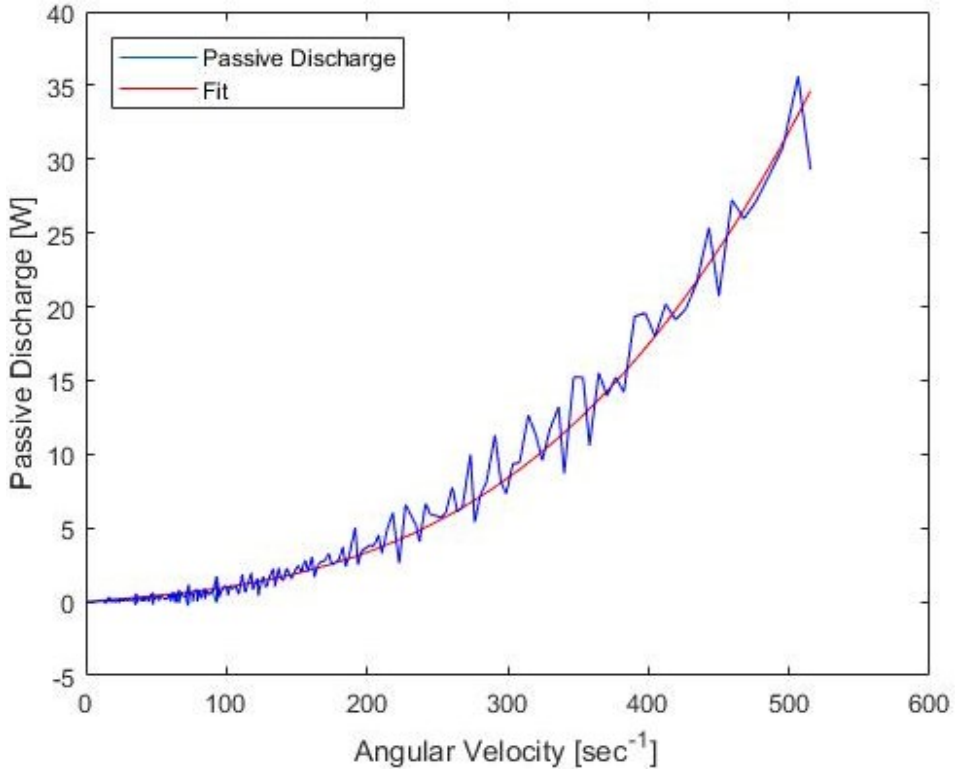

Figure 40: Total high pressure state passive discharge losses with equation (38) best fit approximation.
The constant coefficients for this approximation are 0.0078 and 2.238x10^{-7} for α_{mb} and α_{air} respectively, and the statistical parameters are comparable to those discussed in

Table 7 above. The Adj-r^2 is the same at 0.9997, the RMSE is larger by 0.1 to a total of 0.118, and the SSE is larger at 3.464. The values are given in Table 11.

Table 11: Statistical goodness of fit parameters for the total passive discharge losses at the high pressure state fitted to equation (38).

Parameter	Value
α_{mb}	0.0078
α_{air}	2.238×10^{-7}
SSE	3.464
Adj-r^2	0.9997
RMES	0.118

First, the mechanical bearing coefficient correlates well with the same coefficient at the intermediate state, with a difference of 0.0004, indicating the mechanical bearings do have relatively constant losses at across this pressure range. This is expected because changes in air pressure should not change the bearing surface conditions, i.e. friction coefficient, or loading. Secondly, the air friction coefficient is approximately an order of magnitude greater than at the intermediate pressure state. Again, it is expected for this coefficient to be larger than the intermediate pressure state. Both the pressure and the coefficient are increased by an order of magnitude from one state to the other, so, it is possible the relationship between pressure and the α_{air} coefficient is linear. Conducting this same analysis and pressures in between the intermediate and high pressure state can better define this coefficient. Currently, the air friction coefficient for intermediate pressures, i.e. pressures between the intermediate and high states, can be defined as,

$$\alpha_{\text{air}} = 1.404\text{x}10^{-10}P_r + 3.664x10^{-8}. \quad (40)$$

The low and minimum pressure states will be discussed below, however at this point it is worth noting that equation (38) is not appropriate for these data sets because they do not correlate with the theoretical models discussed in chapter 4. That is, applying this equation assumes these two sources of passive discharge losses are the only source, however there is sufficient evidence to suggest these models are not appropriate for representing these data. Therefore, fitting to this equation is inappropriate because it requires making this unverified assumption.

Comparing the minimum and low pressure states to the model can indicate how much air friction is affecting the system. The minimum and low pressure state air friction losses are given in Figure 41, and the α and β coefficients are given in Table 12.

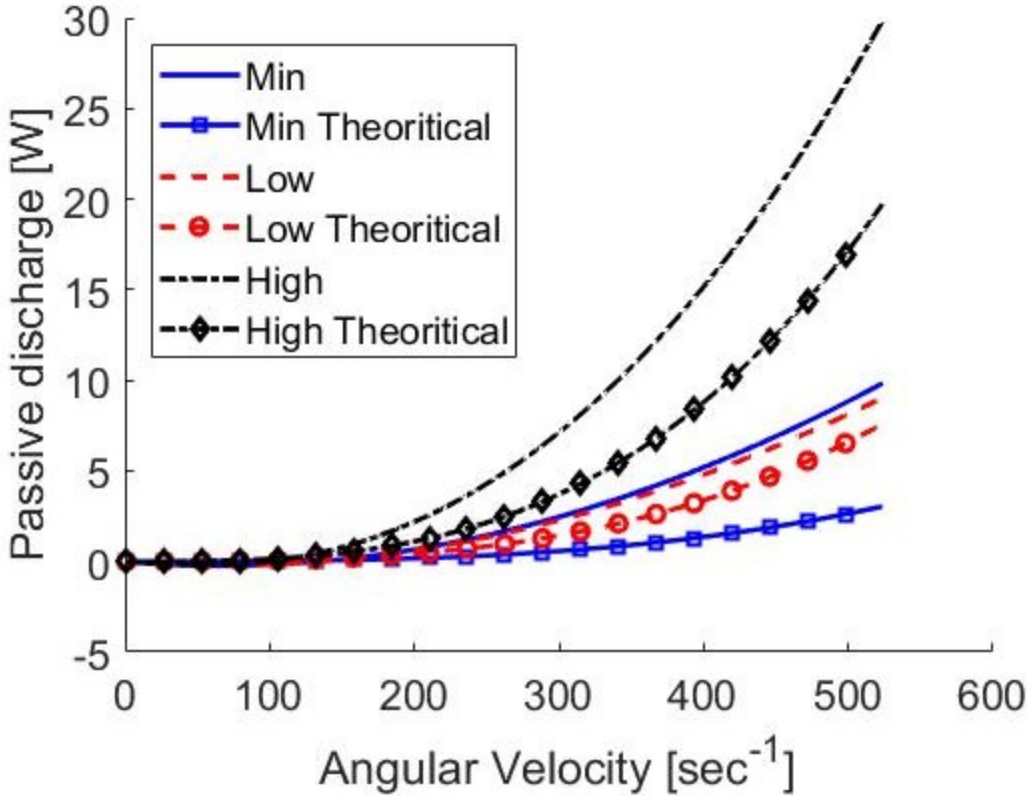

Figure 41: Comparison of minimum and low pressure experimental data with analytical air friction model.

The theoretical model shows passive discharge decreases as pressure decreases, and the experimental results show discharge increasing with pressure. Comparing these pressure states with the theoretical model it appears the model does not represent the experimental results, likely because air friction is not a significant source of passive discharge losses. The temperature remains approximately constant during all experiments, so the excessive losses are not caused by heating. The only other source of passive discharge is to the bearings; however, these losses should have been removed with the passive independent losses. Therefore, the experimental results show the bearing friction has likely increased significantly for some pressure dependent reason. This further supports the hypothesis, discussed earlier, that a deformation or change in deformation caused greater loading in the bearings. While the change in loading on the housing is relatively small this could cause a small change in the housing part of the bearing fixture, especially the top plate which is more susceptible to deformation. Changes in the bearing fixtures which alters radial or axial loading potentially increasing bearing friction. This hypothesis could be verified by measuring bearing load during operation under the operations used in this study.

To accomplish this the housing top and bottom plate, and the corresponding bearing fixtures would need to be redesigned to accommodate load sensors.

Table 12: Best fit approximation coefficients for pressure independent losses from minimum, low, and high pressure states.

Coefficient	Minimum	Low	High
α	9.018×10^{-7}	3.888×10^{-9}	1.142×10^{-6}
β	2.513	3.237	2.689

The low and minimum pressure losses should be taken with an understanding that they do not follow the expected loss mechanics, so there must be another force acting on the system that is not yet understood. However, the method of isolating and analyzing air friction passive discharge is able to quantify losses at a variety of air pressures and velocities. This method can also be used to identify which sources of passive discharge dominated the losses at any time or velocity during operation using the β coefficient. Finally, these models have been shown to be able to accurately predict rotor kinetic energy within the velocity range.

5.2.3 Electrical Machine Losses

The electrical machine, when coupled to the system, has no power flowing through the windings so it experiences zero load losses. It does, however, experience no-load losses which are divided among eddy current, hysteresis, air friction, and bearing friction. Note the air and bearing friction experienced by the electrical machine are separate from the rotor. The electrical machine has its own set of mechanical bearings and operates in atmosphere. The electrical losses are no-load EMF in the iron core, permanent magnets, and stator, as discussed in chapter 4. The air friction is a relatively complicated, but well understood turbulent flow process with air flowing through the fins and around the copper winding in the electrical machine. This flow is restrained by the machine fixture, seen in Figure 3, on the top plate, which holds the electrical machine vertically above the rotor. The bearing friction, due to the ball bearings on which the machine rotor rotates around the stator, can be modeled as discussed in chapter 4.

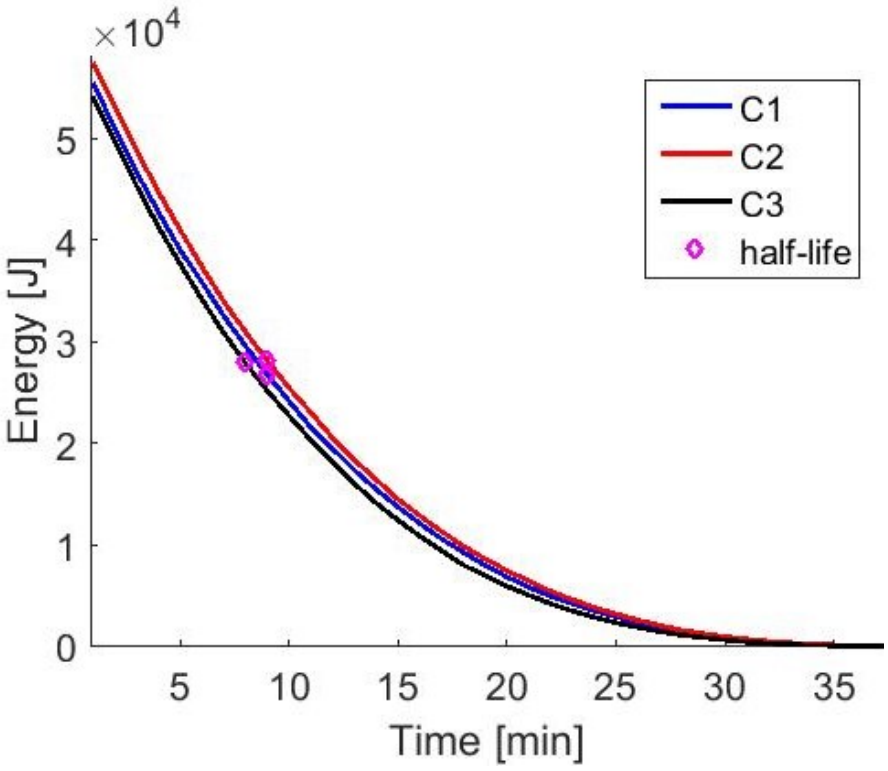

Figure 42: Rotor kinetic energy vs time for the coupled electrical machine condition at 133 Pa. The half-life is shown at a point on each curve.

The electrical machine decreases the half-life and total storage time by more than 90% when compared to the baseline, seen in Figure 26. All three experiments fully discharge within 5 minutes of each other.

The baseline losses at 133 Pa, can be removed from these data, to determine the losses due specifically to the electrical machine yielding Figure 43. This figure shows the passive discharge losses are approximately 72 W at maximum velocity. These losses are approximately linear throughout the experiment with the β coefficient equal to 1.368, given in Table 13. Considering the electrical losses in equations (24) and (25) the hysteresis losses are linearly related to frequency while the eddy current losses are quadratically related to frequency. As previously discussed the bearing friction is linearly dependent on velocity. The air friction model discussed in chapter 4 is not applicable under these conditions because it was designed for flywheel rotors operating under vacuum, however air friction should account the remaining losses. Given the approximately linear passive discharge behavior, based on the β coefficient, the EMF and bearing losses combined appear to have a larger effect on losses than air friction. Based on the theoretical models, hysteresis and bearing friction are linear with velocity while

eddy current losses are quadratic with velocity this is a reasonable conclusion. This is supported by the results presented in [59] by Tong, where EMF effects can account for up to 50% of losses.

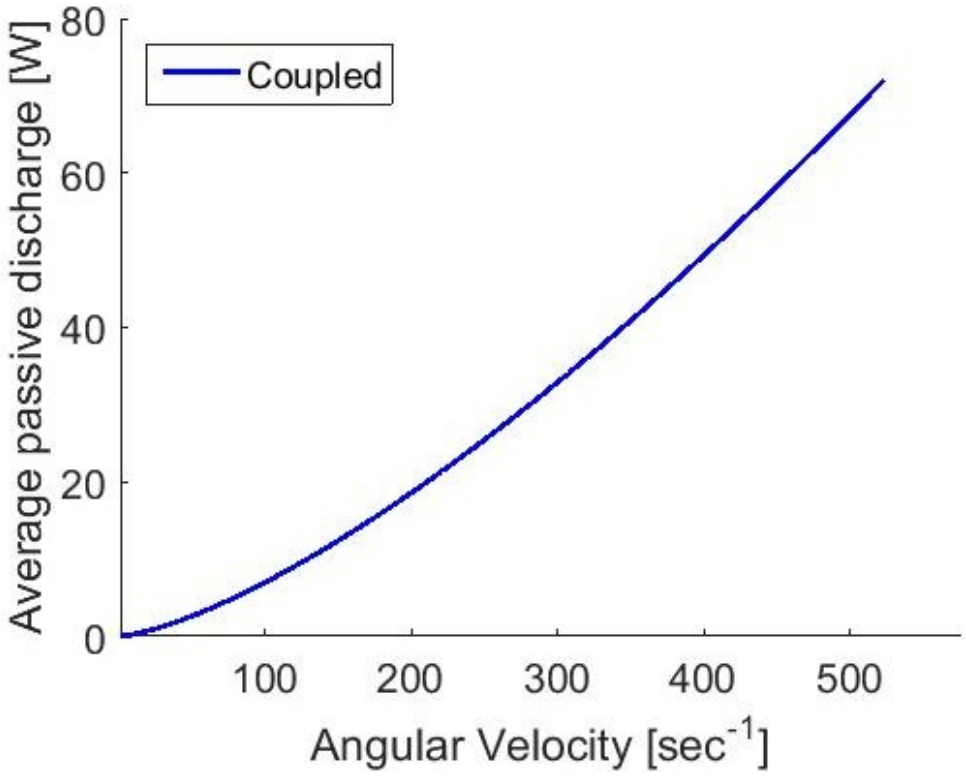

Figure 43: Electrical machine specific losses [W] vs rotor angular velocity with the baseline removed.

The statistical goodness of fit parameters used to make this model are given in Table 13. These values indicate the model can accurately represent the experimental data with small standard deviation and high fit quality.

Table 13: Best fit approximation coefficients and statistical goodness of fit parameters for coupled electrical machine condition.

	Value
α	0.0118
β	1.368
SSE	1.104
Adj-r^2	0.999
RMES	0.175

The baseline losses were separated into bearing and air friction losses with equation (38) to determine the fraction of total losses due to each source. This was discussed in the previous section and shown in Figure 37. These results can be combined with the coupled machine results discussed here to determine fraction of total losses contributed by each source, Figure 44. As velocity approach zero the electrical machine contributes less to passive discharge meaning the bearing losses are the only significant factor. However, this rapidly grows to completely dominate the losses at approximately 1,700 RPM (180 sec^{-1}). At this point air friction become more significant because it is cubically related to velocity, so the percentage of total losses due to the electrical machine decreases. The electrical machine losses are dependent on angular velocity raised to 1.3 whereas the air friction is cubically dependent. Therefore, the air friction losses are expected to grow faster than the electrical machine losses.

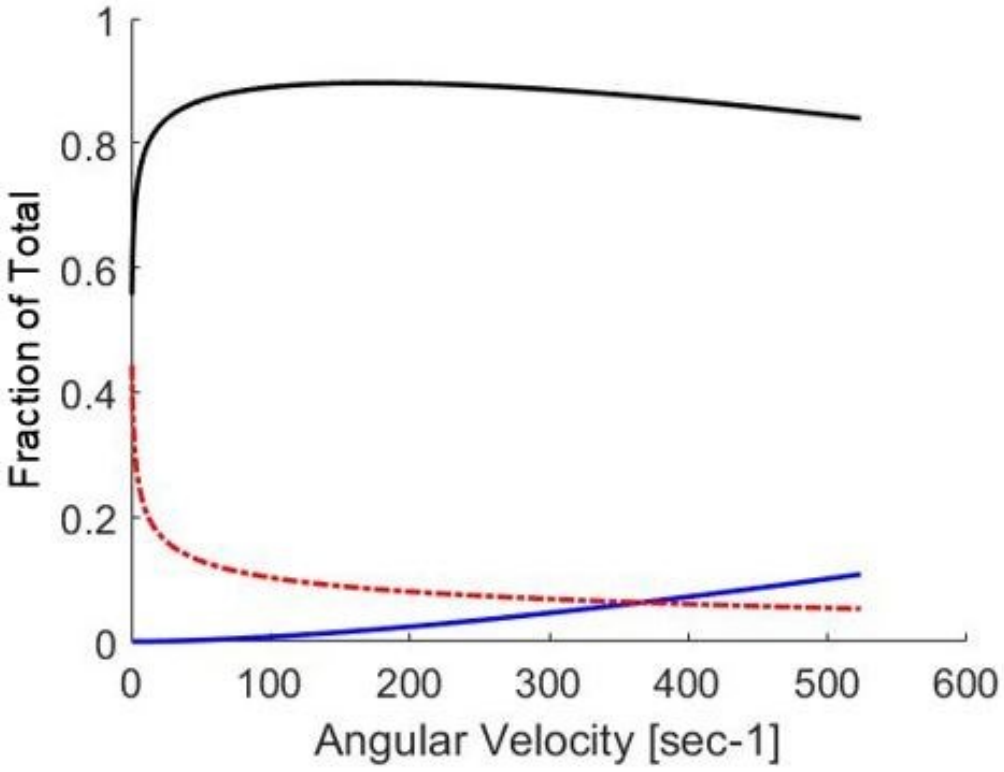

Figure 44: Percentage of total losses attributed to the electrical machine.

5.3 Summary

Based on the previous results the following models are proposed for bearings, air and electrical machine losses for the current FESS are,

$$P_{baseline} = 0.2753x10^{-3}\omega^{1.685}, \quad (41)$$

for the baseline,

$$P_{EMF} = 0.0118\omega^{1.368}, \quad (42)$$

for the electrical machine losses, and

$$P_{air} = \alpha_{\text{air}}\omega^{3} \quad (43)$$

for the air friction. For air pressures at and above the baseline the air friction coefficient can be found with equation (40). The bearing losses can be calculated with,

$$P_{\text{bearing}} = 0.0074\omega. \quad (44)$$

The coefficient varies by $4x10^{-4}$ from the baseline to the high pressure state, however this difference is relatively small compared to the sources of passive discharge.

The losses below the baseline can be determined using the values in Table 12, however these models are not recommended due to the highly unexpected behavior below the baseline. It is recommended that the cause of this behavior is determined before attempting to model the system's passive discharge losses at the minimum and low pressure states.

6 Bearing Wear Analysis

6.1 Observations

The inspection of the FESS after operation revealed the presence of particulate contaminations in the mechanical bearings, and hence, a thorough maintenance schedule was developed in order to ensure consistent operating conditions. The bearings were cleaned with compressed air and checked for damage every four to six experiments, corresponding to 24 to 36 operating hours. To assemble and disassemble the FESS for maintenance the rotor and lower bearing assembly are placed into the housing separately, and from different sides, i.e. the rotor was placed in the housing from the top and the bearings were pushed onto the rotor shaft from the bottom, so the bearing must be able to slide onto and off the shaft portion of the hub. It was observed that the lower bearing assembly suffered significantly more deterioration than the upper bearing, which was believed to be the result of increased axial loading. Consequently, the subsequent analysis focusses on the lower bearing assembly.

During maintenance a significant amount of fine metallic powder was discovered in the bearing and the bearing-shaft interface. Initially, it was hypothesized that this debris was created by rolling friction between the bearing balls. However, at some point the bearing could not be removed from the shaft, and the ensuing investigation revealed that significant damage to the shaft had occurred. This led to a new hypothesis, i.e., fretting at the bearing-shaft interface was the actual cause for the contamination of the bearing with particulate debris.

The description of fretting given by ASM International [20] states that fretting is commonly seen in bearing-shaft systems subject to high vibrational loads. This is characterized by small-scale sliding between the bearing and shaft resulting in micron to nano-scale particles worn off the surface of the materials. Additionally, material transfer between the surfaces is common. Based on the U.S. National Advisory Committee for Aeronautics (NACA) [61], fretting is primarily dependent on bearing load, vibration, hardness ratio, and environment. Specifically, high vibrational loads, as described by [61], large hardness ratios, and friction coefficient, both described by Neyman et al. [62], significantly increase the fretting rate. Environmental concerns are temperature, relative humidity, air pressure, and corrosive elements such as salt. The only factor of concern for the FESS is the air pressure as the system operates under vacuum at a constant temperature.

Neyman et al. [62] investigated the fretting wear rate by defining a stationary and moving surface, and then measuring the volume of material removed from each surface. The results indicated that a high hardness ratio from the moving to the stationary surface increased the wear rate. They also found low friction coefficients and lubrication to decrease wear rate. However, wet lubricants cannot be used in FESS bearings, and dry lubricants tend to have short lifetimes in conditions present during FESS operation.

Motivated by assembly requirements, the fit between the bearing and shaft/hub in the FESS was designed to be a close location clearance fit, approximately H7/h6 or LC2 according to ANSI B4.1 standard. The shaft diameter with tolerances was to range from a maximum of 15.000 mm to a minimum of 14.991 mm. Consequently, the bearing inner race and the shaft are not rigidly fixed to one another which allowed the ID of the bearing to slide against the OD of the shaft. Both particle generation and material transfer were thus observed from the FESS bearing and shaft indicating fretting is occurring during operation. Moreover, circumferential striations are visible on the shaft caused by the relative motion where particles worn from each surface remained at the interface increasing the wear rate. It is possible that the striations were generated during fretting. However, as the fit between the components became looser the system would likely transition to an abrasive wear pattern characterized by larger-scale sliding, which could also produce striations. The wear occurring at the bearing-shaft interface would typically generate aluminum oxide particles, which then remain at the bearing-shaft interface or are transported into the bearing and the ball-race interface by vibrations and/or air flow, Figure 45.

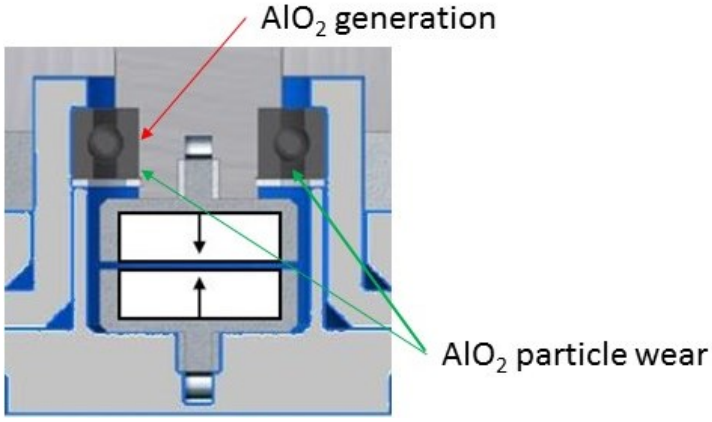

Figure 45: Lower bearing assembly cross section identifying where particles are generated and where they migrate to during operation.

The aluminum shaft has a Vickers hardness of 107 MPa [63], and the silicon nitride bearing's hardness is approximately 16 GPa [64]. It is worth noting that the aluminum hardness was measured in Brinell hardness and converted to Vickers by ASM [20]. For this system, with the bearing moving on the shaft, the hardness ratio of the bearing to the shaft is large, which thus increases the wear rate of the shaft.

6.2 Microscopic Analysis

To inspect the bearing and hub shaft surfaces, and to better understand the wear processes in the FESS, the individual components were examined under a microscope, as seen in Figure 46 and Figure 47. The primary goal was to identify the size of features, such as the striations on the hub shaft, and scale and type of particles generated during wear. ASM [20] and NACA [61] state that the fine particles generated during the described wear process typically oxidize very quickly in atmosphere and act like an abrasive further increasing the wear at the interface. This is also noted by referring to iron oxide particles in the interface of steel bearing-shaft systems. However, due to the vacuum condition the FESS operates under, particle oxidization does not occur or progresses at a much lower rate. Aluminum particles were thus generated during the wear process, which then deposited non-uniformly on the ID of the inner race, Figure 46a and Figure 46b, show the erosion area of the shaft and deposits on the inner diameter of the inner race, respectively. The vertical striations seen in Figure 46a are 100 μm to 300 μm wide and 3 mm to 5 mm long. It should be noted that deposited particles are likely a combination of pure aluminum (Al), aluminum oxide (Al_2O_3), and silicon nitride (Si_3N_4). The axial striation seen in the center of Figure 46a was created when the hub and bearing were pressed apart in a large press as and will be described in detail later.

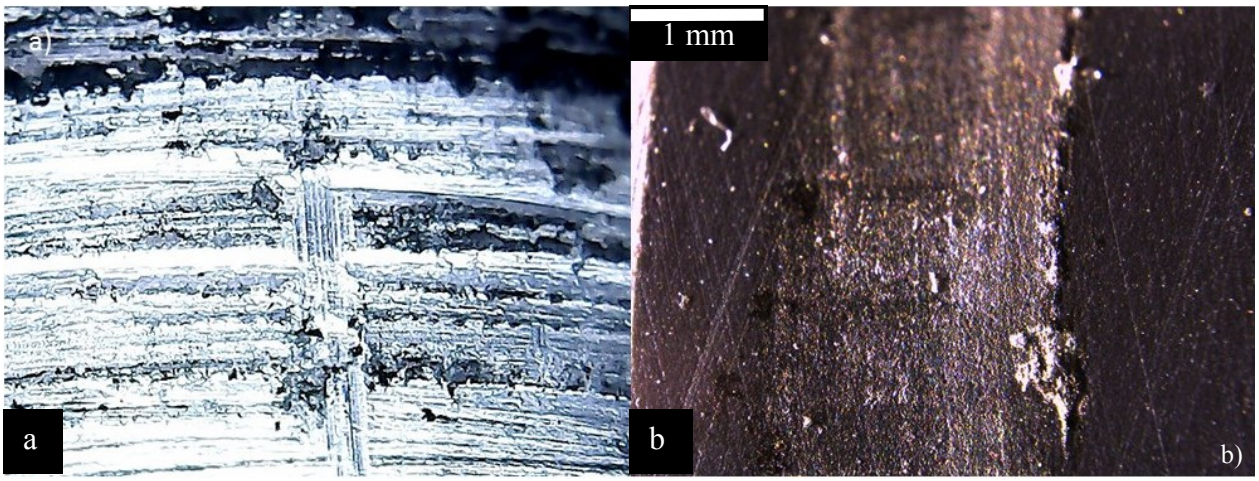

Figure 46: a) Hub erosion due to fretting and adhesion between the hub and bearing race. Features in this figure are in the mm scale. b) Aluminum material transfer to the inner bearing surface. The scale shown in the top left corner reads 1 mm.

Fine particles from the wear process were also transported into the bearing and to the ball-race interface, increasing friction and reducing bearing life. Images of a bearing ball and the inner race are shown in Figure 45a and Figure 45b, respectively, where particles are visible on the surfaces. Particles were embedded into the surface of the balls indicating they are aluminum oxide particles capable of maintaining their shape while damaging the surface of the hard silicon nitride bearing. If these particles were pure aluminum, then a thin, more evenly dispersed layer would be expected on the surface, such as seen on the inner diameter of the inner race, Figure 46b. The particles seen on the balls and races, Figure 47, are fine arbitrarily shaped aluminum oxide particles in the bearing surfaces. All the damage to the bearings here is from particles embedded in or forced below the surface, but there is no evidence of soft aluminum particles being deformed in the ball-race interface creating a thin metallic layer on the surface. This indicates that most of the aluminum particles remained at the bearing-hub interface while the oxide particles traveled throughout the bearing assembly more freely.

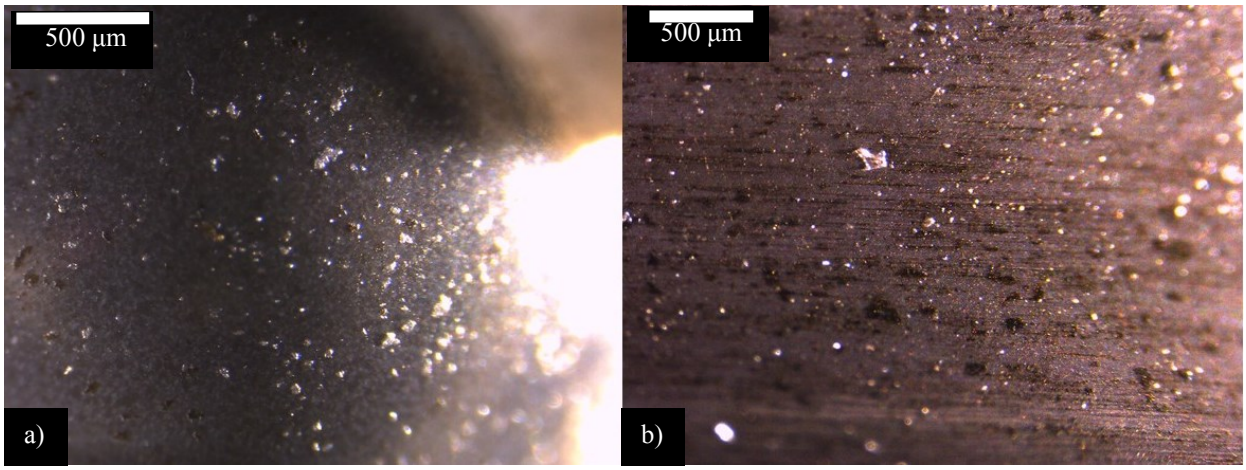

Figure 47: a) Bearing ball with particles in the surface. Particles are shown in light (shiny) and shadow (dark). The scale in the top left corner shows 500 µm. b) bearing race with particles in the groobe where the balls rotate. The scale reads 500 µm.

6.3 Discussion and Recommendations

It has been shown that wear is generating small aluminum and aluminum oxide particles from the hub. The pure aluminum particles cannot oxidize because of the vacuum environment, allowing them to deform and adhere to the bearing inner race. Adhesion and sintering were proposed as explanations for this phenomenon. Sintering is a high temperature process and no evidence of heating was discovered on any components, so it was ruled out as an explanation. Adhesion, commonly referred to as cold welding, sticking, or stiction, is a relatively well understood effect which can occur between any two clean surfaces made from the same material. The striations and material transfer are clearly visible in the figure.

In all likelihood, there are two particle adhesion processes occurring in the FESS bearing system. First, aluminum particles mechanically adhere to the inner diameter of the inner race of the bearing. Then, the deposited aluminum is transferred back to the hub where it adheres to its clean aluminum surface. Given the vacuum conditions the latter may even be a pure aluminum surface. Resulting aluminum adhesions are uneven to the bearing surface, creating elevated features on the hub surface that may be of significant size. Such larger aluminum deposits likely gouged the hub surface during bearing extraction since several gouges were visible around the outer diameter of the hub shaft (see striation in the center of Figure 45a). These features were not caused by fretting but rather by galling while separating the components. In fact, similar conditions are commonly observed between moving components of spacecraft caused by impact

or fretting, as described by the European Space Agency (ESA) [65]. The ESA document notes that this form of adhesion is less common in terrestrial systems compared to orbital ones due to the presence of oxygen in the atmosphere. During fretting the surfaces are pressed together, separated, and then pressed again. In atmospheric conditions the surfaces re-oxidize during the separation phase thus minimizing the chance for adhesion, which is hampered in a vacuum environment.

As mentioned above, once the bearing assembly had seized together it could only be separated by use of a hydraulic press, requiring a force of approximately 1,335 N, see Figure 48. After extraction the outer diameter of the shaft was significantly reduced due to the wear process. After disassembly, the shaft diameter was reduced to approximately 14.9606 mm, more than 0.03 mm. This amount of wear occurred in approximately 80 – 100 hours of operation. Since this wear phenomenon is difficult to observe during FESS operation, it is impossible to determine exactly the amount of time in which damage accumulated. Further, with the shaft this far out of tolerance the fit between the shaft and bearing changed from a locating fit to a clearance fit, so the wear process would likely have transitioned into larger scale sliding wear.

Figure 48: The rotor and bottom plate upside down in the press before the lower bearing is separated from the shaft.

It is clear the design of the bearing/shaft assembly with a locating fit exacerbated the fretting issue to begin with. However, as stated in the ASM Handbook [20], fretting cannot be eliminated entirely. Regardless of how well the bearings are fixed to the shaft, wear from the vibrational loading can still occur, especially in the case where a soft metal shaft is paired with a hard ceramic component. Further, as seen in this study, significant damage can occur even in a relatively short time and at relatively low FESS operating speeds. Damaging effects are cumulative and the wear rate increases as more particles are generated. It is therefore critical to understand the cause and effect of this wear phenomenon. Even FESS designs that use mechanical bearings only as a backup system may be susceptible over the course of their lifetime. For this reason, it is imperative to consider mechanical wear when designing future FESS intended for long-term use, especially when regular maintenance and inspections are costly and inconvenient as in residential energy storage systems.

The above investigation revealed significant shortcomings with the current FESS design. Ideally, the entire hub should be replaced and redesigned. However, this solution was not an option in this study. It is not possible to remove the hub from the composite rotor rims without potentially critically damaging the rotor. Moreover, a new hub and rotor design would be subject to fretting unless an improved design solution can be found. In an attempt to mitigate the wear problem for this study a spacer was added next to the magnetic axial thrust bearing, creating a clamping force on the bearing inner race between the shoulder on the hub shaft and the axial thrust magnet bearing. This solution was already discussed in detail in Chapter 3 (see, Figure 14). The hub shaft was repaired by polishing the surface to remove striations and gouges. In addition, the bearing inner race and hub shaft were provided with a marking that allows for a visual assessment whether the spacer solution properly affixes the bearing and prevents large scale sliding. After implementing these remedies, no further issues were encountered relating to this wear failure mode, and hence, this configuration was used for all experiments presented above for consistence.

For future FESS designs, the following recommendations can be given. In general, fretting can be alleviated by creating a very tight fit between the bearing inner race and the shaft, such as a thermal shrink fit. Additionally, creating an axial clamping force on the inner race with a threaded component (e.g. nut), as was ultimately done in this study, can mitigate this damage

process. However, fretting damage may not entirely preventable, given the long projected operating times of a FESS. Therefore, a future FESS design should avoid large hardness ratios between the components of the bearing assembly as this will minimize fretting effects reducing the wear rate. This however is difficult to achieve with ceramic mechanical bearings, as used here, because they necessarily have much greater hardness than a metallic hub. Nevertheless, metals harder than aluminum should be considered allowing hardness ratios closer to unity. Finally, designing a FESS such that maintenance can be performed with a minimum amount of disassembly while minimizing bearing and shaft deterioration, will promote a greater lifetime of the system.

7 Conclusion and Future work

Flywheel energy storage systems are commonly implemented in small and large scale energy grids, mass transportation, and regenerative braking systems for frequency regulation, energy storage, and power spike reduction. These systems have been, and are continuing to be, improved by the adoption of composite materials allowing them to reach higher energy capacities and energy density. However, to this point, FESS passive discharge losses have not been well understood as longer term energy storage has not been a focus in the field. As FESS applications expand into low cost energy storage for renewable energy grids and regenerative braking systems for mass transport vehicles, passive discharge losses become a larger concern.

In this study, a small scale FESS designed for an application in the Edmonton Light Rail Transit System, using a 0.2 m radius hybrid (carbon/aramid fiber) polymer composite rotor capable of storing 40 to 45 Wh at maximum velocity, was tested to characterize passive discharge losses. A set of experiments was designed to isolate the bearing, air friction and motor losses at 5,000 rpm and below.

During this study, passive discharge losses were characterized by calculating energy lost per unit time from experimental velocity measurements. This was used to find the passive discharge per unit velocity, and a best fit approximation was determined and shown to accurately represent the experimental data. At the baseline pressure of 133 Pa, the passive discharge model was verified against experimental data for velocities up to 5,000 RPM. This method isolated each source of passive discharge to be quantified, and compared against analytical models.

The electrical machine no-load losses were found to be the largest contributor to passive discharge at approximately 50 W and reducing storage time by more than 90% compared to the baseline pressure with the electrical machine uncoupled. Next to the electrical machine no-load losses, the baseline losses at 133 Pa, constituting the bearings and minimum air friction, contributed approximately 8.5 W. Notably, the passive discharge rate was observed to increase as vacuum pressure was decreased below 133 Pa, which is counterintuitive based on the presented theoretical model for air friction. Passive discharge losses increased from the baseline by approximately 1 W at 66 Pa, then again by 2 W at 27 Pa.

Based on the results from this study, recommendations for future, cost-effective FESS designs were derived. Decoupling the electrical machine from the system when not in use has the most significant impact on passive discharge, followed by minimizing bearing losses, and finally

minimizing air friction losses. Mechanical ball bearings cause significant passive discharge losses, so replacing these with a different yet appropriate bearing type is recommended. This is especially important in residential and grid level storage that requires long periods of storage time, perhaps in the order of a day. Even for short term storage applications, such as in the transportation sector, mitigating passive discharge losses is important since associated FESS designs typically require high power output which is directly related to maximizing velocity.

During testing the lower bearing assembly of the FESS failed due to fretting at the bearing-shaft interface. This event caused to significant damage to the bearing and shaft. Given that the rotational velocity during the tests was comparatively low, and the scheduled maintenance interval was also short, it was expected to encounter a wear problem with significant effects on the system. The damage was caused by vibrational loading in the rotating equipment forcing small scale slipping of the inner race of the bearing against the hub shaft. However, it was possible to alleviate the fretting issue by creating a clamping force on the inner race of the bearing between a shoulder on the shaft and the back of the thrust magnet bearing. Ultimately, redesigning the bearing assembly to avoid the observed failure modes should be pursued. Rigidly fixing the bearing to the shaft with an interference fit and selecting a more apt shaft material would help to mitigate sliding and minimize fretting. Additionally, it is recommended to make provisions for ease of maintenance and a replaceable hub shaft.

Future research on passive discharge should address the observation of increasing passive discharge as vacuum pressure decreased below 133 Pa, which could not be explained by any of the discussed theoretical models. Several hypotheses were presented. While all of them are plausible, they insufficiently explain the phenomenon which therefore deserves future study to understand the cause of this behavior, and develop methods to mitigate this effect.

The models developed in this study were only shown to accurately represent the FESS passive discharge losses up to 5,000 RPM, so expanding the experiments to higher velocities is useful for understanding high velocity passive discharge and predicting losses in future FESS. Validating these models will allow them to be integrated into optimization algorithms to effectively develop more efficient FESS. Given the large design space for a FESS – from various types of bearings, electrical machines, and rotor shapes – it is suggested to develop comprehensive (multiphysics) optimization routines that can accurately predict losses arising from different design features. Such computational tools would significantly reduce FESS

development time, and make tailoring a FESS to a specific application more ideal than at present.

The presented method of characterizing passive discharge can be expanded to include variations of components studied here, such as multiple types of bearings and electrical machines. Also, different FESS configurations can be investigated, such as externally mounted electrical machines – used in this study – compared to integrated electrical machines. Including such information in optimization algorithms would further improve their capabilities.

In closing, flywheel energy storage systems are rapidly developing due the introduction of new technologies in the last three decades (e.g. composite rotors, high-performance bearings and electrical machine technology). While a great deal of advancement has occurred during this time period, much effort has been expended on finding the potential of flywheel systems rather than developing a deeper understanding of their behavior and governing principles. This study characterized the passive discharge losses of a small scale FESS at low velocity and varying pressures. While there is potential for improvement, the methods described in this study make a valuable contribution to FESS technology by quantifying each source of passive discharge and validating models against experimental data. Future studies can employ and expand on the methods and findings of this study to advance FESS technology development and implementation.

References

[1] NRCAN, "Canada - a global leader in renewable energy: Enhancing collaboration on renewable energy technologies," in *Energy and Mines Ministers' Conference*, YellowKnife, Northwest Territories, 2013.

[2] B. Dunn, H. Kamath and J.-M. Tarascon, "Electrical storage for the grid: a battery of choices," *Science,* vol. 334, no. 6058, pp. 928-935, 2011.

[3] X. Luo, J. Wang, M. Dooner and J. Clark, "Overview of current development in electrical energy storage technologies and application potential in power system operation," *Applied Energy,* vol. 137, pp. 511-536, 2015.

[4] I. Hadjipaschalis, A. Poullikkas and V. Efthimiou, "Overview of current and future energy storage Technologies for electric power applications," *Renewable and Sustainable Energy Reviews,* vol. 13, no. 6-7, pp. 1513-1522, 2009.

[5] Temporal Energy Storage, "Convergent Energy + Power and Temporal Power Announce Flywheel Storage Project of Ontario Grid Operator," [Online]. Available: http://temporalpower.com/news/convergent-energy-power-and-temporal-power-announce-flywheel-storage-project-for-ontario-grid-operator/. [Accessed 12 April 2016].

[6] Beacon Power Corporation, "Beacon Power inagurates 20MW flywheel plant in NY," PennErgy, 21 July 2011. [Online]. Available: http://www.pennenergy.com/articles/pennenergy/2011/07/beacon-power-inaugurates.html. [Accessed 06 June 2017].

[7] G. Besel and E. Hau, "Flyhweel energy acumulators for city buses- steel and composite design," in *Flywheel Technology Symposium*, Scotsdale, AZ, 1980.

[8] S. Abuelsamid, "How It works: Porche 911's GT3R hybrid flywheel," Popular Mechanics, 8 October 2010. [Online]. Available: http://www.popularmechanics.com/cars/hybrid-electric/a6266/porsche-911-gt3r-hybrid-flywheel/. [Accessed November 2016].

[9] L. J. Lawson, "Flywheel trolley coach propulsion with high-capacity composite flywheel," in *Flywheel Technology Symposium*, Socttsdale, AZ, 1980.

[10] T. Zemo and D. Christofferson, "Flywheel-powered shuttle car for mine haulage," in *Flywheel Technology Symposium*, Scottsdale, AZ, 1980.

[11] G. Ertz, *Development, manufacturing and testing of a multi-rim (hybrid) flywheel rotor,* Edmonton, AB: Univ of Alberta, 2014.

[12] T. Mulcahy, J. Hull, K. Uherka, R. Abbound and J. Juna, "Test results of 2-kWh flywheel using passive PM and HTS bearings," *IEEE Transactions and Applied Superconductivity,* vol. 11, no. 1, pp. 1729-1739, 2001.

[13] A. Buchroithner, A. Haan, R. Pressmair, M. Bader, B. Schweighofer, H. Wegleiter and H. Edtmayer, "Decentralized low cost flyhweel energy storage for photovoltaic systems," in *International Conference on Sustainable Energy Engeinrring Application*, Tangerang, Indonesia, 2016.

[14] C. W. Gabrys and C. E. Bakis, "Design and testing of composite flywheel rotos," *Composite Materials: Testing and Design,* vol. 13, pp. 3-22, 1997.

[15] S. Ha, D.-J. Kim and T.-H. Sung, "Optimum design of multi-ring composite flywheel rotor using a modified generalized plane strain assumption," *International Journal of Mechanical Sciences,* vol. 43, pp. 993-1007, 2001.

[16] M. Krack, M. Secanell and P. Mertiny, "Advanced optimization strategies for cost-sensitive design of energy storage flywheel rotors," in *SAMPE*, Long Beach, California, 2011.

[17] A. Schulz, S. Sima, T. Hinterdorfer and W. J., "Innovative schwungradspeicher mit hoher energieeffizienz und zuverlassigkeit," *Elektrotechnik un Informationstechnk,* vol. 132, no. 8, pp. 481-490, Dec 2015.

[18] D. Sato, J. Itoh, T. Watanabe, K. Kawagoe, N. Yamada and K. Kato, "Development of magnetic coupling with variable thrust structure for flywheel energy storage system in long

lifetime UPS," in *Telecommunications Energy Conference*, Osaka, 2015.

[19] A. V. Filatov and E. H. Maslen, "Passive magnetic beraing for flywheel energy storage systems," *IEEE Transactions on Magnetics,* vol. 37, no. 6, pp. 3913-3924, 2001.

[20] ASM International, "Mechanically Assisted Degredation, Corrosion: Fundamentals, Testing and Protection," in *ASM Handbook*, Amer, 2003, pp. 322-330.

[21] D. Hills, "Mechanics of fretting fatigue," *Wear,* vol. 175, pp. 107-113, 1994.

[22] R. O. Woods, "Overview of component developement," in *Mechanical and Magnetic Energy Storage Contractors*, Luray, VA, 1978.

[23] W. H. Bauer, H. S. Gordon, G. V. Hassman and S. F. Y. F. C. Post, "Conceptual design of a flywheel energy storage system - final report," National Technical Information Services, U.S. Department of Commerce, Springfield, VA, 1979.

[24] Z. Long and Q. Zhiping, "Review of flywheel energy storage system," in *IEEE World Congress 2007*, Heidelberg, 2008.

[25] T. T. Chiao, "Fiber composite materials development for flywheel applications," in *Flywheel Technology Symposium*, Scottsdale, AZ, 1980.

[26] R. F. Foral and N. L. Newhouse, "On the performance of hoop would composite flywheel rotors," in *Flywheel Technology Symposium*, Scottsdale, AZ, 1980.

[27] D. E. Johnson and J. J. Gorman, "Maxium energy densities for composite flywheels," in *Flywheel Technology Symposium*, ScottsDale, AZ, 1980.

[28] M. Haridy, "Optimal materials selection for 2-rim and 3-rim rotors design fro FESS," *University of Alberta, Edmonton, Canata,* 2013.

[29] S. k. Ha, H. H. Han and H. Y. Han, "Design and manufacture of a compsite flywheel press-fit multi-rim rotor," *Journal of Reinforced PlasticS and Composites,* vol. 27, no. 9/2008, pp. 953-965, 2008.

[30] S. K. Ha, M. H. Kim, C. C. Han and S. Tae-Hyun, "Design and spin test of a hybrid composite flywheel rotor with split type hub," *Journal of Composite Materials,* vol. 40, no. 23/2006, pp. 2113-2130, 2006.

[31] T. A. Lembke, *Design and analysis of a novel low loss homopolar electrodynamic bearing,* Stockholm: KTH Electrical Engineering, 2005.

[32] G. Schweitzer and E. H. Maslen, Magnetic Bearings: Theory, Design and Application in Rotating Machinery, Heidelberg: Springer, 2009.

[33] H. Habermann and G. Liard, "An active magnetic beraings system," *Tribology International,* vol. 13, no. 2, pp. 85-89, 1980.

[34] G. Genta, Kinetic Energy Storage, Cambridge: Butterworth Co., 1985.

[35] T. A. Coombs, A. M. Campbell and D. A. Cardwell, "Development of an active superconducting magnetic bearing," *IEEE Transactions on Applied Superconductivity,* vol. 5, no. 2, pp. 630-633, 1995.

[36] Z. Xia, Q. Y. Chen, K. B. Ma, C. K. McMichael, M. Lamb, R. S. Cooley, P. C. Fowler and W. K. Chu, "Design of superconducting magnetic bearings with high levitating force for flywheel energy storage systems," *IEEE Transactions on Applied Superconductivity,* vol. 5, no. 2, pp. 622-625, 1995.

[37] T. A. Coombs, A. M. Campbell and R. W. R. Storey, "Superconducting magnetic bearings for energy storage flywheels," *IEEE Transactions on Applied Superconductivity,* vol. 9, no. 2, pp. 968-971, 1999.

[38] T. A. Coombs, "Bearings and energy storage," in *IEEE Colloquium on High Tc Superconducting Materials and Magnets*, Cambridge, 1995.

[39] S. Jung, J. Lee, B. Park, S. Jeong, J. Lee, B. Park, H. Kim and T. Sung, "Double-Evaporator Thermosiphon for Cooling 100 kWh Class Superconductor Flywheel Energy Storage System Bearings," *IEEE Transactions on Applied Superconductivity,* vol. 19, no. 3, pp.

2103-2106, 2009.

[40] S. Jiang, H. Wang and S. Wen, "Flywheel energy storage system with permanent magnet bearing and a pari of hybrid ceramic ball bearings," *Journal of Mechanical Science and Techology,* vol. 28, pp. 5043-5053, 2014.

[41] B. Bolund, H. Bernhoff and M. Leijon, "Flywheel energy and power storage systems," *Renewable and Sustainable Energy Reviews,* vol. 11, pp. 235-258, 2007.

[42] T. W. Place, "Composite material for UMTA flywheel trolley coach," in *Flywheel Technology Symposium*, Scottsdale, AZ, 1980.

[43] C. S. Heam, M. M. Flynn, M. C. Lewis, R. C. Thompson, B. T. Murphy and R. G. Longoria, "Low cost flywheel energy storage for a fuel cell powered transit bus," in *Vehicle Power and Propulsion Conference*, Arlington, TX, 2007.

[44] A. Rupp, H. Baier, P. Mertiny and M. Secanell, "Analysis of a flywheel energy storage system for light rail transit," *Energy,* vol. 107, pp. 625-638, 2016.

[45] J. Widmer and P. v. Burg, "Failure of tangentially wound composite energy storage flywheels (safety aspect of rotor bursts)," in *ENERCOMP*, Montreal, 1995.

[46] Brother, "TC-20B," Brother, 2017. [Online]. Available: http://www.brother.com/europe/machine/tc20b/index.htm. [Accessed 2016].

[47] Hardinge Group, "GX 250 5F (4+1) (12"x16"x17")," Hardinge Gropu, [Online]. Available: http://hardinge.com/ProductCatalog/Product/ProductId/193. [Accessed 2016].

[48] "Coefficients of Friction for Steel," Hypertextbook, 2005. [Online]. Available: https://hypertextbook.com/facts/2005/steel.shtml. [Accessed 2016].

[49] AZO Materials, "AISI 1018 Mild/Low Carbon Steel," AZO Materials, 5 07 2012. [Online]. Available: https://www.azom.com/article.aspx?ArticleID=6115. [Accessed 2016].

[50] Advanced Materials Engineering Solutions, "Metric Bolt Grades and Strength Calculator," Advanced Mechanical Engineering Solutions, 2013. [Online]. Available:

http://www.amesweb.info/Screws/Metric_Bolt_Grades_Strength.aspx. [Accessed 2016].

[51] International Standard Organization, "ISO 898-1," ISO, 2009.

[52] Kontronik, "Pyro 850," Kontronik, [Online]. Available: http://www.kontronik.com/en/products/motors/pyro/pyro-850/pyro-850-50.html. [Accessed March 2016].

[53] John, "Thermocouple Vacuum Gauge," Instrumentation Today, 5 October 2011. [Online]. Available: http://www.instrumentationtoday.com/thermocouple-vacuum-gauge/2011/10/. [Accessed 22 Febuary 2017].

[54] Granville-Philips, *Series 270 Ionization Gauge Controller Instruction Manual,* Boulder CO: Granville-Philips, 1996.

[55] Y. Xing, H. Xu, S. Pei, X. Chen and L. Xuejing, "A novel non-Hertzian contact model of spherical roller bearings," *Journal of Engineering Tribology,* vol. 230, no. 1, pp. 3-13, 2015.

[56] T. A. Harris and M. N. Kotzalas, Advanced Concepts of Bearing Technology, Rolling Bearing Analysis, Fifth Edition, CRC Press, 2006.

[57] C. Shen, Rarefied Gas Dynamics, Heidelberg: Spring-Verlag, 2005.

[58] V. E. Broecker, "Theorie und experiment zum reibungswiderstand der glatten rotierenden scheibe bei tubolenter stromung," *ZAMM,* vol. 1/2, pp. 68-76, 1959.

[59] W. Tong, Mechanical Design of Electric Motors, CRC Press, 2014.

[60] Mathworks, "Least-Squares Fitting," Mathworks, 2017. [Online]. Available: http://www.mathworks.com/help/curvefit/least-squares-fitting.html. [Accessed June 2017].

[61] H. Uhlig, I. Ming Feng and W. Tierney, "A fundamental investigation of fretting corrosion," National Advisory Committee for Aeronautics, 1953.

[62] A. Neyman and O. Olszewski, "Research on fretting wear dependence of hardness ratio and friction coefficient of fretted couple," *Wear,* Vols. 162-164, pp. 939-943, 1993.

[63] Aerospace Specification Metals Inc, "Aluminum 6061-T6; 6061-T651," ASM, [Online]. Available: http://asm.matweb.com/search/SpecificMaterial.asp?bassnum=ma6061t6. [Accessed 2017].

[64] A. Mukhopadhyay, S. Data and D. Chakraborty, "On the microhardness of silicon nitride and sialon ceramics," *Journal of European Ceramics Society,* vol. 6, pp. 303-311, 1990.

[65] A. Merstallinger, M. Sales and E. Semerad, "Assessment of cold welding between separable contact surfaces due to impact and fretting under vacuum," ESA Communication Production Office, Noordwijk, Netherlands, 2009.

[66] Mathworks, "Evaluating Goodness of FIt," Mathworks, 2017. [Online]. Available: https://www.mathworks.com/help/curvefit/evaluating-goodness-of-fit.html. [Accessed June 2017].

[67] H. Bangcheng, Z. Shiqiang and W. Xi, "Integral design and analysis of passive magnetic beraing and active radial magnetic bearingfor agile satellite application," *IEEE Transaction on Magnetics,* vol. 48, no. 6, pp. 1959-1966, 2012.